THE UNIVERSITY OF CHICAGO

ANGULAR-MOMENTUM-DOMINATED ELECTRON BEAMS AND
FLAT-BEAM GENERATION

A DISSERTATION SUBMITTED TO
THE FACULTY OF THE DIVISION OF THE PHYSICAL SCIENCES
IN CANDIDACY FOR THE DEGREE OF
DOCTOR OF PHILOSOPHY

DEPARTMENT OF PHYSICS

BY
YIN-E SUN

CHICAGO, ILLINOIS
JUNE 2005

To my husband,
Philippe R.-G. Piot

ABSTRACT

In the absence of external forces, if the dynamics within an electron beam is dominated by its angular momentum rather than other effects such as random thermal motion or self Coulomb-repulsive force (i.e., space-charge force), the beam is said to be angular-momentum-dominated. Such a beam can be directly applied to the field of electron-cooling of heavy ions; or it can be manipulated into an electron beam with large transverse emittance ratio, i.e., a flat beam. A flat beam is of interest for high-energy electron-positron colliders or accelerator-based light sources.

An angular-momentum-dominated beam is generated at the Fermilab/NICADD photoinjector Laboratory (FNPL) and is accelerated to an energy of 16 MeV. The properties of such a beam is investigated systematically in experiment. The experimental results are in very good agreement with analytical expectations and simulation results. This lays a good foundation for the transformation of an angular-momentum-dominated beam into a flat beam.

The round-to-flat beam transformer is composed of three skew quadrupoles. Based on a good knowledge of the angular-momentum-dominated beam, the quadrupoles are set to the proper strengths in order to apply a total torque which removes the angular momentum, resulting in a flat beam. For bunch charge around 0.5 nC, an emittance ratio of 100 ± 5 was measured, with the smaller normalized root-mean-square emittance around 0.4 mm-mrad.

Effects limiting the flat-beam emittance ratio are investigated, such as the chromatic effects in the round-to-flat beam transformer, asymmetry in the initial angular-momentum-dominated beam, and space-charge effects. The most important limiting factor turns out to be the uncorrelated emittance growth caused by space charge when the beam energy is low, for example, in the rf gun area. As a result of such emittance growth prior to the round-to-flat beam transformer, the emittance ratio achievable in simulation decreases from orders of thousands to hundreds.

Finally, factors that might spoil the smaller transverse emittance such as beamline misalignments and dispersions caused by magnetic elements are discussed. The limit of the emittance measurement system, such as camera resolution, is also studied.

ACKNOWLEDGEMENTS

breaking the rf calibration kit despite his warnings.

As part of TESLA collaboration, FNPL received lots of support from other collaborating institutes. In particular, I wish to thank Rudolf Neumann and Manfred Wendt from DESY for their help in commissioning the beam position monitor system.

For the flat-beam experiment, I benefit from valuable discussions with Dr. Klaus Flöttmann from DESY Hamburg, Dr. Steve Lidia from Berkeley, Dr. Daniel Mihalcea from Norther Illinois University and ShaoHeng Wang from Indiana University. Prof. Massimo Ferrario from INFN Frascati taught me how to use his simulation code HOMDYN and explained emittance compensation to me.

During the early years of my graduate student life, I worked on an experiment related to the scanning electron microscope at the Enrico Fermi Institute. Big thanks to Bud Kapp there for the fun and the ice cream. I also wish to thank Prof. Albert Crewe, Prof. Yau Wah and Prof. Mark Oreglia for their discussions and support. I benefit so much from the classes taught by Prof. Jonathan Rosner, and he is a model to follow in many aspects. I also wish to thank him for carefully reading this dissertation and for his comments.

To Vicki Stone, Aspasia Sotir-Plutis and Nobuko McNeill at the University of Chicago, Jackie Sullivan at Fermilab, Renee Lanham at Argonne, thank you for taking care of the things related to life, if not physics, during the past years.

A special thanks is due to Prof. Court Bohn from Norther Illinois University for having believed in me all the way. He has always been there whenever I needed help. He took the pain to go through this manuscript at different stages and made valuable comments on physics as well as corrections to my English.

My world would have been totally different had I not met Philippe Piot. I thank him for taking numerous shifts with me. His knowledge of beam physics served to answer so many questions of mine, and his exceptional computing skills opened my eyes to the wonders of the numerical simulation world. Yet above all, life beyond work has been wonderful and perfect because I am lucky to have him.

Finally, I want to express my gratitude to my sisters and parents. While I have given up trying to explain to them what it is exactly that I study, they have always been there for me nonetheless. I cannot thank you enough.

TABLE OF CONTENTS

LIST OF FIGURES

LIST OF TABLES

CHAPTER 1
SOME BASICS OF ACCELERATORS AND BEAMS

A particle accelerator is a machine that accelerates electrons, positrons, protons or any other charged particles. A collection of particles with a preferred direction of motion is a *beam*. The beam energy could be raised using electric fields, mostly radio-frequency (rf) fields in modern accelerators. The start of an accelerator is the particle source, sometimes also called a *gun*. An accelerating section follows the gun to boost the energy to the desired level.

In this Chapter, we will first get familiar with the basic mathematical formalism used in accelerator physics. We will also discuss several important concepts in beam physics that are used extensively in this dissertation.

1.1   The coordinates

The common coordinate system used in linear accelerator physics is the Cartesian system (x, y, z). The z coordinate coincides with the beam pipe, i.e., the particle propagation direction, and is called the longitudinal coordinate. In contrast, x and y are the transverse coordinates, with x being horizontal and y being vertical; (x, y, z) forms a right-hand system.

The time derivatives of (x, y, z), usually noted by $(\dot{x}, \dot{y}, \dot{z})$ or (v_x, v_y, v_z), are the velocities of the particles. Particle momentum p_i is given by $\gamma m v_i$ ($i = x, y$ or z), where m is the rest mass of the particle, γ is the Lorentz factor given by $\gamma = 1/\sqrt{1 - \beta^2}, \beta = v/c, v = \sqrt{\sum v_i^2}$ and c is the speed of light in vacuum. The longitudinal velocity v_z is normally much larger than the two transverse velocities v_x and v_y. As a result, $v_z \approx v, v_z/c \approx \beta$. This is not true in the immediate region of the particle source where particles have not yet gained significant acceleration in the longitudinal direction.

As we will see, more extensively used are the derivatives of (x, y) with respect to z, noted by x', y'. It can be shown that $x' = v_x/v_z = p_x/p_z$, etc.

1.2   Phase space, emittance, and brightness

The coordinates (x, p_x, y, p_y, z, p_z) form a six-dimensional (6-D) *phase space.* Each particle can be represented by a point in such a space. All particles in a beam will occupy a volume.

A figure of merit of the beam quality in the (x, p_x) subspace is the normalized root-mean-square (rms) beam emittance. For the following discussion, let's assume that $\langle x \rangle = \langle p_x \rangle = 0$, where "$\langle \ \rangle$" stands for taking the average value of all the N particles, e.g., $\langle x \rangle = \left(\sum_{i=1}^{N} x_i \right)/N$, etc.. The normalized rms beam emittance is defined as [1, 2]:

$$\varepsilon_{nx} = \frac{1}{mc}\sqrt{\langle x^2 \rangle \langle p_x^2 \rangle - \langle x p_x \rangle^2}, \tag{1.1}$$

The value $\sigma_x = \sqrt{\langle x^2 \rangle}$ is the rms beam size along the x-axis. In similar fashion, one can define normalized rms emittance in (y, p_y) and (z, p_x) subspace as ε_{ny} and ε_{nz}.

ε_{nx} is a measure of the phase space volume projected into the (x, p_x) subspace. The product $\varepsilon_{nx}\varepsilon_{ny}\varepsilon_{nz}$ is the volume of the 6-D phase space. *Liouville's theorem* states for noninteracting particles, the particle density, or the volume occupied by a certain number of particles in the 6-D phase space, remains invariant [3]. As a result, if there are no forces that couple x motion to the other directions, ε_{nx} is a constant of motion.

Another common notation is the *trace space* with coordinates (x, x', y, y'). If x' is used instead of p_x in the above discussion, then the trace-space emittance, also known as the unnormalized emittance, is defined as

$$\varepsilon_x = \sqrt{\langle x^2 \rangle \langle x'^2 \rangle - \langle x x' \rangle^2} \tag{1.2}$$

The relation between the unnormalized emittance [Eq. (1.2)] and the normalized emittance [Eq. (1.1)] is discussed in detail in Ref. [4]. For higher energy with low energy spread, we have

$$\varepsilon_x = \varepsilon_{nx}\frac{mc}{p_z} \approx \frac{\varepsilon_{nx}}{\beta\gamma}. \tag{1.3}$$

Another figure of merit of a particle beam quality is its *brightness*. If only the

transverse properties of the beam are considered, the differential brightness is defined as [5]

$$dB = \frac{d^2 I}{dS \, d\Omega},$$

(1.4)

where I is the beam current, S is the beam area in (x, y) space, and Ω is the beam solid angle in (x', y') space. Hence the differential brightness is the beam density per solid angle. Sometimes it is more useful to define the average brightness given by

$$B = \frac{I}{V_4}$$

(1.5)

where $V_4 = \int \int dS d\Omega$ is the 4-D trace-space volume. Meanwhile, V_4 is related to the product of the two transverse rms beam emittances as defined in Eq. (1.2). The brightness can thus be related to the rms emittances via

$$B = \mathcal{C} \frac{I}{\varepsilon_x \varepsilon_y},$$

(1.6)

where $\mathcal{C}$ is a constant determined by the beam distribution. As an example, for a Gaussian beam, the peak brightness is given by:

$$B_{pk}^G = \frac{1}{4\pi^2} \frac{I}{\varepsilon_x \varepsilon_y}.$$

(1.7)

Another example of theoretical importance is the Kapchinsky-Vladimirsky (K-V) distribution [6], in which the beam is confined to a 4-D ellipsoidal shell. The brightness of a K-V-distributed beam is related to its emittances via

$$B = \frac{2}{\pi^2} \frac{I}{\varepsilon_x \varepsilon_y}.$$

(1.8)

In view of Eq. (1.3), the *normalized brightness* is given by $B_n = B/(\beta\gamma)^2$.

1.3   Transfer matrix and beam matrix

Consider the transverse equation of motion of a particle in an accelerator:

$$u'' + K(z)u = 0, \tag{1.9}$$

where u can be either x or y, and $K(z)$ is a function that describes the external field in the beamline and usually is piecewise constant. Eq. (1.9) is also known as *Hill's equation*. Notice that there is no first derivative terms in Eq. (1.9), which indicates that there is no dissipative force.

Suppose $A(z)$ and $B(z)$ are two independent solutions of Eq. (1.9) that satisfy the following boundary conditions:

$$A(z_0) = B'(z_0) = 1,$$
$$A'(z_0) = B(z_0) = 0.$$

Any solution of Eq. (1.9) can be written as

$$u(z) = A(z)u(z_0) + B(z)u'(z_0),$$
$$u'(z) = A'(z)u(z_0) + B'(z)u'(z_0);$$

or in matrix formalism, as

$$U(z) = M(z|z_0)U(z_0), \quad \text{with} \ \ U(z) = \begin{bmatrix} u(z) \\ u'(z) \end{bmatrix}, \tag{1.10}$$

and

$$M(z|z_0) = \begin{bmatrix} A(z) & B(z) \\ A'(z) & B'(z) \end{bmatrix}. \tag{1.11}$$

$M(z|z_0)$ is called the *transfer matrix* from z_0 to z. Since there is no first-order derivative term in Eq. (1.9), the determinant of M, which is the Wronskian, is unity.

By using the matrix formalism, the general properties of Eq. (1.9) are separated from each particular solution since M depends only on the beamline elements between

two points z_0 and z [7]. The transfer matrix from z_0 to $z_1, z_2, \cdots, z_{n-1}, z_n$ is the product of the matrices of the sub-intervals:

$$M(z_n|z_0) = M(z_n|z_{n-1}) \cdots M(z_2|z_1)M(z_1|z_0). \tag{1.12}$$

Consider an example where K is a constant k for $z_0 < z < z_1$. Eq. (1.9) becomes

$$u''(z) + ku(z) = 0. \tag{1.13}$$

For positive k, the transfer matrix is

$$M(z_1|z_0) = \begin{bmatrix} \cos\varphi & \frac{\sin\varphi}{\sqrt{k}} \\ -\sqrt{k}\sin\varphi & \cos\varphi \end{bmatrix}, \quad \text{with} \quad \varphi = (z_1 - z_0)\sqrt{k}. \tag{1.14}$$

For negative k, we have

$$M(z_1|z_0) = \begin{bmatrix} \cosh\varphi & \frac{\sinh\varphi}{\sqrt{|k|}} \\ \sqrt{|k|}\sinh\varphi & \cosh\varphi \end{bmatrix}, \quad \text{with} \quad \varphi = (z_1 - z_0)\sqrt{|k|}. \tag{1.15}$$

For example, for a force-free drift space, we have $k = 0$ and

$$M(z|z_0) = \begin{bmatrix} 1 & z - z_0 \\ 0 & 1 \end{bmatrix}. \tag{1.16}$$

For a quadrupole of length $l = z - z_0$ and strength k, the transfer matrix is given by either Eq. (1.14) or Eq. (1.15) depending on whether k is positive (focusing) or negative (defocusing), respectively. In the case where the focal length f of the quadrupole is large compared to its length l, the *thin lens approximation* applies. Introducing $1/f = kl$, we have

$$M = \begin{bmatrix} 1 & 0 \\ -1/f & 1 \end{bmatrix}. \tag{1.17}$$

So far we only considered 2×2 transfer matrices. A 4×4 transfer matrix can

be introduced for propagating beam in the four trace-space coordinates (x, x', y, y'). This is useful when the motions in x and y degrees of freedom are coupled.

The equations of motion for a Hamiltonian system can be written as:

$$q_i = \frac{\partial H}{\partial p_i}, \quad p_i = -\frac{\partial H}{\partial q_i}, \tag{1.18}$$

where H is the Hamiltonian of the system and $q_i = (x, y, z)$ are the coordinates and p_i are the conjugate momenta of q_i. Given initial values q_{i0}, p_{i0}, a solution of the following form at time t exists:

$$q_i = q_i(q_{i0}, p_{i0}, t), \quad p_i = p_i(q_{i0}, p_{i0}, t). \tag{1.19}$$

This may be viewed as a canonical transformation from (q_{i0}, p_{i0}) to (q_i, p_i).

The generalization of the 6×6 transfer matrix for a non-linear transformation is:

$$\mathcal{M}_6 = \begin{bmatrix} \frac{\partial q_1}{\partial q_{10}} & \cdots & \frac{\partial q_1}{\partial p_{30}} \\ \vdots & \vdots & \vdots \\ \frac{\partial p_3}{\partial q_{10}} & \cdots & \frac{\partial p_3}{\partial p_{30}} \end{bmatrix}. \tag{1.20}$$

It can be shown that [7, 8, 9]

$$\widetilde{\mathcal{M}_6} J_6 \mathcal{M}_6 = J_6, \tag{1.21}$$

where $\widetilde{\mathcal{M}_6}$ is the transpose of $\mathcal{M}_6$, and J_6 is given by

$$J_6 = \begin{bmatrix} J & 0 & 0 \\ 0 & J & 0 \\ 0 & 0 & J \end{bmatrix}, \tag{1.22}$$

with J being the 2×2 unit symplectic matrix

$$J = \begin{bmatrix} 0 & 1 \\ -1 & 0 \end{bmatrix}. \tag{1.23}$$

A matrix that satisfies Eq. (1.21), such as $\mathcal{M}_6$, is called *symplectic*. In similar

fashion, one can define a 4×4 symplectic matrix $\mathcal{M}_4$ and a 2×2 symplectic matrix $\mathcal{M}_2$. For a 2×2 matrix, the symplectic condition is equivalent to the requirement that the determinant of the matrix should be unity.

In 4-D phase space, (x, p_x, y, p_y) compose a set of canonical variables. If $x' = p_x/p_z \approx p_x/p$, $y' = p_y/p_z \approx p_x/p$, where $p = \sqrt{p_x^2 + p_y^2 + p_z^2}$, then for a conservative system, the transfer matrix can be written as:

$$M_4 = \mathbf{P}^{-1}\mathcal{M}_4\mathbf{P}, \quad \text{with} \quad \mathbf{P} = \begin{bmatrix} 1 & 0 & 0 & 0 \\ 0 & p & 0 & 0 \\ 0 & 0 & 1 & 0 \\ 0 & 0 & 0 & p \end{bmatrix}. \tag{1.24}$$

From Eq. (1.21) and Eq. (1.24), we have

$$\widetilde{M_4}J_4M_4 = J_4, \quad \text{where} \quad J_4 = \begin{bmatrix} J & 0 \\ 0 & J \end{bmatrix}. \tag{1.25}$$

Therefore the transfer matrix is symplectic. We will use the properties of a symplectic 4×4 matrix extensively in Section 3.2.

In the case of a linear transformation from z_i to z_f, we have

$$U(z_f) = M_4 U(z_i), \tag{1.26}$$

where U is the trace space coordinates of a particle given by

$$U = \begin{bmatrix} x \\ x' \\ y \\ y' \end{bmatrix}, \quad \text{and} \quad M = \begin{bmatrix} M_{11} & M_{12} & M_{13} & M_{14} \\ M_{21} & M_{22} & M_{23} & M_{24} \\ M_{31} & M_{32} & M_{33} & M_{34} \\ M_{41} & M_{42} & M_{43} & M_{44} \end{bmatrix}, \tag{1.27}$$

where $M_{ij} = \partial U_i(z_f)/\partial U_j(z_i)$ are the constants determined by the linear transformation. For example, the transfer matrix of a quadrupole in the thin lens approximation

is

$$M = \begin{bmatrix} 1 & 0 & 0 & 0 \\ -\frac{1}{f} & 1 & 0 & 0 \\ 0 & 0 & 1 & 0 \\ 0 & 0 & \frac{1}{f} & 1 \end{bmatrix}. \tag{1.28}$$

Now consider a packet of particles, called a *bunch*, the distribution of which is centered at the origin of the 4-D trace space, i.e.,

$$\sum x_i = 0, \quad \sum p_{xi} = 0, \text{ etc.}$$

The covariance matrix of U, called the *beam matrix*, is defined by

$$\Sigma = \langle U\widetilde{U} \rangle = \begin{bmatrix} \langle x^2 \rangle & \langle xx' \rangle & \langle xy \rangle & \langle xy' \rangle \\ \langle x'x \rangle & \langle x'^2 \rangle & \langle x'y \rangle & \langle x'y' \rangle \\ \langle yx \rangle & \langle yx' \rangle & \langle y^2 \rangle & \langle yy' \rangle \\ \langle y'x \rangle & \langle y'x' \rangle & \langle y'y \rangle & \langle y'^2 \rangle \end{bmatrix}. \tag{1.29}$$

We see that transverse rms emittances [see Eq. (1.2)] are given by the square-root of the determinants of the 2×2 diagonal blocks. For example,

$$\varepsilon_x = \left| \begin{matrix} \langle x^2 \rangle & \langle xx' \rangle \\ \langle x'x \rangle & \langle x'^2 \rangle \end{matrix} \right|^{0.5}. \tag{1.30}$$

where "| |" is the determinant operator.

As a result of Eq. (1.26), the beam matrix propagates via

$$\Sigma(z_f) = M\Sigma(z_i)\widetilde{M}. \tag{1.31}$$

If $|M| = 1$, we see that $\varepsilon_{4D} = \varepsilon_x \varepsilon_y$ is a constant of motion. If acceleration or deceleration takes place, then $|M| \neq 1$ and the normalized 4-D rms emittance remains a constant of motion.

1.4 Photocathode rf gun

1.4.1 Introduction

Free electrons can be obtained in many ways, such as by thermal emission from a *thermionic* cathode, or photoemission via the photoelectric effect when laser light shines on a *photocathode.* If the electron source of an accelerator incorporates a photocathode, it is called a *photocathode gun.* Systems in which the photocathode is directly inserted into an rf accelerating field is called an *photocathode rf gun.* The start of a *photoinjector* is a photocathode gun, followed by a section of linear beamline which incorporates accelerating structures, magnetic elements, and beam diagnostics, etc.

The photocathode rf gun has several advantages that make it the choice of technology for high-brightness electron beams. First, the initial electron distribution, both transversely and longitudinally, can be controlled via the photocathode drive-laser. By tuning the drive laser parameters, the transverse beam emittance can be optimized. Second, since ultra-short pulsed laser light is available, the electron bunch length can be much smaller than the rf wavelength of the gun, hence eliminating the need for complicated bunching schemes. Finally the charge density achieved with a photocathode is of the order kA·cm^{-2}, about two orders of magnitude higher than a thermionic cathode [10].

Since the first photoinjector experiment at LANL in 1986 [11], the applications of electron beams produced in photoinjectors range from free electron lasers (FELs) to synchrotron light sources, high-energy electron-positron colliders, electron cooling of other heavier ions (see Section 2.3.1) etc. The best normalized transverse emittance achieved out of the gun for a bunch charge of 1 nC is $\sim$ 1 mm-mrad [12].

The main components of a photocathode rf gun include: photocathode, drive laser, rf accelerating cavity with various number of rf cells, and solenoids surrounding the cavity for beam focusing and phase-space manipulation. A sketch of a photocathode rf gun with a 1.5-cell normal-conducting cavity is shown in Figure 1.1.

While the beam dynamics of a photoinjector is complicated and in many cases needs to be studied numerically, there are some well-developed analytical theories,
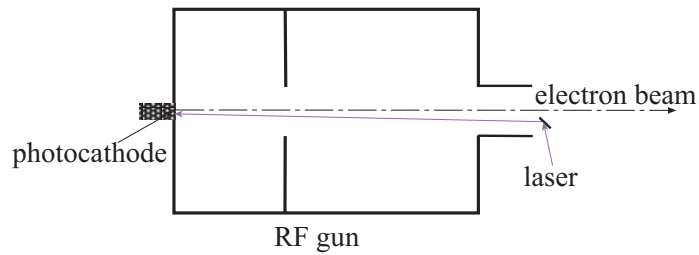
Figure 1.1: Schematic of a 1.5-cell rf gun.

such as emittance compensation by Carlsten in 1988 [13], rf and space-charge effects on the beam emittance by Kim in 1989 [14], particle motion in an rf photoinjector by Serafini in 1995 [15], and envelope analysis of emittance compensation by Serafini and Rosenzweig in 1997 [16]. These analytical models provide some preliminary guidance a priori to numerical modeling.

1.4.2   Emittance growth from rf and space charge

Kim [14] calculated the emittance growth caused by the rf field curvature and space charge analytically for a $(n + 1/2)$-cell rf gun. Starting with the electric field on axis taken to be

$$E_z = E(z) \cos kz \sin(\omega t + \phi_0) \tag{1.32}$$

where $k = 2\pi/\lambda$ and λ is the rf wavelength, $\omega = ck$ and ϕ_0 is the initial rf phase at $z = 0$, $t = 0$, and assuming that E_z is independent of the transverse coordinates, from Maxwell's equations one obtains

$$E_r = \frac{r}{2} \frac{\partial E_z}{\partial z}, \quad \text{and } cB_\theta = \frac{r}{2c} \frac{\partial E_z}{\partial t}. \tag{1.33}$$

The radial force is thus given by

$$F_r = e(E_r - \beta cB_\theta). \tag{1.34}$$

Kim showed that the radial force can be written as

$$
\begin{aligned}
F_r = er\Big\{ &- \frac{1}{2c}\frac{\mathrm{d}}{\mathrm{d}t}\big(E(z)\sin kz \cos(\omega t + \phi_0)\big) - \frac{1}{2}\big(\frac{\mathrm{d}}{\mathrm{d}z}E(z)\big)\cos kz \sin(\omega t + \phi_0) \\
&+ \frac{\beta}{2}\big(\frac{\mathrm{d}}{\mathrm{d}z}E(z)\big)\sin kz \cos(\omega t + \phi_0)\Big\}.
\end{aligned}
$$

(1.35)

The equation of radial motion is

$$
\frac{\mathrm{d}p_r}{\mathrm{d}t} = F_r,
$$

(1.36)

where p_r is the radial momentum. To calculate the emittance caused by the rf field, we need to integrate Eq. (1.36) to get p_r. The first term of Eq. (1.35) is a total time derivative of an expression which vanishes at the photocathode and outside the cavity exit, so its integral vanishes. The second and third terms are non-zero only at the region where $E(z)$ varies, such as at the cavity exit. Kim takes a step function for $E(z)$ at the cavity exit and finds the minimum normalized transverse emittance (in Cartesian coordinates) from rf effects to be:

$$
\varepsilon_{nx}^{rf} = \frac{\alpha k^3 \sigma_x^2 \sigma_z^2}{\sqrt{2}},
$$

(1.37)

where $\alpha = \frac{eE_0}{2mc^2k}$ is a dimensionless parameter characterizing the rf field strength, E_0 is the peak accelerating field, and σ_x and σ_z are the transverse and longitudinal rms beam sizes, respectively.

For the emittance growth caused by space charge, Kim notes that the space charge force scales as

$$
\mathbf{F} = \frac{1}{\gamma^2}\mathbf{f}(\gamma)
$$

(1.38)

and the function $\mathbf{f}(\gamma)$ behaves as follows:

$$
\mathbf{f}(\gamma) \sim \mathcal{O}(1), \quad \gamma \gg A;
$$

(1.39)

$$
f_x \sim \mathcal{O}(\gamma) \text{ and } f_z \sim \mathcal{O}(\gamma^2), \quad 1 \le \gamma \ll A;
$$

(1.40)

where $A = \sigma_x/\sigma_z$ is the aspect ratio.

Integrating Eq. (1.36) over time, Kim obtained the emittance growth caused by

space charge:

$$\varepsilon_{n,i}^{sc} = \frac{\pi}{4} \frac{1}{\alpha k \sin \phi_0} \frac{I}{I_0} \mu_i(A); \ i = x \text{ or } z. \tag{1.41}$$

Here I is the peak current, $I_0 = 4\pi\epsilon_0 mc^3/e = 17$ kA the Alfvén current, ϵ_0 the permittivity of free space, e the electron charge, and $\mu_i(A)$ are dimensionless functions that depend on the beam distribution. For a Gaussian distribution, Kim gave the following approximations:

$$\begin{aligned} \mu_x(A) &= \frac{1}{3A+5}, \\ \mu_z(A) &= \frac{1.1}{1+4.5A+2.9A^2}. \end{aligned} \tag{1.42}$$

Eqs. (1.37) and (1.41) give an estimations of the emittance growths, assuming the transverse position of the electrons to be constant. Therefore the emittance growths are results of changes in transverse momenta.

CHAPTER 2
ANGULAR-MOMENTUM-DOMINATED ELECTRON BEAMS AND THEIR APPLICATIONS

2.1 Angular-momentum-dominated electron beams

Several factors drive the bulk properties of an electron beam, such as space charge, beam emittance, angular momentum, and external electromagnetic focusing. Beam dynamics differs drastically when one factor dominates over the others; see Figure 2.1. In (a), the beam is emittance-dominated and the electron motion is random; in (b), the beam is angular-momentum-dominated and the electrons shear in a well defined vortex pattern; in (c), the beam is space-charge-dominated; the electrons move outwards along the radial direction due to the repulsive collective Coulomb force within the beam.
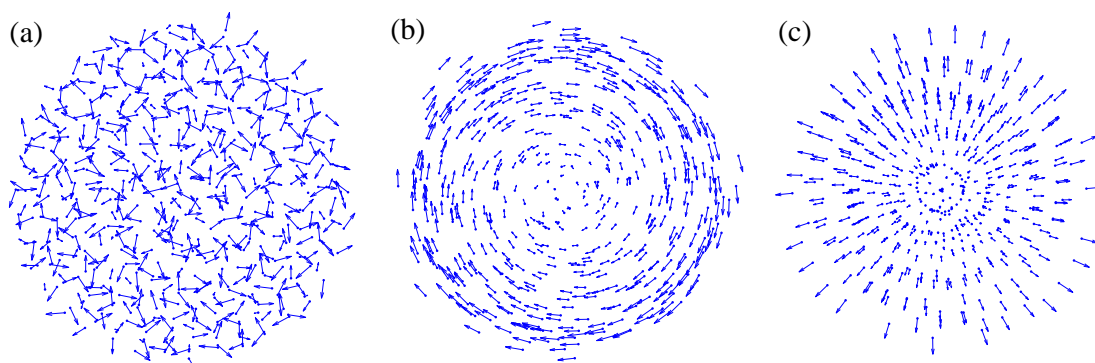
Figure 2.1: Motions of the electrons when the beam is dominated by (a) emittance, (b) angular momentum or (c) space charge. Each dot represents an electron in (x, y) space, and the arrow shows the magnitude and direction of the electron's velocity.

The evolution of the transverse rms beam size of an electron bunch in a drift, i.e., in the absence of external electromagnetic forces, is described by the following rms envelope equation [17]

$$\sigma'' - \frac{K}{4\sigma} - \frac{\varepsilon_u^2}{\sigma^3} - \frac{\mathcal{L}^2}{\sigma^3} = 0, \tag{2.1}$$

13

where σ is the transverse rms size, $K = \frac{2I}{I_0 \beta^3 \gamma^3}$ is the generalized perveance, I is the absolute value of the instantaneous beam current, and $I_0 = 4\pi\epsilon_0 mc^3/e \approx 17 \,\text{kA}$ is the Alfvén current, ε_u is the uncorrelated transverse rms emittance, and $\mathcal{L}$ is related to the average canonical angular momentum $\langle L \rangle$ (see Section 2.2) and the longitudinal momentum p_z of the beam via

$$\mathcal{L} = \frac{\langle L \rangle}{2p_z}. \tag{2.2}$$

The second, third, and fourth terms of Eq. (2.1) respectively represent the effects due to space charge, emittance, and angular momentum. When the fourth term is much greater than the second and the third term, the beam is said to be *angular-momentum-dominated*.

If there is external electromagnetic linear focusing, an extra term in the form of $k_0\sigma$ can be added to the envelope equation, where k_0 is related to the strength of the external focusing force.

2.2 Generation of angular-momentum-dominated electron beams in a photocathode rf gun

The magnetic field on the photocathode should be avoided if the beam emittance needs to be minimized. This can be seen from Eq. (2.1), where the canonical angular momentum term $\mathcal{L}$ has the same effect on the beam envelope as the emittance ε_u. However, the magnetic field is necessary to produce an angular-momentum-dominated beam, as we will see below.

In a rotationally invariant system, the conservation of canonical angular momentum L [18] states that

$$L = \gamma m r^2 \dot{\phi} + \frac{e}{2\pi}\Phi = const., \tag{2.3}$$

where (r, ϕ, z) are the cylindrical coordinates, and Φ is the magnetic flux enclosed inside a circle of radius r at a given location in z. Eq. (2.3) is also known as *Busch's theorem* [19]. At the photocathode, the average of the first term in Eq. (2.3) is zero since $\langle \dot{\phi} \rangle = 0$. The second term must not vanish in order to allow the beam to acquire an angular momentum. Therefore an axial magnetic field on the cathode is required

to generate an angular-momentum-dominated electron beam.

2.3 Applications of angular-momentum-dominated electron beams

2.3.1 Electron cooling of heavy ions

A direct application of the angular-momentum-dominated beam is the electron cooling of heavy-ion beams [20, 21, 22]. In such a scheme, a cold electron beam co-propagates with the ion beam at the same average velocity. Collisions of ions with electrons lead to a transfer of thermal motion from the ion to the electron beam. The cooling efficiency can be greatly improved by using a "magnetized", i.e., an angular-momentum-dominated electron beam.
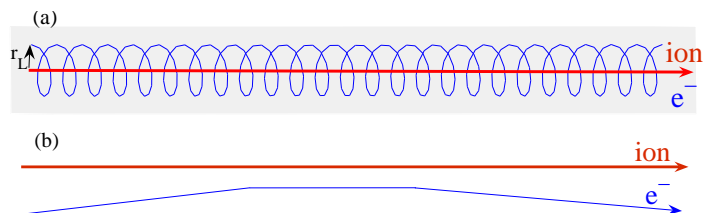
Figure 2.2: Cooling of heavy ion beams using (a) magnetized electron beam; (b) non-magnetized electron beam. The thicker (red) and thinner (blue) lines represent the trajectories of an ion and an electron in the simplified picture.

In a simplified picture (see Figure 2.2), consider an ion and a magnetized electron colliding with impact parameter ρ. Let the Larmor radius of the electron in the magnetic field B_z be r_L, given by

$$r_L = \frac{v_{e\perp}}{eB_z},\tag{2.4}$$

where $v_{e\perp}$ is the transverse velocity of the electron. For $\rho > r_L$, the effective cooling duration is determined by

$$\tau \approx \frac{\rho}{v - v_{e\parallel}},\tag{2.5}$$

where v and $v_{e\parallel}$ are the longitudinal velocities of the ion and electron, respectively;

while for non-magnetized electron beam, $\tau \approx \rho/v_{e\perp}$. Since $(v - v_{e\parallel})$ can be made much smaller than $v_{e\perp}$, the effective cooling duration can thus be increased by a factor of $v_{e\perp}/(v - v_{e\parallel})$.

To summarize, as the ion beam and electron beam co-propagate, the electron-ion effective interaction is increased by using an angular-momentum-dominated electron beam, and the cooling rate is mainly determined by the longitudinal momentum spread of the electron beam, which can be made much smaller than the transverse one. In Ref. [23], an angular-momentum-dominated beam is proposed to be accelerated to ~ 50 MeV and used for electron beam cooling of ion beams in the Relativistic Heavy Ion Collider (RHIC).

2.3.2   Flat-beam generation

A *flat* electron beam, i.e. a beam with high transverse emittance ratio, can be produced from an angular-momentum-dominated beam [24]. The technique consists of manipulating an angular-momentum-dominated beam produced by a photoinjector using the linear transformation described in Ref. [25]. A round-to-flat beam transformer consisting of three skew quadrupoles and drift spaces is discussed in Ref. [26]. The transformation removes the angular momentum and results in a flat beam. A proof-of-principle flat-beam experiment was conducted at the Fermilab/NICADD Photoinjector Laboratory (FNPL)[1] and an emittance ratio of 50 was reported [27, 28].

A flat beam is desired in an electron-positron linear collider, as well as in some accelerator-based novel light sources.

For linear colliders

At the interaction point of a linear electron-positron collider, the particles in one bunch passing through the opposite bunch are subject to a very strong transverse electromagnetic focusing force. As a result, the particles bend and radiate. This

---

1. NICADD is an acronym for Northern Illinois Center for Accelerator and Detector Development.

radiation is called "beamstrahlung" [29, 30]. As particles lose energy due to beam-strahlung, a large energy spread is introduced in the center-of-mass collision energy. Moreover, photons produced by beamstrahlung are sources of background in the detector, as photons can convert into low-energy electron-positron or muon pairs, which can lead to unacceptable levels of background in the detector.

For a Gaussian bunch, the beamstrahlung parameter is related to the rms beam sizes σ_x, σ_y and σ_z through [29]

$$\Upsilon = \frac{5}{6} \frac{N r_e^2 \gamma}{\alpha \sigma_z (\sigma_x + \sigma_y)},\tag{2.6}$$

where N is the number of particles per bunch, r_e is the classical electron radius, and α is the fine structure constant. On the other hand, the geometrical luminosity of a collider can be written as

$$\mathcal{L}_0 = \frac{N^2 f}{4\pi \sigma_x \sigma_y},\tag{2.7}$$

where f is the collision frequency.

Considering both Eq. (2.6) and Eq. (2.7), we can see that a flat beam with $\sigma_x \gg \sigma_y$ at the interaction point helps to reduce the beamstrahlung effect while keeping the luminosity high. For example, the TESLA[2] 500 GeV design has $\sigma_x = 554$ nm, $\sigma_y = 5.0$ nm, and the corresponding normalized emittances are $\varepsilon_{nx} = 10$ mm-mrad, $\varepsilon_{ny} = 0.03$ mm-mrad.

The photoinjector production of a flat electron beam is attractive since it could eliminate the need for an electron damping ring [24].

For light sources

For some accelerator-based light sources, a flat electron beam is beneficial. One example is the Linac/Laser-Based Ultra-fast X-Ray Facility (LUX) project proposed at Lawrence Berkeley National Laboratory [31, 32]. In this proposal, a flat beam

---

2. TESLA stands for TeV Energy Superconducting Linear Accelerator, which is a proposal for a linear collider where both the electron and positron accelerators incorporate superconducting rf technology.

generated by a photoinjector is accelerated to ~ 2.5 GeV and is used to generate ultra-short X-ray pulses. First, the electron bunches receive a time-correlated vertical kick in a dipole-mode cavity, introducing a correlation between the transverse momentum amplitude of the electron and its longitudinal position within the bunch. When the electron bunches radiate in the undulator downstream, they imprint such correlation to the geometrical distribution of the X-ray pulses. The correlated X-ray pulses can then by compressed using asymmetrically cut crystals [33]; see Figure 2.3.
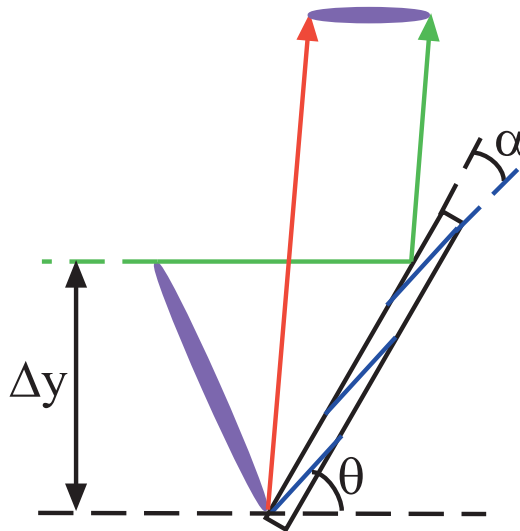
Figure 2.3: Compression of X-ray pulse by using a asymmetrically cut crystal with variable optical path length.

Let α be the angle between the crystal lattice plane and surface, and θ be the Bragg angle, see Figure 2.3. The optical path length difference Δl is related to the pulse vertical height Δy through

$$\Delta l = \frac{2\sin\theta \, \sin\alpha}{\sin(\theta + \alpha)}\Delta y. \tag{2.8}$$

The final X-ray pulse duration is related to the smaller transverse (usually vertical) dimension of the flat electron beam. X-ray pulses of the duration 100 fs or less are envisioned using this technique.

Recently, Smith-Purcell radiation [34] light sources have drawn interest, such as a Smith-Purcell radiator [35] or an image charge undulator [36], in which a "sheet" beam

(a)   (b)
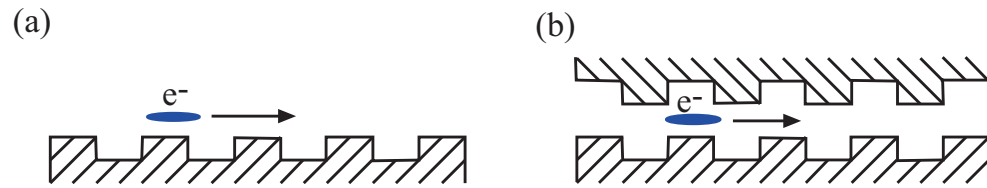
Figure 2.4: Smith-Purcell radiation based light sources: (a) Smith-Purcell radiator; (b) image charge undulator.

interacts with one or two planar metallic grating surfaces, as in Figure 2.4. A flat beam can be used in this kind of configuration as its very small vertical emittance would allow the beam to stay close to the grating surface over a long longitudinal distance, therefore enhancing the beam-surface interaction. This enhancement shortens the gain length for coherent radiation, making the use of a flat beam very attractive.

CHAPTER 3
PRINCIPLES OF ROUND-TO-FLAT BEAM
TRANSFORMATION

3.1   Introduction

In most of the existing photoinjectors, the drive-laser transverse profile is cylindrically symmetric. This property is inherited by the electrons emitted from the cathode. Since other beamline elements, such as the rf gun and the solenoids around it, are cylindrically symmetric to first order, the electron beam retains its cylindrical characteristics. Furthermore, in order to deliver a high-brightness electron beam with minimal transverse emittances, the magnetic field on the photocathode is tuned to zero as explained in Section 2.2. So upon exiting the rf gun and the solenoidal field, there is no coupling between the two transverse phase spaces. Therefore the natural beam produced in a photoinjector is round and uncoupled in the two transverse trace spaces (x, x') and (y, y'). However, this kind of beam cannot be manipulated into a flat beam. It is shown in Appendix A that "if a beam is uncoupled at the beginning of a system, and the initial x and y emittances are equal, i.e., if $\varepsilon_{x0} = \varepsilon_{y0}$, then at *all* points downstream, the projected emittances ε_{x1} and ε_{y1} will also be equal to each other" [9].

To produce a flat beam in a photoinjector, one might consider two different approaches. One way is to generate an asymmetric electron beam directly on the photocathode using a flat laser spot. This option was studied numerically by Rosenzweig in the early nineties [37, 38]. However the smaller emittance of the asymmetric beam obtained this way is below the requirement of some possible applications, and more complicated rf accelerating structures might be necessary [39]. In this dissertation, we adopt a simpler and more effective approach, i.e., introducing significant transverse coupling to a cylindrically symmetric beam on the cathode and transforming such a beam into a flat beam later. The coupling can be achieved by applying a large (e.g., of the order of $10^2 - 10^3$ Gauss) longitudinal magnetic field on the photocathode. The electron beam is born with a large canonical angular momentum which dominates the

beam dynamics. Such a beam has the potential to be transformed into a flat beam with high transverse emittance ratio. We call the beamline assembly which performs such manipulation the *round-to-flat beam transformer*, or in short, the transformer.

Before we proceed with a more rigorous theory of flat-beam generation, it is interesting to gain some insights through a simple-minded model [40]. Consider four particles with the following coordinates of an angular-momentum-dominated beam:

$$U_{1,0} = \begin{bmatrix} 0 \\ 1 \\ 1 \\ 0 \end{bmatrix}, \quad U_{2,0} = \begin{bmatrix} 1 \\ 0 \\ 0 \\ -1 \end{bmatrix}, \quad U_{3,0} = \begin{bmatrix} 0 \\ -1 \\ -1 \\ 0 \end{bmatrix}, \quad U_{4,0} = \begin{bmatrix} -1 \\ 0 \\ 0 \\ 1 \end{bmatrix}; \qquad (3.1)$$

see Figure 3.1 (a).
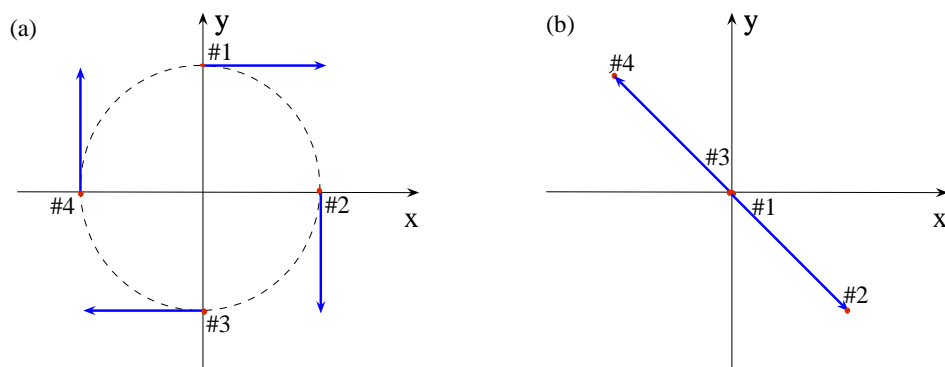
Figure 3.1: Four electrons (#1, #2, #3, and #4) in an angular-momentum-dominated electron beam [see (a)] are aligned diagonally after passing through the transformer, inside which the (y, y') coordinates are rotated by $90°$ comparing to (x, x') [see (b)].

Let M be the transfer matrix of the transformer. If M is such that it rotates the (y, y') coordinates by $90°$ compared to (x, x'), i.e.,

$$M = \begin{bmatrix} 1 & 0 & 0 & 0 \\ 0 & 1 & 0 & 0 \\ 0 & 0 & 0 & 1 \\ 0 & 0 & -1 & 0 \end{bmatrix}, \qquad (3.2)$$

then from Eq. (1.26), the coordinates of the four particles at the transformer exit are:

$$U_1 = \begin{bmatrix} 0 \\ 1 \\ 0 \\ -1 \end{bmatrix}, \quad U_2 = \begin{bmatrix} 1 \\ 0 \\ -1 \\ 0 \end{bmatrix}, \quad U_3 = \begin{bmatrix} 0 \\ -1 \\ 0 \\ 1 \end{bmatrix}, \quad U_4 = \begin{bmatrix} -1 \\ 0 \\ 1 \\ 0 \end{bmatrix}; \qquad (3.3)$$

see Figure 3.1 (b). All the electrons on the dashed circle in Figure 3.1 (a) go through similar changes, i.e.:

$$\left. \begin{array}{l} x_0 = a\cos\theta \\ y_0 = a\sin\theta \end{array} \right\} \Rightarrow \left\{ \begin{array}{l} x = a\cos\theta = x_0, \\ y = -a\sin(\theta + \pi/2) = -x_0, \end{array} \right. \qquad (3.4)$$

where a is the radius of the circle ($a = \sqrt{2}$), and θ is the angle of the radius with respect to x-axis. We see that the round beam is made flat diagonally and it will remain so in a free space since the electron velocities, if non-zero, are along the diagonal line.

If one wishes to make the beam flat horizontally or vertically, the transformer can be rotated by $45°$ around the z-axis.

In the following sections, we will see that a flat beam can be generated from an angular-momentum-dominated beam using three quadrupoles separated by drifts. The quadrupoles are *skewed* in order to have the beam flat horizontally or vertically.[1]

3.2   Beam matrix formulation

The theory of generating a flat beam from an incoming angular-momentum-dominated beam is treated in several papers [24, 25, 41, 42]. In this section, we follow the theoretical treatment based on the 4-D beam matrix presented in Ref. [42], in which the round-to-flat beam transformation analysis was performed assuming that the beam and the transport channel upstream of the transformer are cylindrically

---

1. A normal quadrupole focuses the beam either horizontally or vertically. Rotating a normal quadrupole around z-axis by $45°$ results in a skew quadrupole. Therefore, a skew quadrupole focuses the beam in the one of the diagonal directions in the transverse plane.

symmetric and that the particle dynamics is Hamiltonian.

We will specify the coordinates of a particle in transverse trace space by two vectors:

$$X = \begin{bmatrix} x \\ x' \end{bmatrix} \text{ and } Y = \begin{bmatrix} y \\ y' \end{bmatrix}. \tag{3.5}$$

The corresponding 4×4 beam matrix is

$$\Sigma = \begin{bmatrix} \langle X\widetilde{X} \rangle & \langle X\widetilde{Y} \rangle \\ \langle Y\widetilde{X} \rangle & \langle Y\widetilde{Y} \rangle \end{bmatrix}. \tag{3.6}$$

Let R be the 4×4 rotation matrix:

$$R = \begin{bmatrix} I \cdot \cos\theta & I \cdot \sin\theta \\ -I \cdot \sin\theta & I \cdot \cos\theta \end{bmatrix}, \tag{3.7}$$

where I stands for the 2×2 identity matrix. The beam matrix is rotationally invariant if

$$\Sigma = R \cdot \Sigma \cdot R^{-1}. \tag{3.8}$$

From Eq. (3.8), we obtain

$$\langle X\widetilde{X} \rangle \cos^2\theta + \langle Y\widetilde{Y} \rangle \sin^2\theta + (\langle X\widetilde{Y} \rangle + \langle Y\widetilde{X} \rangle) \sin\theta \cos\theta = \langle X\widetilde{X} \rangle. \tag{3.9}$$

Since the rotation angle θ is arbitrary, Eq. (3.9) leads to

$$\langle X\widetilde{X} \rangle = \langle Y\widetilde{Y} \rangle, \tag{3.10}$$

$$\langle X\widetilde{Y} \rangle = -\langle Y\widetilde{X} \rangle. \tag{3.11}$$

Taking the transpose of both sides of Eq. (3.11)

$$\widetilde{\langle X\widetilde{Y} \rangle} = -\widetilde{\langle Y\widetilde{X} \rangle} = -\langle X\widetilde{Y} \rangle, \tag{3.12}$$

we find that $\langle X\widetilde{Y}\rangle$ is antisymmetric and can be written as

$$\langle X\widetilde{Y}\rangle = \mathcal{L}J, \tag{3.13}$$

where $\mathcal{L}$ is a constant related to the angular momentum L and longitudinal momentum p_z by

$$\mathcal{L} = \langle xy'\rangle = -\langle x'y\rangle = \frac{L}{2p_z}, \tag{3.14}$$

and J is the 2×2 unit symplectic matrix given by Eq. (1.23).

By expressing the beam matrix in the terms of *Courant-Snyder parameters* (also known as *Twiss parameters*) α, β (see, for example, [43]), the general form of a round beam matrix in (x, x') or (y, y') subspaces can be written as

$$\langle X\widetilde{X}\rangle = \langle Y\widetilde{Y}\rangle = \varepsilon T_0, \text{ with } T_0 = \begin{bmatrix} \beta & -\alpha \\ -\alpha & \frac{1+\alpha^2}{\beta} \end{bmatrix}, \tag{3.15}$$

where ε is the rms transverse emittance, and $|T_0| = 1$.

Gathering Eq. (3.13) and Eq. (3.15), we may write the general form of a cylindrically symmetric 4×4 beam matrix in the following convenient form:

$$\Sigma_0 = \begin{bmatrix} \varepsilon T_0 & \mathcal{L}J \\ -\mathcal{L}J & \varepsilon T_0 \end{bmatrix}. \tag{3.16}$$

Let M be the transfer matrix of the transformer which is symplectic. From Eq. (1.31), the beam matrix at the exit of the transformer is

$$\Sigma = M\Sigma_0\widetilde{M}. \tag{3.17}$$

Kim noticed two invariants associated with the symplectic transformation given by Eq. (3.17) [42]:

$$I_1 = \varepsilon_{4D} = \sqrt{|\Sigma|}, \tag{3.18}$$

$$I_2(\Sigma) = -\tfrac{1}{2}\text{Tr}(J_4\Sigma J_4\Sigma). \tag{3.19}$$

where "Tr" is the trace operator.

Suppose a proper transfer matrix M exists such that the beam matrix at the exit of the transformer is block diagonalized,

$$\Sigma = \begin{bmatrix} \varepsilon_- T_- & 0 \\ 0 & \varepsilon_+ T_+ \end{bmatrix}, \quad \text{with } T_{\pm} = \begin{bmatrix} \beta_{\pm} & -\alpha_{\pm} \\ -\alpha_{\pm} & \frac{1+\alpha_{\pm}^2}{\beta_{\pm}} \end{bmatrix}. \tag{3.20}$$

Applying Eq. (3.18) to the symplectic transformation given by Eq. (3.17), we have

$$\sqrt{|\Sigma|} = \sqrt{|\Sigma_0|} \Rightarrow \varepsilon_+ \varepsilon_- = \varepsilon^2 - \mathcal{L}^2 \tag{3.21}$$

It is easy to calculate the second invariant once we verify that

$$J T_{0,\pm} J T_{0,\pm} = -I, \tag{3.22}$$

which leads to

$$J_4 \Sigma_0 J_4 \Sigma_0 = \begin{bmatrix} -(\varepsilon^2 + \mathcal{L}^2)I & 0 \\ 0 & -(\varepsilon^2 + \mathcal{L}^2)I \end{bmatrix}, \quad \text{and}$$

$$J_4 \Sigma J_4 \Sigma = \begin{bmatrix} -\varepsilon_-^2 I & 0 \\ 0 & -\varepsilon_+^2 I \end{bmatrix}.$$

So from Eq. (3.19), we have

$$I_2(\Sigma) = I_2(\Sigma_0) \Rightarrow \varepsilon_+^2 + \varepsilon_-^2 = 2(\varepsilon^2 + \mathcal{L}^2). \tag{3.23}$$

Finally, the two transverse emittances can be derived from Eq. (3.21) and Eq. (3.23),

$$\varepsilon_{\pm} = \varepsilon \pm \mathcal{L}. \tag{3.24}$$

Eq. (3.24) gives the two transverse emittances of a completely decoupled asymmetric beam. One emittance (ε_+) can be orders of magnitude higher than the other (ε_-) given properly chosen initial conditions such as ε and $\mathcal{L}$.

Our tasks remain to properly construct: (1) an input beam with beam matrix Σ_0 and (2) a beam transformer with the symplectic transfer matrix M.

3.3 Conceptual design of experiment

Figure 3.2 shows the schematics of the flat-beam generation experiment. The solenoidal coils around the rf gun produce the necessary axial magnetic field on the cathode. The round-to-flat beam transformer is composed of three quadrupoles. The quadrupoles are skewed, i.e., rotated around the z-axis by $45°$ so that the beam is made flat horizontally or vertically instead of diagonally.
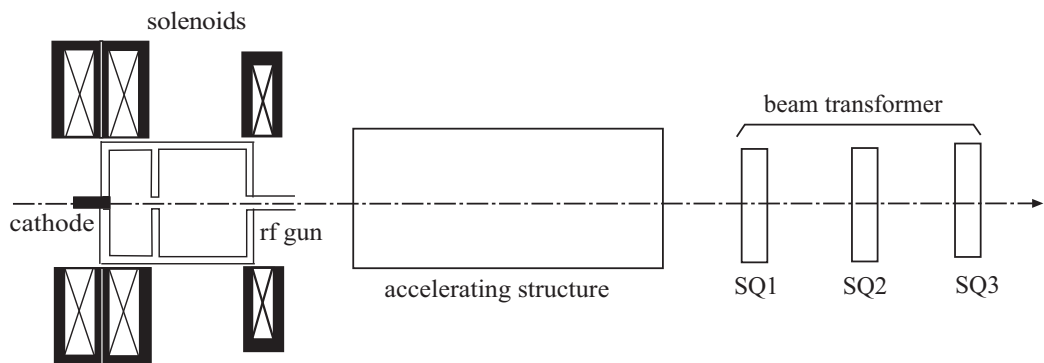
Figure 3.2: Schematic layout of the beamline setup for flat-beam generation.

Consider an electron at the photocathode surface with coordinates given by Eq. (3.5). Let B_c be the longitudinal magnetic field on the photocathode. At the exit of the solenoidal field ($B_z = 0$), the changes in the phase space coordinates x' and y', $\Delta x'$ and $\Delta y'$, are given by (see Appendix B):

$$\Delta x' = -\kappa y, \quad \Delta y' = +\kappa x,$$

where $\kappa = \frac{eB_c}{2p_z}$ and x, y are assumed to be constant.

So the electron trace space coordinates become

$$X = \begin{bmatrix} x \\ x' - \kappa y \end{bmatrix}, \quad Y = \begin{bmatrix} y \\ y' + \kappa x \end{bmatrix}. \tag{3.25}$$

Assuming there is no correlated moment at the photocathode surface (i.e. $\langle xx' \rangle = \langle xy \rangle = \cdots = 0$), the beam matrix becomes

$$\Sigma_0 = \begin{bmatrix} \sigma^2 & 0 & 0 & \kappa\sigma^2 \\ 0 & \kappa^2\sigma^2 + \sigma'^2 & -\kappa\sigma^2 & 0 \\ 0 & -\kappa\sigma^2 & \sigma^2 & 0 \\ \kappa\sigma^2 & 0 & 0 & \kappa^2\sigma^2 + \sigma'^2 \end{bmatrix}, \tag{3.26}$$

where $\sigma^2 = \langle x^2 \rangle = \langle y^2 \rangle, \sigma'^2 = \langle x'^2 \rangle = \langle y'^2 \rangle$.

Σ_0 is in the form of Eq. (3.16) with the following identifications:

$$\begin{aligned} \mathcal{L} &= \kappa\sigma^2, \\ \varepsilon &= \sqrt{\varepsilon_u^2 + \mathcal{L}^2}, \quad \text{where} \ \varepsilon_u = \sigma\sigma', \\ \alpha &= 0, \quad \beta = \frac{\sigma^2}{\sqrt{\varepsilon_u^2 + \mathcal{L}^2}}, \end{aligned} \tag{3.27}$$

where ε_u can be interpreted as the uncorrelated transverse rms emittance.

From Eq. (3.24), the expected flat-beam emittances are

$$\varepsilon_\pm = \sqrt{\varepsilon_u^2 + \mathcal{L}^2} \pm \mathcal{L}. \tag{3.28}$$

For $\mathcal{L} \gg \varepsilon_u$, we have

$$\varepsilon_+ = 2\mathcal{L}, \quad \varepsilon_- = \frac{\varepsilon_u^2}{2\mathcal{L}}, \ \text{and} \ \frac{\varepsilon_+}{\varepsilon_-} \approx \left(\frac{2\mathcal{L}}{\varepsilon_u}\right)^2. \tag{3.29}$$

Now we have obtained the input beam matrix Σ_0. The next step is to construct a beam transformer with symplectic transfer matrix M that can block diagonalize Σ_0. In the following discussion, we will see that such a beam transformer can be made of three skew quadrupoles separated by drift spaces [26].

The 4×4 transfer matrix for three normal quadrupoles separated by drift spaces

is of the following form:

$$M_{NQ} = \begin{bmatrix} A & 0 \\ 0 & B \end{bmatrix}. \tag{3.30}$$

A $45°$ rotation transformation on M_{NQ} gives the transfer matrix of the transformer:

$$M = R^{-1} M_{NQ} R, \tag{3.31}$$

where R is given by Eq. (3.7) with $\theta = 45°$. Carrying out the transformation, we have

$$M = \frac{1}{2} \begin{bmatrix} A_+ & A_- \\ A_- & A_+ \end{bmatrix}, \quad \text{with } A_\pm = A \pm B. \tag{3.32}$$

If the beam matrix at the exit of the transformer given by Eq. (3.17) is block diagonalized, the XY coupling components vanish:

$$\varepsilon(A_+ T_0 \widetilde{A_-} + A_- T_0 \widetilde{A_+}) + \mathcal{L}(A_+ J \widetilde{A_+} - A_- J \widetilde{A_-}) = 0. \tag{3.33}$$

Try a solution to Eq. (3.33) with

$$A_- = A_+ S, \tag{3.34}$$

where S is symplectic. The second term of Eq. (3.33) vanishes because $|S| = 1$. The first term also vanishes if

$$T_0 \widetilde{S} + S T_0 = 0. \tag{3.35}$$

Since T_0 is symmetric, we have

$$S T_0 = -T_0 \widetilde{S} = -\widetilde{S T_0}. \tag{3.36}$$

Therefore $S T_0$ is antisymmetric. On the other hand, since $|T_0| = |S| = 1$, we have $S T_0 = \pm J$. So

$$S = \pm J T_0^{-1} = \pm \begin{bmatrix} -\alpha & -\beta \\ \frac{1+\alpha^2}{\beta} & \alpha \end{bmatrix}. \tag{3.37}$$

Comparing with Eq. (3.15), we see that S can be determined by the elements of $\langle X\widetilde{X}\rangle$,

$$S = \begin{bmatrix} S_{11} & S_{12} \\ S_{21} & S_{22} \end{bmatrix} = \pm \frac{1}{\varepsilon} \begin{bmatrix} \Sigma_{12} & -\Sigma_{11} \\ \Sigma_{22} & -\Sigma_{12} \end{bmatrix}. \tag{3.38}$$

The $\langle XX\rangle$, $\langle YY\rangle$ components of the beam matrix are:

$$2\,\Sigma_{XX,YY} = \varepsilon(A_+ T_0 \widetilde{A_+} + A_- T_0 \widetilde{A_-}) \mp \mathcal{L}(A_+ J\widetilde{A_-} - A_- J\widetilde{A_+}). \tag{3.39}$$

We note that $ST_0\widetilde{S} = T_0$, and $J\widetilde{S} = -SJ = \pm T_0$, depending on the sign of S in Eq. (3.37).

If the positive sign in Eq. (3.37) is taken, the beam matrix at the exit of the transformer is

$$\Sigma = \begin{bmatrix} \varepsilon_- T & 0 \\ 0 & \varepsilon_+ T \end{bmatrix}, \quad \text{with } T = \frac{1}{2} A_+ T_0 \widetilde{A_+}\,, \tag{3.40}$$

where $\varepsilon_\pm$ is given by Eq. (3.24).

Notice that T is not necessarily diagonal even if T_0 is. However, from the symplectic conditions of M (see Appendix A), it follows that

$$\left. \begin{array}{c} |A_+/2| = |A_-/2| \\ |A_+/2| + |A_-/2| = 1 \end{array} \right\} \Rightarrow |A_\pm| = 2 \Rightarrow |T| = 1. \tag{3.41}$$

Therefore the two transverse emittances are indeed given by $\varepsilon_\pm$.

If the negative sign in Eq. (3.37) is taken, the positions of ε_- and ε_+ in Eq. (3.40) will be switched. So the choice of signs corresponds to the beam being made narrow in either the x or y plane. For the following discussion, we choose the positive sign of S.

Next, we will show that three skew quadrupoles are sufficient to produce a beam whose transfer matrix satisfies Eq. (3.34).

The 2×2 transfer matrix for a *normal* quadrupole in thin lens approximation is given by:

$$Q(q) = \begin{bmatrix} 1 & 0 \\ q & 1 \end{bmatrix}, \tag{3.42}$$

where q is the *quadrupole strength* and $q = 1/f$, f being the focal length of the quadrupole. In practical unit, q is given by

$$q[1/\text{m}] = \frac{300g[\text{T/m}]l_{\text{eff}}[\text{m}]}{pc[\text{MeV}]} \;,$$

$$(3.43)$$

where p is the particle momentum, g the gradient of the magnetic field and l_{eff} is the effective length of the quadrupole.

For a drift space of length d, the 2×2 transfer matrix is given by:

$$D(d) = \begin{bmatrix} 1 & d \\ 0 & 1 \end{bmatrix}.$$

$$(3.44)$$

Consider a beamline consisting of three normal quadrupoles, with the first two separated by a drift of distance d_2, and the last two by d_3. Given the transfer matrix A in (x, x') phase space, the coordinates of an electron,

$$X_0 = \begin{bmatrix} x_0 \\ x'_0 \end{bmatrix},$$

$$(3.45)$$

is transformed via $A \cdot X_0$ [see Eq. (1.26)], where A is

$$X_0 = \begin{bmatrix} x_0 \\ x'_0 \end{bmatrix} \text{and} A = \begin{bmatrix} 1 & 0 \\ q_3 & 1 \end{bmatrix} \begin{bmatrix} 1 & d_3 \\ 0 & 1 \end{bmatrix} \begin{bmatrix} 1 & 0 \\ q_2 & 1 \end{bmatrix} \begin{bmatrix} 1 & d_2 \\ 0 & 1 \end{bmatrix} \begin{bmatrix} 1 & 0 \\ q_1 & 1 \end{bmatrix}.$$

$$(3.46)$$

Let

$$Y_0 = \begin{bmatrix} y_0 \\ y'_0 \end{bmatrix},$$

$$(3.47)$$

Y_0 is transformed via $B \cdot Y_0$, where B is:

$$B = A(-q_1, -q_2, -q_3, d_2, d_3).$$

$$(3.48)$$

Substituting Eq. (3.46) and Eq. (3.48) into Eq. (3.34), we obtain the following

equations for $q_i(i = 1, 2, 3)$:

$$d_2 d_T S_{12} q_1^2 + d_2 S_{11} - S_{12} + d_2 d_T S_{21} - d_T S_{22} = 0,$$

$$d_2 d_3 (1 + S_{12} q_1) q_2 + (S_{12} + d_T S_{22}) = 0, \tag{3.49}$$

$$[d_T S_{11} q_1 + d_3 S_{11} q_2 + d_2 d_3 q_2 (S_{21} + q_1) + 1] q_3 + d_2 S_{11} q_1 q_2 + s_{21} + q_1 + q_2 = 0,$$

where S_{ij} is the ijth element of matrix S [see Eq. (3.38)] and $d_T = d_2 + d_3$. Eq. (3.49) yields

$$q_1 = \pm \sqrt{\frac{-d_2 S_{11} + S_{12} - d_2 d_T S_{21} + d_T S_{22}}{d_2 d_T S_{12}}},$$

$$q_2 = -\frac{S_{12} + d_T S_{22}}{d_2 d_3 (1 + S_{12} q_1)}, \tag{3.50}$$

$$q_3 = -\frac{q_1 + q_2 + d_2 S_{11} q_1 q_2 + s_{21}}{1 + (d_T q_1 + d_3 q_2) S_{11} + d_2 d_3 q_2 (S_{21} + q_1)}.$$

Notice that if the signs q_1 and S_{ij} are changed simultaneously, then q_2 and q_3 change signs too. This corresponds to the case where the beam is flat in the other transverse plane.

The solutions for q_i were first derived by Edwards in Ref. [44] with S defined as a "correlation" matrix, S^{co}, which relates X and Y through

$$Y = S^{co} X \tag{3.51}$$

In the context here, $S^{co} = S$ for zero thermal emittance [i.e., $\sigma' = 0$ in Eq. (3.26)].

In Eq. (3.50), there are two sets of solutions for the skew quadrupole strength settings. Both sets can remove the XY coupling. We will explore the difference of these two sets of solutions numerically later in Section 3.5.

3.4   Removal of angular momentum

The angular momentum of the electron beam is removed when the beam is made flat. Using the three-skew-quadrupole setup discussed in Section 3.3, we will now discuss how the torque applied by the transformer removes the angular momentum. Since a rotation of the coordinates will not change angular momentum, we will con-

sider three normal quadrupoles for simplicity of the algebra.

Consider an electron with the following phase-space coordinates:

$$X_0 = \begin{bmatrix} x_0 \\ -\kappa y_0 \end{bmatrix} \text{ and } Y_0 = \begin{bmatrix} y_0 \\ \kappa x_0 \end{bmatrix}, \tag{3.52}$$

From Eq. (3.37) (and taking the positive sign), we have

$$S = \begin{bmatrix} 0 & -1/\kappa \\ \kappa & 0 \end{bmatrix}. \tag{3.53}$$

When the electron passes through a quadrupole, a magnetic force is applied to it. For a normal quadrupole of strength q under the thin lens approximation [45],

$$F_x \propto qx\delta(t), \qquad F_y \propto -qy\delta(t). \tag{3.54}$$

So the torque is given by

$$N(q) \propto xF_y - yF_x = -2qxy\delta(t), \tag{3.55}$$

where x and y are the transverse coordinates of the electron at the quadrupole location, which can be computed through the transfer matrix of the beamline elements.

Assuming the initial beam is cylindrically symmetric, we have $\langle x_0 y_0 \rangle = 0$. So the change in average angular momentum caused by the first quadrupole $-2q_1\langle x_0 y_0 \rangle$ is zero.

The change in angular momentum caused by the second quadrupole is given by $-2q_2 x_2 y_2$, where x_2 and y_2 are given by [see Eq. (3.42) and Eq. (3.44)]

$$X_2 = D(d_2)Q(q_1)X_0, \tag{3.56}$$

$$Y_2 = D(d_2)Q(-q_1)Y_0. \tag{3.57}$$

The change in average angular momentum is then

$$\Delta\langle L\rangle_2 \propto -2q_2 x_2 y_2 = -4\kappa\sigma^2 d_2^2 q_1 q_2. \tag{3.58}$$

Similarly, at the third quadrupole location we have

$$X_3 = D(d_3)Q(q_2)D(d_2)Q(q_1)X_0, \tag{3.59}$$

$$Y_3 = D(d_3)Q(-q_2)D(d_2)Q(-q_1)Y_0. \tag{3.60}$$

The change in average angular momentum caused by the third quadrupole is given by

$$\Delta\langle L\rangle_3 \propto -2q_3 x_3 y_3 = -4\kappa\sigma^2 q_3(d_t^2 q_1 + d_3^2 q_2 - d_2^2 d_3^2 q_1 q_2^2). \tag{3.61}$$

Finally combining Eq. (3.58) and Eq. (3.61), the average angular momentum of the beam at the exit of the third quadrupole is given by:

$$\langle L\rangle \propto 2\kappa\sigma^2 - 4\kappa\sigma^2 d_2^2 q_1 q_2 - 4\kappa\sigma^2 q_3(d_t^2 q_1 + d_3^2 q_2 - d_2^2 d_3^2 q_1 q_2^2). \tag{3.62}$$

If $\langle L\rangle$ vanishes, then we have:

$$2d_2^2 q_1 q_2 + 2q_3(d_t^2 q_1 + d_3^2 q_2 - d_2^2 d_3^2 q_1 q_2^2) = 1. \tag{3.63}$$

The q's can be calculated using Eq. (3.50) where S_{ij} is given in Eq. (3.53). For simplicity of algebra, let $d_2 = d_3 = d$. We find

$$\begin{aligned}
q_1 &= \pm\sqrt{\frac{1+2d^2\kappa^2}{2d^2}}, \\
q_2 &= -2(q_1 + \kappa), \\
q_3 &= -\frac{q_1^2 - \kappa^2}{2\kappa}.
\end{aligned} \tag{3.64}$$

Consequently, the left hand side of Eq. (3.63) yields

$$2q_1 q_2 d^2 + 2q_3 d^2(4q_1 + q_2 - d^2 q_1 q_2^2) = ... = \frac{\kappa(q_1 - \kappa)}{\kappa(q_1 - \kappa)} = 1. \tag{3.65}$$

So the average angular momentum of the flat beam is indeed removed after the three properly tuned quadrupoles.

3.5   Two solutions of the round-to-flat beam transformer

In this section, we study numerically the two solutions for the transformer as shown in Eq. (3.50). The numerical code ASTRA [46] is used to propagate beam through the transformer. We model the beamline of the FNPL (see Chapter 5) in the simulations using the parameters in Table 3.1.

Table 3.1: Parameters used to generate input beam for the transformer.

parameter	value	units
rms drive laser pulse (Gaussian shape) length	3	ps
width of energy distribution on cathode	0.75	eV
magnetic field on cathode B_z	$\sim$935	Gauss
rms beam size on cathode σ_c	0.80	mm
bunch charge Q	0.50	nC
gun rf phase	25	degree
gun peak gradient	35	MV/m
booster cavity peak gradient	25	MV/m

From the beam distribution generated by ASTRA at the entrance of the transformer, the expected normalized flat-beam emittances from Eq. (3.24) are

$$\varepsilon_n^+ = 35.26 \text{ mm-mrad}, \qquad \varepsilon_n^- = 0.11 \text{ mm-mrad}.$$

Using three skew quadrupoles located at $z_1 = 4.020$ m, $z_2 = 4.371$ m, $z_3 = 5.224$ m, we start with the thin-lens approximation solutions of the skew quadrupole strengths given by Eq. (3.50). The quadrupole strengths are then optimized using a least-squares technique to minimize the x-y coupling terms of the beam matrix at the exit of the transformer and are found to be (in the unit of 1/m):

$$\text{Solution 1:} \quad q_1^1 = -1.622, \qquad q_2^1 = +2.074, \qquad q_3^1 = -2.992;$$
$$\text{Solution 2:} \quad q_1^2 = +1.643, \qquad q_2^2 = -2.574, \qquad q_3^2 = -2.964.$$

Putting these values into ASTRA, we found that the normalized flat-beam emittances achieved at the end of the transformer are:

$$\varepsilon_n^{+1} = 35.25 \text{ mm-mrad}, \qquad \varepsilon_n^{-1} = 0.12 \text{ mm-mrad};$$
$$\varepsilon_n^{+2} = 35.25 \text{ mm-mrad}, \qquad \varepsilon_n^{-2} = 0.14 \text{ mm-mrad}.$$

In Figure 3.3, the evolution of the rms beam emittances and sizes are plotted, where the smaller emittance (ε_-^n) is in the horizontal plane.

The beam distributions in (x, y), (x, x'), (y, y') are plotted in Figure 3.4 and 3.5. The solid lines are the analytical results of the trace-space rms ellipses.

Snapshots of the beam in (x, y) space immediately before and after each skew quadrupole are shown in Figure 3.6 and Figure 3.7. The origin of each arrow is the (x, y) position of an electron, and the direction and length of the arrow represent the direction and magnitude of the electron velocity. The top (middle, bottom) two snapshots are just before and after the first (second, third) skew quadrupole. If we zoom in the bottom right panels of Figure 3.6 and Figure 3.7, we can see that electrons are going inward vertically for the first solution, and outward vertically for the second solution, as shown in Figure 3.8.

From Figure 3.3 we can see that the second solution (where the signs of the quadrupole strength are $+ - -$) leads to a rapidly diverging beam in the vertical direction. So for the studies in the following two sections, the first solution for the quadrupole strengths is chosen.
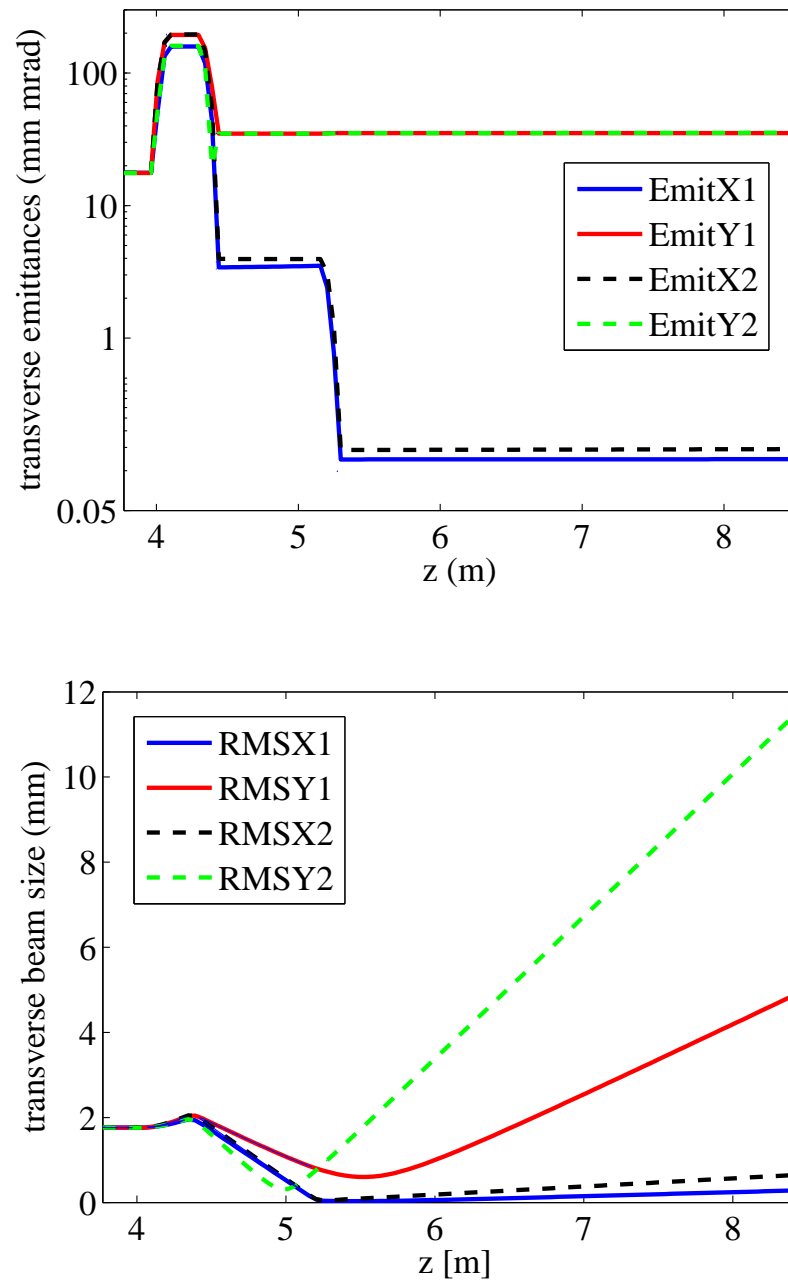
Figure 3.3: (color) The evolution of the two transverse emittances (top) and rms beam sizes (bottom) along the beamline for the two solutions of the three skew quadrupoles. Solid/dashed lines represent the first/second solution in which the quadrupole signs are - + -/+ - -.
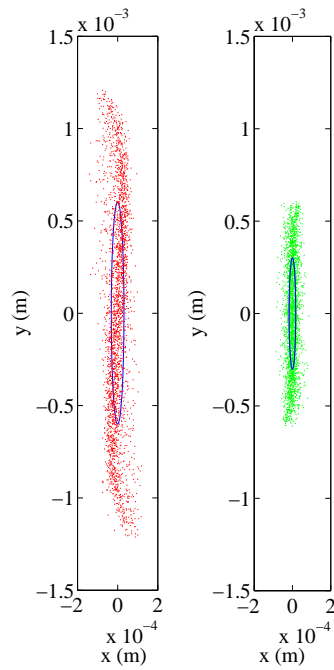
Figure 3.4: The beam profile for solution - + - (left) and + - - (right), each propagated to the its waist location.
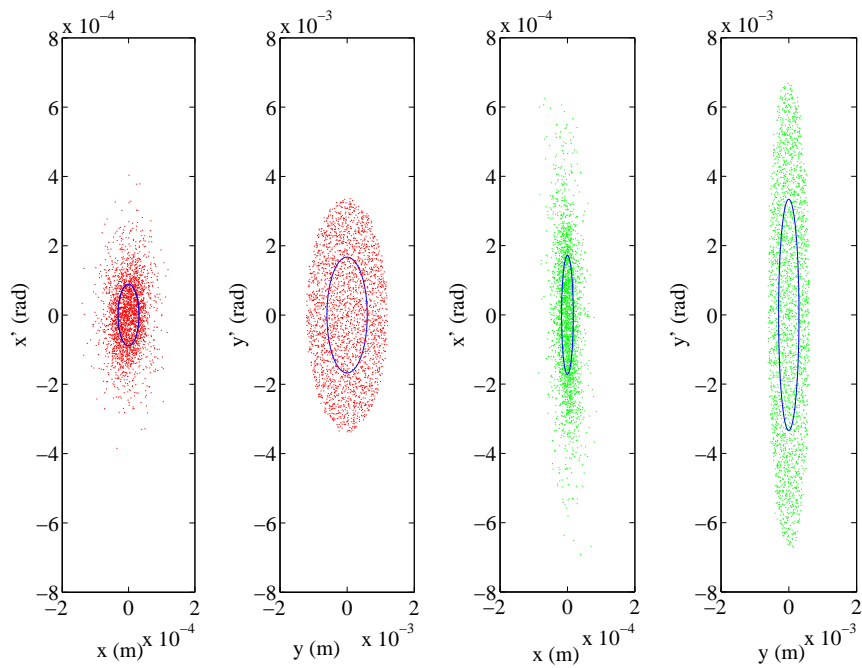
Figure 3.5: Particle distributions in (x, x') and (y, y') trace space for solution - + - (left two figures) and + - - (right two figures) at the waist locations.
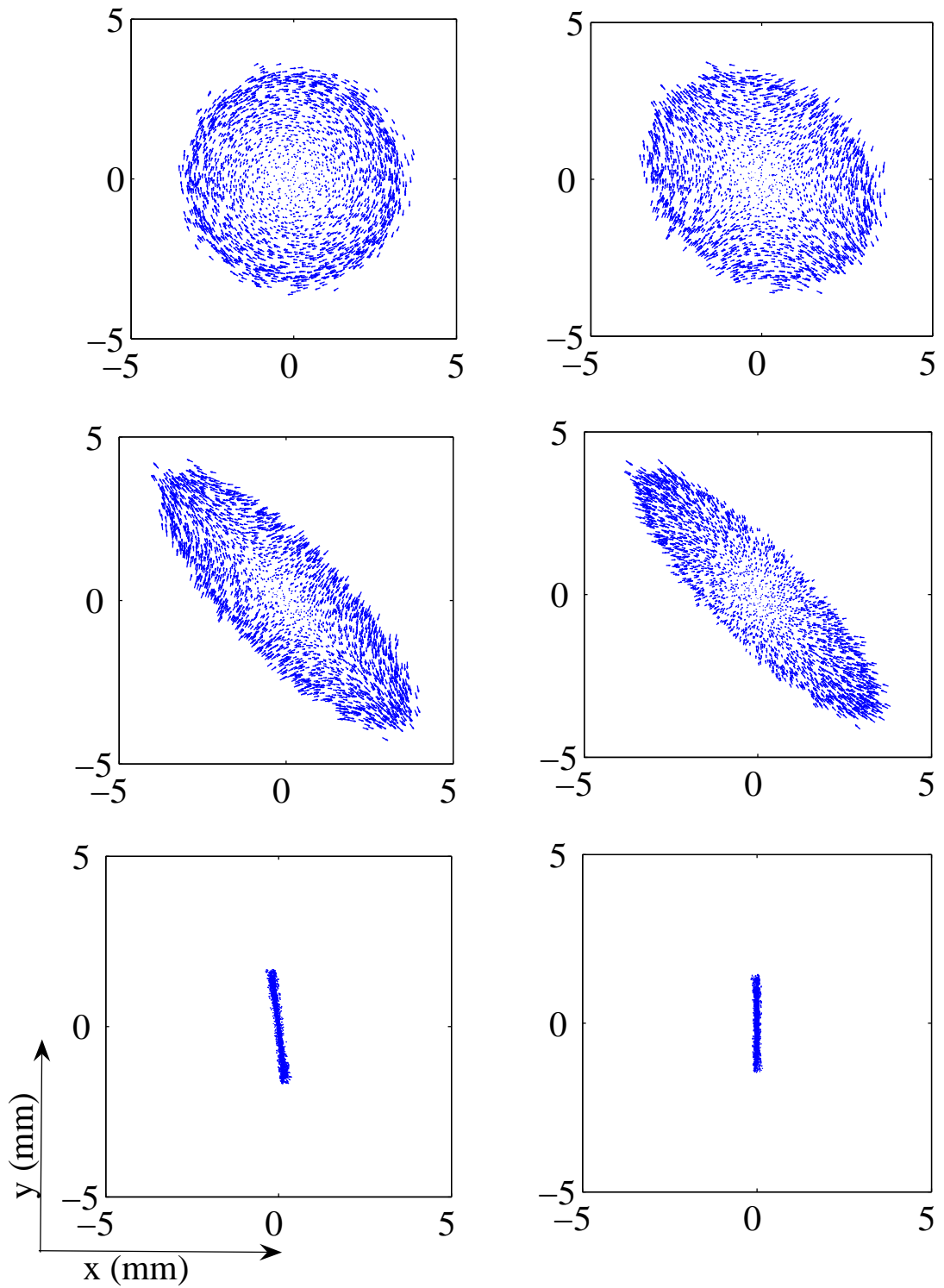
Figure 3.6: Beam during the round to flat transformation, solution - + -.
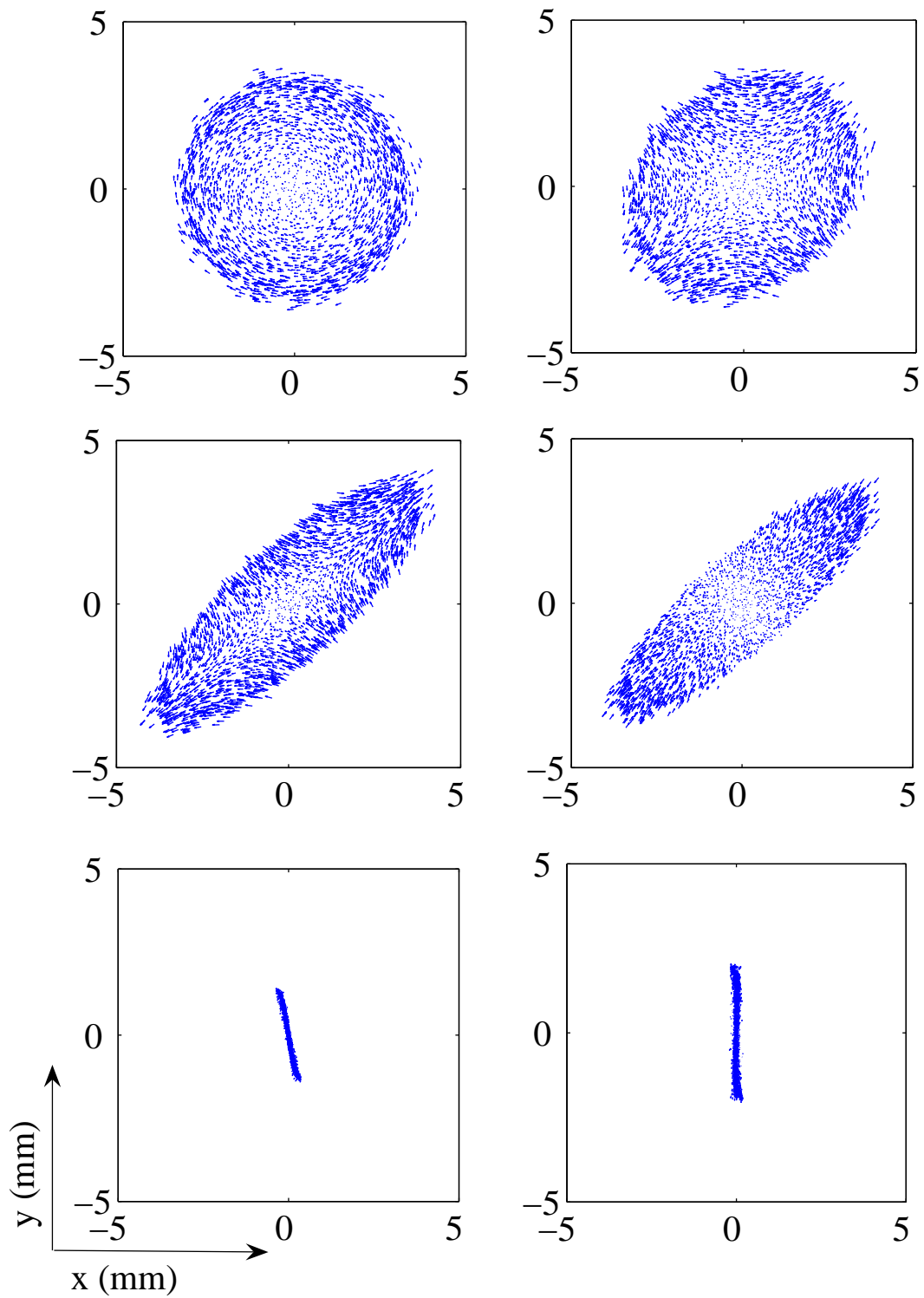
Figure 3.7: Beam during the round to flat transformation, solution + - -.
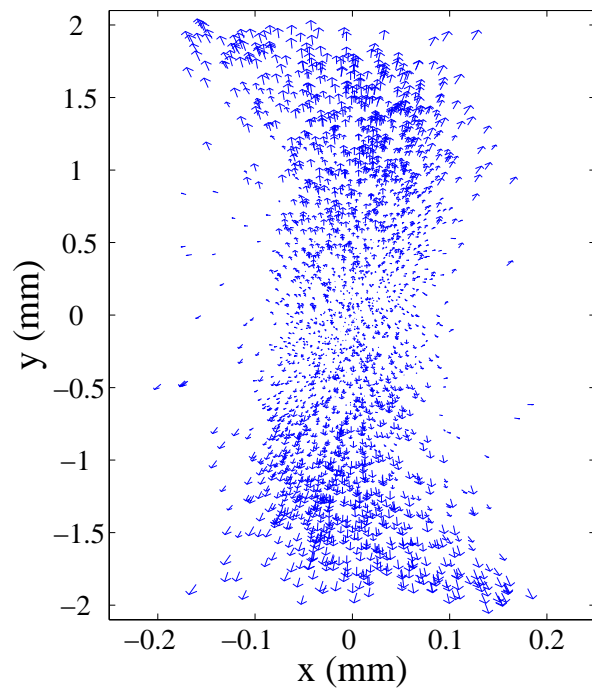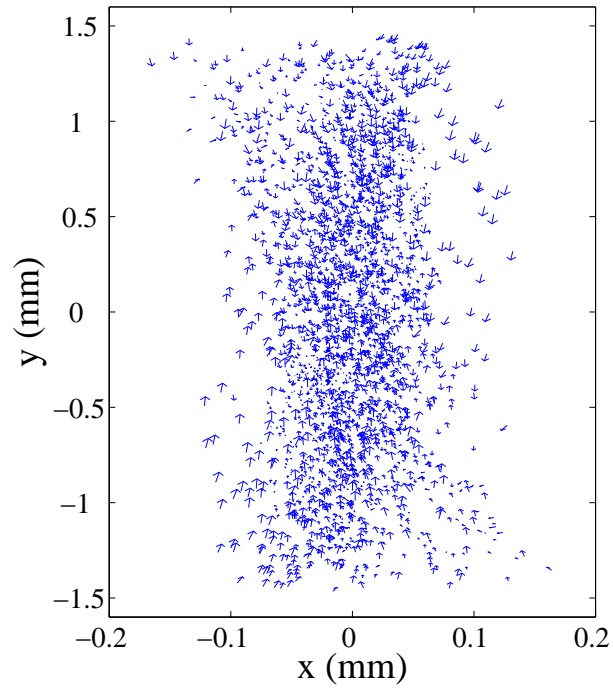
Figure 3.8: Flat beam at the exit of the transformer, solution - + - (top) and solution + - - (bottom). Note that the - + - solution converges vertically, but the + - - solution diverges vertically.

CHAPTER 4
FACTORS LIMITING FLAT-BEAM PRODUCTION

For a beam without any uncorrelated transverse emittance and energy spread, the flat-beam emittance ratio will be infinite, as indicated by Eq. (3.29). However, a real electron beam produced in a photocathode rf gun has nonzero thermal emittance. This is due to the residual thermal energy of the electrons when they are released from the photocathode. For example, for a beam emitted from a cesium telluride photocathode with a drive laser of 263 nm wavelength, the normalized thermal emittance is around 0.85 mm mrad for rms beam size around 1 mm (see Section 5.2.1). If $\gamma \mathcal{L} \approx 20$ mm-mrad, the normalized flat-beam emittances are 40.02 and 0.02 mm-mrad, leading to an emittance ratio on the order of thousands. Meanwhile, experimentally the best measured emittance ratio is about a hundred (see Chapter 6). This is partly because aside from thermal emittance, there are other effects that limit the flat-beam production, such as chromatic effects, asymmetry of the input beam to the round-to-flat beam transformer, and uncorrelated emittance growth caused by nonlinear space charge. In the following sections, we will discuss these effects.

4.1 Chromatic effects

In the case of a beam with zero energy spread, the beam matrix could be block-diagonalized upon proper choice of transfer matrix. However the beam generally has an energy spread coming from both stochastic and correlated processes. In this Section we address the related chromatic effects in the round-to-flat beam transformation.

As in Eq. (3.43), the strength of the quadrupole is related to the beam's momentum. Consider an electron with a small relative momentum deviation $\delta = \frac{p - p_0}{p_0}$ around the average beam momentum p_0. The quadrupole strength for an electron with momentum $p = p_0(1 + \delta)$ is given by

$$q[1/\text{m}] = \frac{q_0}{1 + \delta} \approx q_0(1 - \delta + \delta^2), \tag{4.1}$$

where $q_0[1/m] = \frac{300g[\text{T/m}]l_{\text{eff}}[\text{m}]}{p_0 c[\text{MeV}]}$ [see Eq. (3.43)]. Correspondingly, the transfer matrix $M_Q(q)$ may be written as:

$$M_Q(q, \delta) \approx \begin{bmatrix} 1 & 0 \\ q_0 & 1 \end{bmatrix} + \delta \begin{bmatrix} 0 & 0 \\ -q_0 & 0 \end{bmatrix} + \delta^2 \begin{bmatrix} 0 & 0 \\ q_0 & 0 \end{bmatrix}, \tag{4.2}$$

Matrices A in Eq. (3.46) and B in Eq. (3.48) become:

$$A \approx A_0 + \delta \Delta A_1 + \delta^2 \Delta A_2,$$
$$B \approx B_0 + \delta \Delta B_1 + \delta^2 \Delta B_2,$$

where the subscript "0" refers to the quadrupole strength for the particle with momentum p_0, and ΔA_i $(i = 1, 2)$ and ΔB_i are the modifications to the matrices A_0 and B_0 on the ith order of δ.

Define the following matrices:

$$\Delta_i^{\pm} = \Delta A_i \pm \Delta B_i,$$
$$\Delta_i = \frac{1}{2} \begin{bmatrix} \Delta_i^+ & \Delta_i^- \\ \Delta_i^- & \Delta_i^+ \end{bmatrix},$$

The transfer matrix of the skew-quadrupole channel takes the form

$$M(q_1, q_2, q_3, d_2, d_3) \approx M_0 + \delta \Delta_1 + \delta^2 \Delta_2, \tag{4.3}$$

where

$$M_0 = \frac{1}{2} \begin{bmatrix} A_0 + B_0 & A_0 - B_0 \\ A_0 - B_0 & A_0 + B_0 \end{bmatrix}. \tag{4.4}$$

If the distribution of the relative momentum spread is centered on the average energy, then $\langle \delta \rangle$ vanishes. From Eq. (3.6) and Eq. (4.3), keeping only the first order modification to the beam matrix, we have:

$$\Sigma \approx M_0 \Sigma_0 \widetilde{M_0} + \langle \delta^2 \rangle (M_0 \Sigma_0 \widetilde{\Delta_2} + \Delta_1 \Sigma_0 \widetilde{\Delta_1} + \Delta_2 \Sigma_0 \widetilde{M_0}). \tag{4.5}$$

As discussed in Section 3.2, the first term of Eq. (4.5) can be block diagonalized given the proper transfer matrix M. The second term can be written as:

$$\langle \delta^2 \rangle (M_0 \Sigma_0 \widetilde{\Delta_2} + \Delta_1 \Sigma_0 \widetilde{\Delta_1} + \Delta_2 \Sigma_0 \widetilde{M_0}) = \langle \delta^2 \rangle \begin{bmatrix} \Delta_{11} & \Delta_{12} \\ \Delta_{21} & \Delta_{22} \end{bmatrix}. \qquad (4.6)$$

The two transverse emittances can be calculated as the square-roots of the determinants of the top left and bottom right 2×2 sub-matrices of the beam matrix expressed in Eq. (4.5). Finally, the modified transverse emittances due to chromatic effects are

$$\varepsilon_{x,y} = \sqrt{(\varepsilon \mp \mathcal{L})^2 + \langle \delta^2 \rangle^2 [|\Delta_{11 \text{ or } 22}| + (\varepsilon \mp \mathcal{L})^2 \text{Tr}(T \Delta_{11 \text{ or } 22}^\dagger)]}, \qquad (4.7)$$

where we used the fact that for two 2×2 matrices P and Q,

$$|P + Q| = |P| + |Q| + \text{Tr}(P^\dagger Q). \qquad (4.8)$$

Here $P^\dagger = J^{-1} \widetilde{P} J$ is the symplectic conjugate of P, with J given by Eq. (1.23).

Next, we compare our analytical calculation with simulations. As an example, we choose the following operating parameters for the FNPL flat-beam experiment:

$$\begin{aligned} \gamma &= 30, & \sigma_c &= 1.00 \text{ mm}, \\ \kappa &= 0.78 \text{ m}^{-1}, & \sigma' &= 0.033 \text{ mrad}, \\ d_2 &= 0.35 \text{ m}, & d_3 &= 0.85 \text{ m}. \end{aligned}$$

Using the thin-lens approximation, and including the thermal emittance, the skew-quadrupole strengths are found from Eq. (3.50):

$$q_1 = 1.729 \text{ m}^{-1}, \quad q_2 = -1.339 \text{ m}^{-1}, \quad q_1 = 0.628 \text{ m}^{-1}.$$

The flat-beam emittances at zero relative momentum spread are calculated to be:

$$\varepsilon_n^x = 0.021 \text{ mm-mrad}, \quad \varepsilon_n^y = 46.82 \text{ mm-mrad}.$$
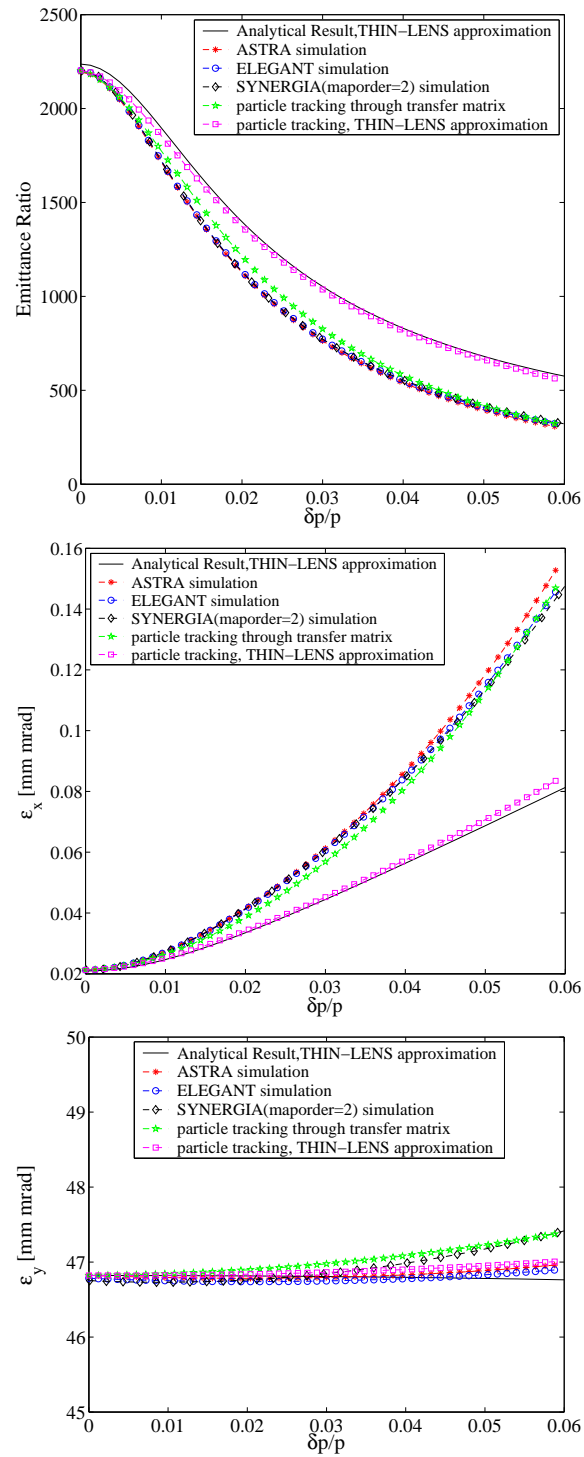
Figure 4.1: Chromatic effects on emittance ratio, horizontal and vertical emittances. Solid line is obtained from Eq. (4.7). Dashed lines with markers are numerical results.

The analytical calculations of two transverse emittances and their ratio as a function of relative momentum spread are compared with simulation results from ASTRA, ELEGANT [47] and SYNERGIA [48, 49]. These results are shown Figure 4.1. We can see that the agreement between the analytical result and simulations is better for lower relative momentum spreads. To explore further the difference, we track each particle in the simulation through the transfer matrix for both the cases when the quadrupoles are thick and thin lenses, using the transfer matrix as shown in Eq. (4.2). We found that in the thick-lens case, the tracking results almost overlap with the simulation results, while the thin-lens approximation agrees quite well with the analytical predictions. So the difference between analytical and simulation results could be explained by the fact that the thin-lens approximation is used in the analytical model to compute the skew-quadrupole strengths.

Next we study chromatic effects for different spacing between skew quadrupoles by changing d_3 from 85 cm to 35 cm, which is another possibility in the beamline at FNPL. Chromatic effects are studied in these two different cases using the analytical model and ELEGANT simulation. The results are shown in Figure 4.2.

We see that if the spacings between skew quadrupoles are $d_2 = 0.35$ m, $d_3 = 0.85$ m, the two transverse emittance values, especially the smaller one, increase more slowly as a function of relative momentum spread, and the emittance ratio decreases more slowly as well. So to reduce chromatic effects, this skew-quadrupole spacing is preferred.

Normally the rms energy spread in the beam is around 0.15%, and the chromatic effects is not significant in the transformer.

4.2 Asymmetry in the incoming beam

Some elements in the beamline, such as the rf coupler (see Figure 5.5) to the resonant cavities, could cause asymmetry in the beam before it enters the transformer. In this case, the emittances of the flat beam are affected and the flat-beam emittance ratio is lowered compared to the cylindrically symmetric beam case.

Suppose y, y' deviate from the symmetric beam by amounts ξ and ρ, respectively:

$$y \rightarrow y + \xi,$$
$$y' \rightarrow y' + \rho,$$

where ρ and ξ could be functions of y. The beam matrix at the entrance to the transformer is

$$\Sigma_0 = \Sigma_0^* + \Delta, \tag{4.9}$$

where Σ_0^* is of the form of Eq. (3.26) with $\mathcal{L}$ replaced by $\mathcal{L}^* = \kappa(\sigma^2 + \mu)$ and can be block diagonalized; Δ is given by

$$\Delta = \begin{bmatrix} 0 & 0 & 0 & -\kappa\mu \\ 0 & 0 & -\kappa\mu & 2\kappa\nu \\ 0 & -\kappa\mu & 4\mu + \langle\xi^2\rangle & 2(\mu+\nu) \\ -\kappa\mu & 2\kappa\nu & 2(\mu+\nu) & \langle\rho^2\rangle \end{bmatrix},$$

with $\mu = \frac{1}{2}\langle y\xi\rangle$, $\nu = \frac{1}{2}\langle y\rho\rangle$.

Δ introduces $x - y$ phase-space coupling terms in the beam matrix at the exit of the transformer. It also modifies the two transverse emittances of the flat beam.

As a numerical example, we use the initial beam matrix as used in previous Section, and include Δ induced by the rf gun coupler kick but propagated to the beam waist location (see Appendix C):

$$\Delta = \begin{bmatrix} 0 & 0 & 0 & 0 \\ 0 & 0 & 0 & 0 \\ 0 & 0 & 0 & 0 \\ 0 & 0 & 0 & ka_2\sigma_z^2(\sigma_y^2 + h^2) \end{bmatrix},$$

where σ_y and σ_z are the rms beam sizes, h is the difference in the vertical direction between the geometric and the electromagnetic axes due to the rf coupler kick, k is the rf wave number, $a_1 = \alpha k\sin(kl)\sin(2kz_m)$, $a_2 = \alpha k\sin(kl)\cos(2kz_m)$, where $l = z_f - z_i$, $z_m = \frac{z_f + z_i}{2}$, z_i and z_f are the start and end of the coupler region, and

$\alpha = \frac{eE_0}{2mc^2k}$ [14], where E_0 is the gun's peak accelerating field. Take the following typical values at FNPL:

$$k = 27 \text{ m}^{-1}, \ \ \alpha = 1.27,$$
$$\sigma_z = \sigma_y = 1 \text{ mm},; \ h = 1 \text{ mm } [50], \qquad (4.10)$$
$$z_i = 0.11 \text{ m}, z_f = 0.19 \text{ m}, \ \ \varepsilon_y^0 = 1 \text{ mm-mrad}.$$

Then we have $\Delta_{44} = 7.65 \times 10^{-10}$.

Applying Eq. (4.5) to the beam matrix given by Eq. (4.9), we obtain the beam matrix at the exit of the transformer including both the coupler kick and chromatic effects. For a beam with zero energy spread, we find $\varepsilon_n^- = 2.21 \times 10^{-2}$ mm-mrad, which is about 3% higher than the value without the coupler effects, and the emittance ratio drops by about 5%. In Figure 4.3, we plot the emittance ratio and horizontal emittance as functions of fractional momentum spread. In conclusion, we find that the asymmetry caused by the rf-gun coupler does not have much effect on flat-beam emittances.
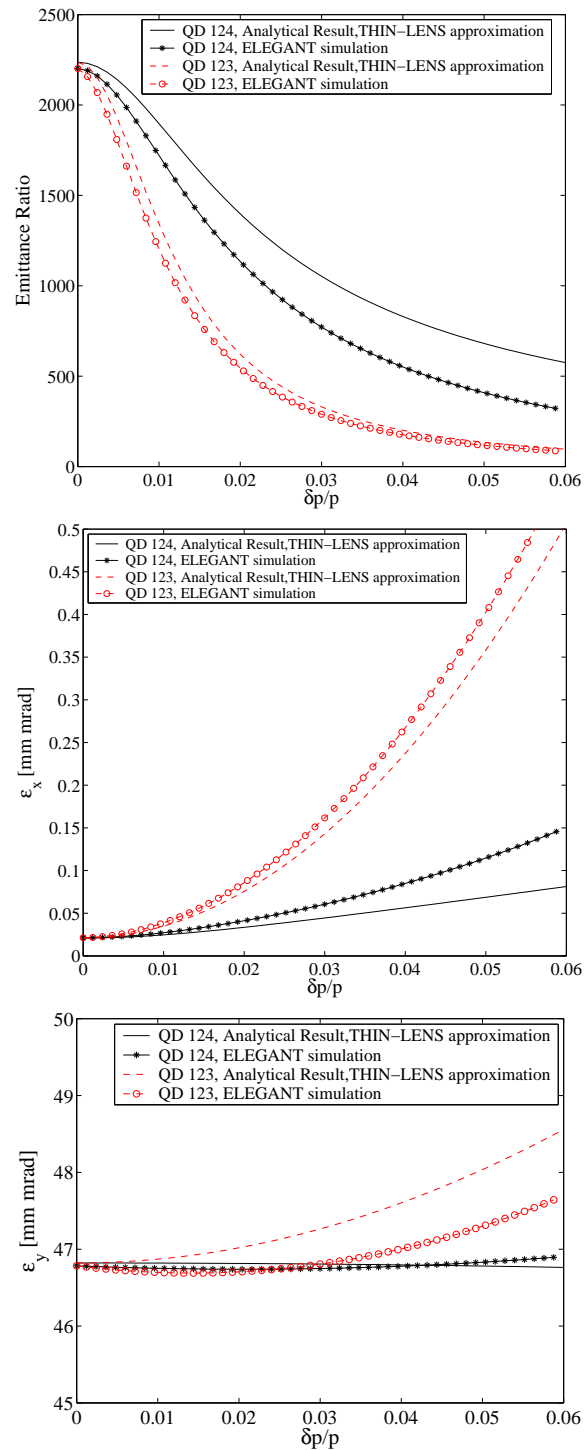
Figure 4.2: Chromatic effects on emittance ratio (top), horizontal (middle) and vertical (bottom) emittances for two cases of skew quadrupoles arrangements: case of QD 124: $d_2 = 0.35$ m, $d_3 = 0.85$ m; case of QD 123: $d_2 = d_3 = 0.35$ m.
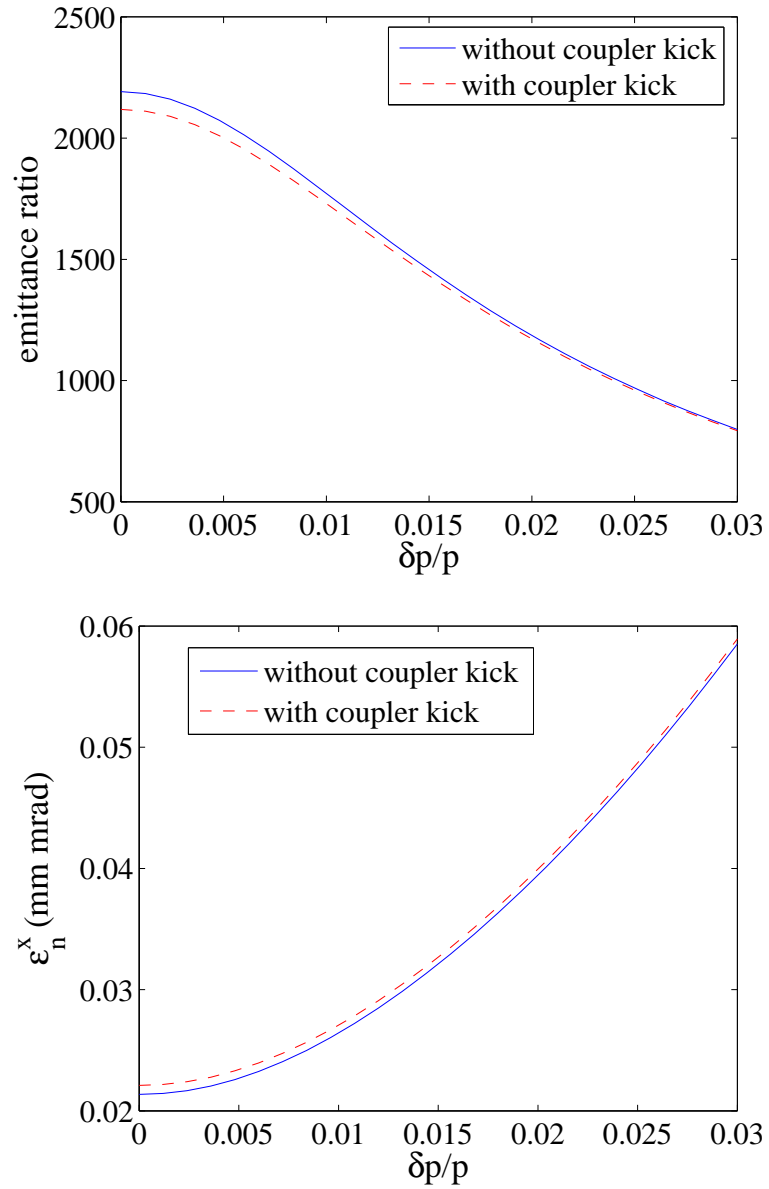
Figure 4.3: Effects on emittance ratio (top) and horizontal emittance (bottom) caused by gun rf coupler kick.

4.3 Space-charge effects

The space-charge force is the collective Coulomb-repulsion force on a particle from the other particles in the bunch or beam. As an example, let's consider a continuous beam moving along the z-axis with velocity v_z, and $v \approx v_z$. Assuming the particle density distribution ρ is uniform, then only the radial electrical field E_r and azimuthal magnetic field B_θ are nonvanishing. From Gauss's law, we have

$$E_r = \frac{\rho r}{2\epsilon_0}, \tag{4.11}$$

where ϵ_0 is the permittivity of free space. From Ampere's law, we have the magnetic field

$$B_\theta = v\frac{\mu_0\rho r}{2} = \frac{\beta}{c}E_r, \tag{4.12}$$

where μ_0 is the permeability of free space. The Lorentz force is

$$F_r = e(E_r - \beta c B_\theta) = \frac{eE_r}{\gamma^2}. \tag{4.13}$$

This is the space-charge force, which is in the radial direction in the example here. We see that while the space-charge force is always repulsive, it scales like γ^{-2}. This is a result of the repulsive electrostatic force being increasingly compensated by the magnetic field at higher energies. For bunched beams, there is also a longitudinal component of space charge, and the scaling with respect to γ is more complicated; see Ref. [14] for more discussions on space-charge effects in an rf gun and the corresponding influence on beam emittance.

Next we will first present the space-charge effects in flat-beam generation as seen in simulations. An analytical approach then follows, where we estimate the emittance growth caused by the nonlinear space-charge force and the resulting limitation on flat-beam production.

4.3.1   Simulations

Using parameters in Table 3.1, several ASTRA simulations were performed with the space charge force on and off, with the quadrupole strengths adjusted accordingly in each case. An emittance ratio larger than 1200 can be achieved with the space charge off from the start to the end of the beamline, compared to ~ 290 in the case of space charge on; see Figure 4.4.
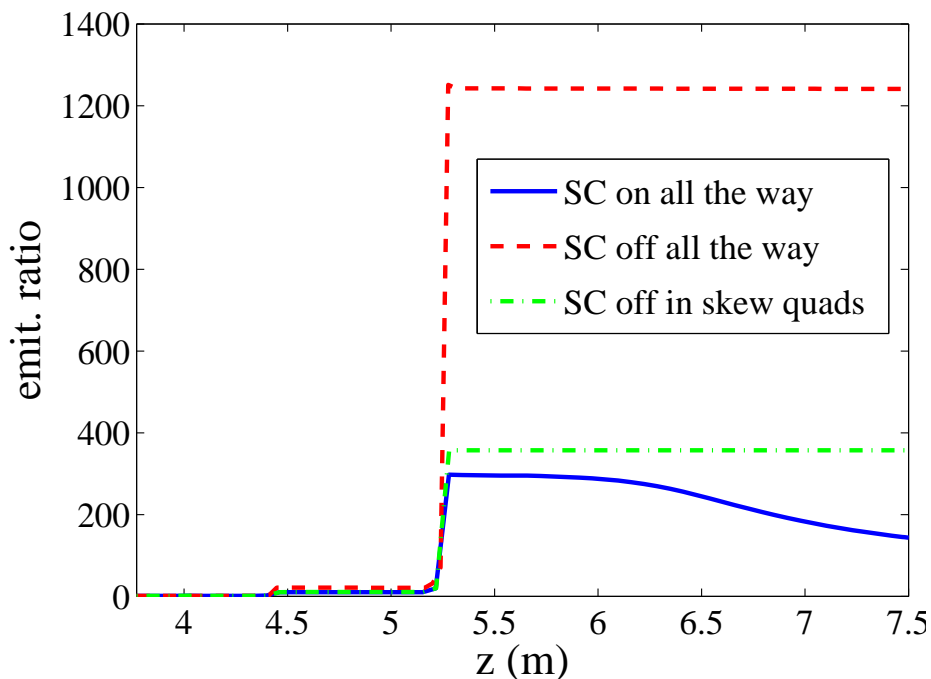
Figure 4.4: Effect of space charge on the emittance ratio.

Apart from space charge force on and off from start to end, an interesting case is having the space charge on only prior to the transformer, as shown with the green dash-dot line in Figure 4.4. We see it is closer to the case where space charge is on all the way. It is thus reasonable to conclude that space charge effects are more important prior to the round-to-flat transformer than during and/or after the transformer. This correlates to the space-charge force being proportional to $1/\gamma^2$, since during/after the transformer, the beam energy already reached its maximum in the beamline ($\simeq 17$ MeV in the example shown here.). Space charge is especially important in the rf gun, where kinetic energy increases from almost zero at the photocathode to about 4 MeV

at the gun exit.

4.3.2   Analytics

In this Section we will discuss space-charge induced emittance growth in the rf gun and its corresponding influence on flat-beam generation. Take, as a model, the space charge force to be

$$F_r \propto ar + br^3, \tag{4.14}$$

or in Cartesian coordinates,

$$\begin{aligned} F_x &\propto ax + bx(x^2 + y^2), \\ F_y &\propto ay + by(x^2 + y^2). \end{aligned} \tag{4.15}$$

The change to the dimensionless momentum $p_x = \frac{\gamma m v_x}{mc}$ caused by F_x is

$$\Delta p_x = \frac{1}{mc} \int F_x \mathrm{d}t \approx \frac{1}{mc^2} \int \frac{F_x}{\beta} \mathrm{d}z. \tag{4.16}$$

Assuming the electron's transverse coordinates remain constant in the rf gun, we can write Δp_x and Δp_y as

$$\Delta p_x = ax + bx^3 + bxy^2, \quad \Delta p_y = ay + by^3 + bx^2 y. \tag{4.17}$$

The phase-space coordinates [similar to the trace-space coordinates given in Eq. (B.4)] become

$$X = \begin{bmatrix} x \\ p_x - \kappa_n y + \Delta p_x \end{bmatrix}, \quad Y = \begin{bmatrix} y \\ p_y + \kappa_n x + \Delta p_y \end{bmatrix}, \tag{4.18}$$

where $\kappa_n = \beta\gamma\kappa$.

Assuming that $\langle x p_x \rangle = \langle x p_y \rangle = \cdots = 0$, the normalized beam matrix is

$$\Sigma_{n,sc} = \begin{bmatrix} \varepsilon_n^{sc} T^{sc} & \mathcal{L}_n J \\ -\mathcal{L}_n J & \varepsilon_n^{sc} T^{sc} \end{bmatrix}. \tag{4.19}$$

where

$$\varepsilon_{nsc}^2 = \varepsilon_n^2 + b^2 \Lambda, \quad \Lambda = \sigma^2 \sigma_6 + \sigma^4 \sigma_4 - \sigma^8 - \sigma_4^2. \tag{4.20}$$

Here $\sigma^2 = \langle x^2 \rangle = \langle y^2 \rangle$, $\mathcal{L}_n = \kappa_n \sigma^2$, $\varepsilon_n = \sigma \sqrt{p_x^2 + (\kappa_n \sigma)^2}$ [see Eq. (3.27)], and $\sigma_n = \langle x^n \rangle$ which depends on the beam distribution.

Immediately we see from Eq. (4.19) that the uncorrelated emittance increases due to the nonlinear space-charge force through parameter b; however the parameter $\mathcal{L}_n$ determined by the beam angular momentum remains unaffected. This can be understood since the space-charge force, linear or not, is in the radial direction, hence preserves the cylindrical symmetry, applies zero torque and thus conserves the angular momentum.

The normalized flat-beam emittances change correspondingly from $\varepsilon_{n,\pm}$ to $\varepsilon_{n,\pm}^{sc}$:

$$\varepsilon_n^{\pm} = \sqrt{\varepsilon_n^2 + \mathcal{L}_n^2} \pm \mathcal{L}_n \Rightarrow \varepsilon_n^{sc\pm} = \sqrt{\varepsilon_n^{sc2} + \mathcal{L}_n^2} \pm \mathcal{L}_n. \tag{4.21}$$

Next, we work out the case for a long beam whose transverse profile is Gaussian. Write the charge density as

$$\rho(r) = \rho_0 e^{-\frac{r^2}{2\sigma_r^2}} \approx \rho_0 (1 - \frac{r^2}{2\sigma_r^2} + \cdots), \tag{4.22}$$

where $\rho_0 = \frac{Q}{2\pi\sigma_r^2 l_z}$ is the normalization factor, with Q and l_z being the bunch charge and length. Only the first two terms of the expansion are considered in the following discussion. In reality, the transverse profile is taken to be a truncated Gaussian, and we can write the charge density

$$\rho(r) = \rho_0 (1 - b^* \frac{r^2}{2\sigma_r^2}), \tag{4.23}$$

where the factor b^* can be determined from the beam distribution. In Figure 4.5, the dots pertain to the observed $\rho(r)$ for a typical beam used in flat-beam experiments, and the solid line is a fit in the form of Eq. (4.23); b^* is found to be 0.3 in this case.
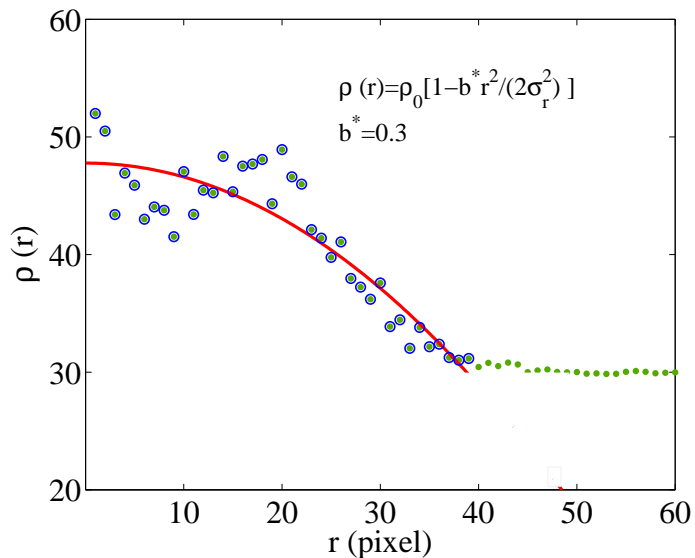
Figure 4.5: A typical beam density profile along radial direction as observed experimentally (dots) at the photocathode. The solid line is a fit in the form of Eq. (4.23) for the circled dots.

From Gauss's law, we have the radial electric field given by

$$E_r = \frac{\rho_0 r}{2\epsilon_0}(1 - b^* \frac{r^2}{4\sigma_r^2}) \tag{4.24}$$

From Ampère's law, we have the magnetic field $B_\theta = \frac{\mu_0 v r \rho}{2} = \frac{\beta}{c} E_r$. The Lorentz force is then given by:

$$F_r = \frac{eE_r}{\gamma^2}. \tag{4.25}$$

Upon substituting Eq. (4.24), Eq. (4.25) into Eq. (4.17), we have:

$$\Delta p_x = \frac{I}{I_0} \frac{\mathcal{I}}{\sigma_r^2} x(1 - b^* \frac{x^2 + y^2}{4\sigma_r^2}), \tag{4.26}$$

where $\mathcal{I} = \int \frac{1}{\beta\gamma^2} dz$ and I_0 is the Alfvén current for electrons. To calculate the integral $\mathcal{I}$, let's assume $\frac{d\gamma}{dz} = \frac{\gamma_f - 1}{z_f}$ (see Fig. 4.6) where γ_f is the final Lorentz factor; we have

$$\mathcal{I} = \frac{z_f}{\gamma_f - 1} \int \frac{1}{\beta\gamma^2} d\gamma = \frac{z_f}{\gamma_f - 1}(\frac{\pi}{2} - \sin^{-1}\frac{1}{\gamma_f}). \tag{4.27}$$

In the case of a $(n+\frac{1}{2})$-cell rf gun, we have $z_f = \frac{(n+1/2)\lambda}{2}$, where λ is the rf wavelength.
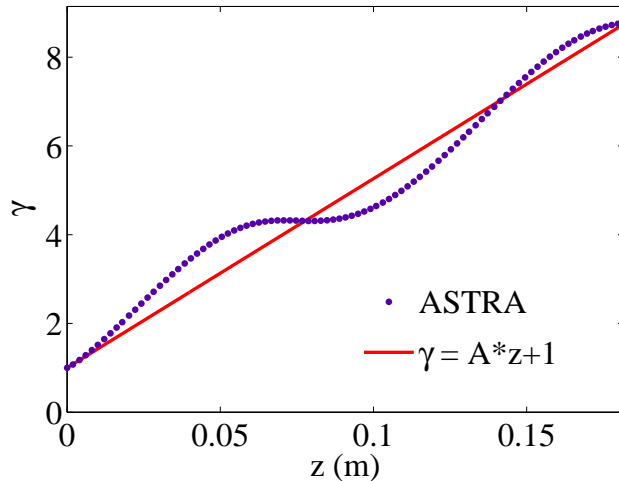
Figure 4.6: Energy gain inside a $1 + 1/2$-cell rf gun. The dots are given by numerical simulation and the solid line is a linear fit.

Eq. (4.26) is of the form Eq. (4.17) with the following identifications:

$$a = \frac{I}{I_0}\frac{\mathcal{I}}{2\sigma^2}, \quad b = -b^*\frac{I}{I_0}\frac{\mathcal{I}}{16\sigma^4}, \tag{4.28}$$

where we used $\sigma_r^2 = 2\sigma^2$ for a cylindrically symmetric beam.

From the distribution given by Eq. (4.22), we obtain

$$\Lambda = 8\sigma^8. \tag{4.29}$$

Finally, substituting Eq. (4.28) and Eq. (4.29) into Eq. (4.21), we get

$$\varepsilon_n^{sc} = \sqrt{\left(b^*\frac{I}{I_0}\frac{\mathcal{I}}{4\sqrt{2}}\right)^2 + \varepsilon_n{}^2}. \tag{4.30}$$

Take the following parameters: $b^* = 0.3$, $I = 35$ A, $\gamma_f = 9$, $z_f \approx 0.17$ m for a 1.5-cell 1.3 GHz rf gun, normalized thermal emittance $\varepsilon_n = 1$ mm-mrad. From Eq. (4.30), we obtain $\varepsilon_n^{sc} = 3.53$ mm-mrad. If $\mathcal{L}_n = 20$ mm-mrad, due to the nonlinear space-

charge force, the smaller of the two transverse flat-beam emittances increases from 0.02 to 0.30 mm-mrad, and the corresponding emittance ratio drops from 2000 to 130.

In reality, particle transverse positions change under the space-charge and external electromagnetic forces, so that the beam dynamics is much more complicated. Nevertheless the discussion here shows that the emittance growth caused by nonlinear space charge in the rf gun is the major limiting factor on achieving a flat beam with very small emittance and high emittance ratio.

4.3.3   Conclusions

Compared to the numerical example shown in Section 4.3.1 where the emittance ratio is around 300 with space charge, the analytic result is good to better than a factor of 3 compared with the simulations, despite the crude approximations.

The space charge in the gun is the dominant limiting factor for flat-beam production. Higher rf accelerating gradient at the photocathode and longer laser pulse could help to reduce the space-charge effects [24]. The most important direction for future R&D is the suppression/compensation of space charge in the rf gun when an axial magnetic field is present on the cathode.

CHAPTER 5

FERMILAB/NICADD PHOTOINJECTOR LABORATORY

5.1 Overview

The Fermilab/NICADD Photoinjector Laboratory (FNPL) produces a high brightness electron beam with energy up to 16 MeV. The facility consists of an ultraviolet (UV) photocathode-drive laser and an electron beam transport line of around 11 meters in length. The key elements of the beamline include a 1.5-cell[1] normal conducting rf gun operating at 1.3 GHz, a TESLA style 9-cell superconducting niobium cavity, a magnetic bunch compressor, and a dipole spectrometer. A drawing of the beamline is shown in Figure 5.1.

Transverse beam diagnostics such as optical transition radiation (OTR) and Yttrium Aluminum Garnet (YAG) viewers, horizontal/vertical slits, beam position monitors (BPMs) are available at various locations in the beamline.

The accelerator has the same design [51] as the injector of the TESLA Test Facility (TTF) at DESY. Apart from the production of a high-brightness electron beam [52], it has hosted several R&D experiments, including plasma wake-field acceleration, channeling radiation, electro-optic sampling [53], and flat-beam generation.

---

1. To be more accurate, it is a 1.625-cell rf gun.
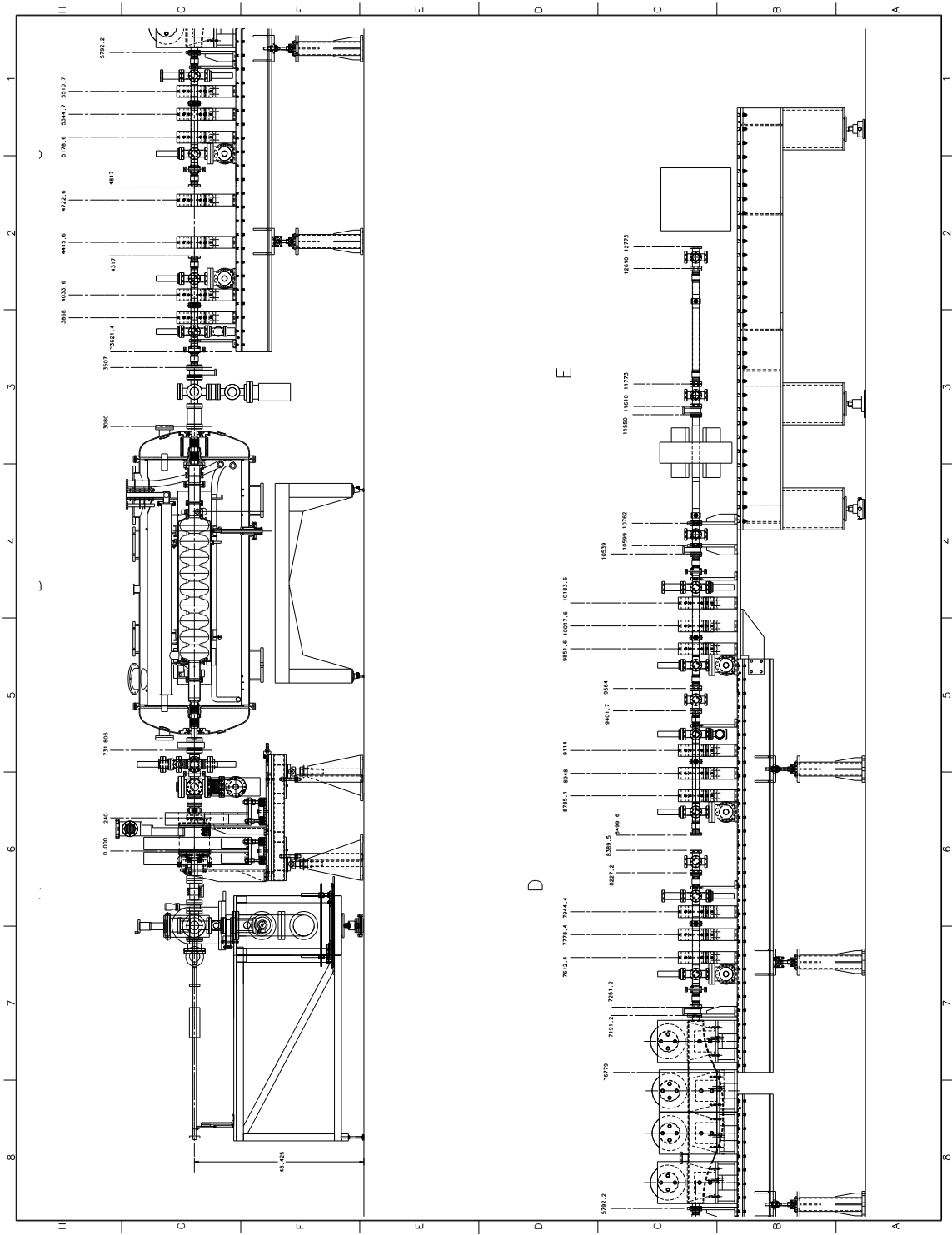
Figure 5.1: A drawing of the FNPL beamline.

5.2   Photoemission electron source

5.2.1   Photocathode

The electron bunches of FNPL are photo-emitted from a high-quantum-efficiency cesium telluride (Cs_2Te) photocathode located at the back plate of the rf gun.

The cesium telluride compound is a p-type semiconductor with a band gap of $E_G = 3.3$ eV and an electron affinity $E_A = 0.2$ eV. Powell [54] found that the first maximum in the conduction band density of states is at $E_f = 4.05$ eV above the valence band maximum, and the first maximum density of states below the valence band maximum occurs at -0.7 eV; see Figure 5.2. This means a photon energy of 4.05 eV for the first maximum photoemission peak, and 4.75 eV for the second peak.
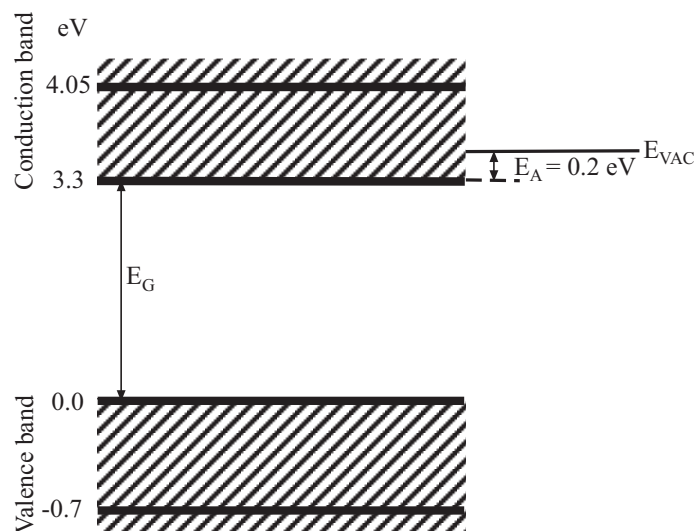
Figure 5.2: Schematic energy-level diagram of cesium telluride. The dark lines indicate the maxima of density of states.

The fourth harmonic of the Nd:YLF laser photon has an energy of 4.72 eV. For the first maximum photoemission peak (indirect transition), this leaves a kinetic energy $E_{kin} = E_f - E_G - E_A = 0.55$ eV for a free electron. The initial normalized thermal emittance of the electron beam is related to this residual kinetic energy and the rms

beam size σ on the photocathode via [55]

$$\varepsilon_n^{th} = \sigma \sqrt{\frac{2E_{kin}}{3mc^2}} \tag{5.1}$$

For example, for $\sigma = 1$ mm, we have $\varepsilon_n^{th} = 0.85$ mm-mrad.

The photocathode fabrication and transportation system at FNPL was developed at Milano [56]. Under ultrahigh vacuum (UHV), a layer of cesium telluride is coated on a molybdenum substrate in a photocathode preparation chamber. The chamber has the capacity of holding up to five photocathodes which could be used in turn. The photocathode can be transferred from the preparation chamber to the rf gun while remaining in UHV via a couple of manipulator arms; see Ref. [57] for more details.

The quantum efficiency of the photocathode varies from 0.5% to 10% depending on conditions such as cathode age, UV light energy per pulse, electromagnetic field on the photocathode, etc. [58, 59].

5.2.2   Drive laser

The FNPL photocathode-drive laser is a Nd:YLF laser quadrupled to the fourth harmonic of its IR wavelength of 1053 nm. The laser system was developed by the University of Rochester [60]. A block diagram is shown in Figure 5.3. The laser system starts with a Nd:YLF mode-locked oscillator which produces a 81.25 MHz pulse train of wavelength 1054 nm. An iris is used to select the TEM_{00} transverse mode which is Gaussian spatially. The pulses are then expanded in time through a frequency chirp in a 2 km long optical fiber. From the fiber output, a fast pulse picker selects pulses to form a 1.003 MHz pulse train. The pulses are injected into a Nd:glass multi-pass amplifier for a fixed number of passes; the pulse intensity is amplified by a factor of ~ 3000. The output of the multi-pass amplifier is fed into a two-pass amplifier containing two Nd:glass rods for a further amplification by a factor of ~ 70. Following the two-pass amplifier, the laser beam is spatially filtered and compressed using a pair of diffraction gratings. Finally, the infrared light pulses pass two stages of second-harmonic generation and are converted into UV pulses with wavelength

1054 nm

Nd:YLF oscillator
81.25 MHz

optical fiber
(2 km)

pulse picker
1 MHz

Nd:glass
multi-pass amplifier

Nd:glass
two-pass amplifier

263 nm

527 nm

1054 nm

1054 nm

BBO

BBO

grating compressor

spatial filter

to photocathode
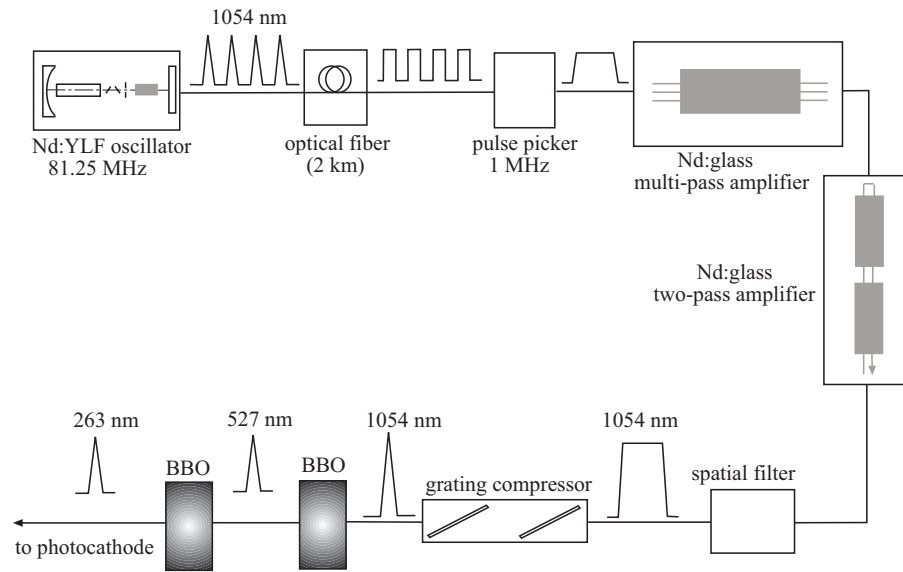
Figure 5.3: A block diagram of the FNPL laser system.

263.5 nm. The macro UV pulse train repetition rate is 1 Hz; see Figure 5.4. The energy per UV pulse could be as high as 10 μJ.

1 s

up to 800 μs

1 μs
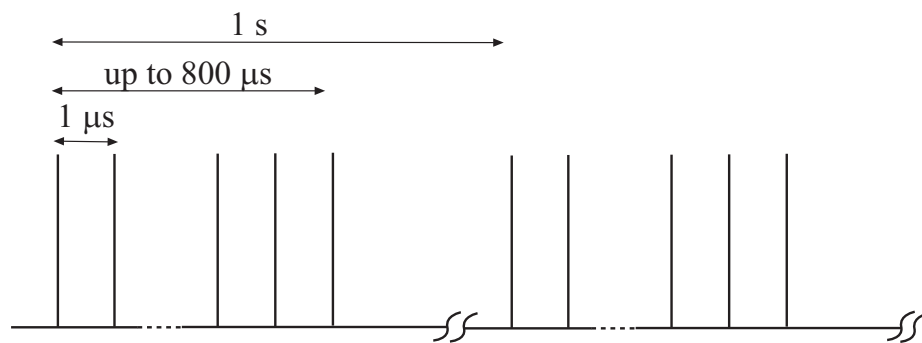
Figure 5.4: Time structure of the UV laser pulse.

The UV laser is synchronized to the rf drive of the accelerating cavities by locking onto the rf with a commercial phase-lock feedback loop. The resulting rms time jitter is less than 2 ps, which is 1 rf degree.

5.3   The rf cavities

5.3.1   The rf gun

The FNPL rf gun is a 1.5-cell copper cavity operating in TM_{010} π-mode at 1.3 GHz. The Cs_2Te photocathode is located at the back plate of the first half-cell of the gun. The full cell is side-coupled to the waveguide; see Figure 5.5.
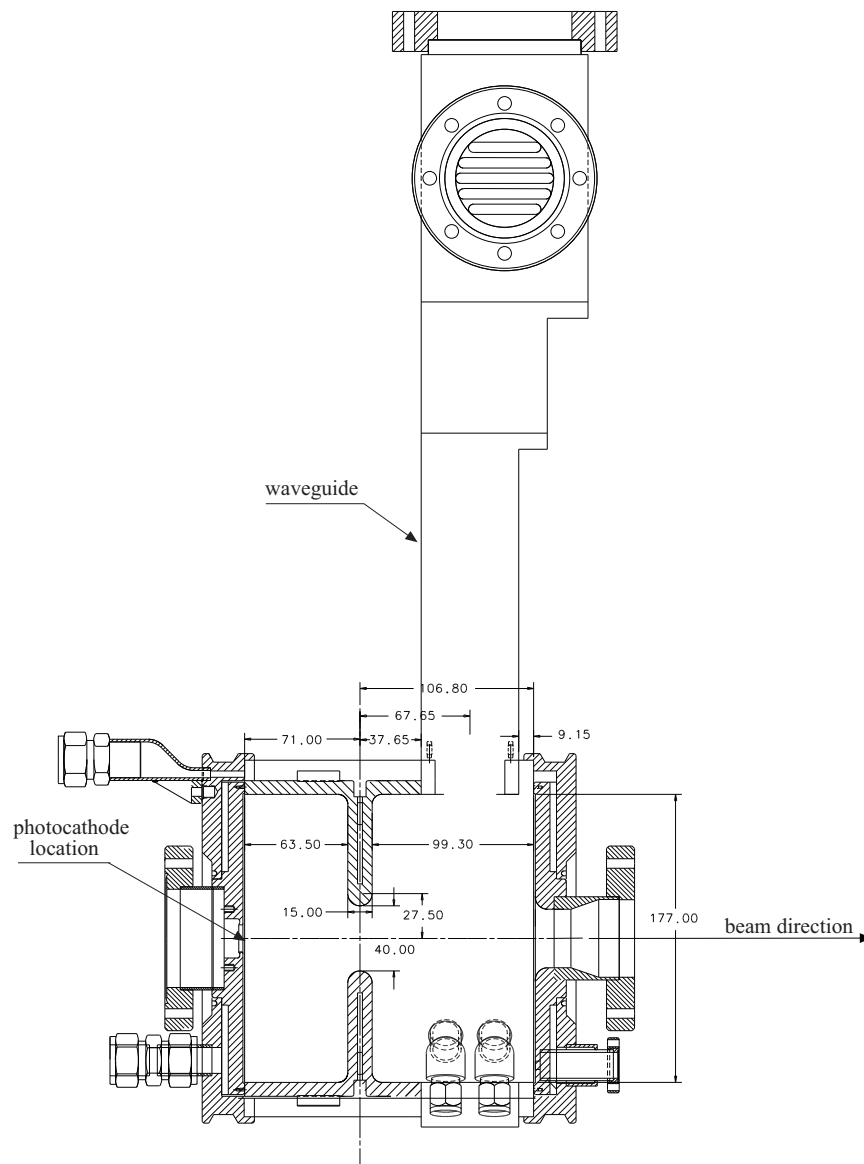
Figure 5.5: A drawing of the FNPL rf gun.

Given the geometry and material of the rf gun, numerical codes such as SUPERFISH can be used to generate its electromagnetic field. The longitudinal electric field E_z for the TM_{010} π-mode is shown in Figure 5.6.
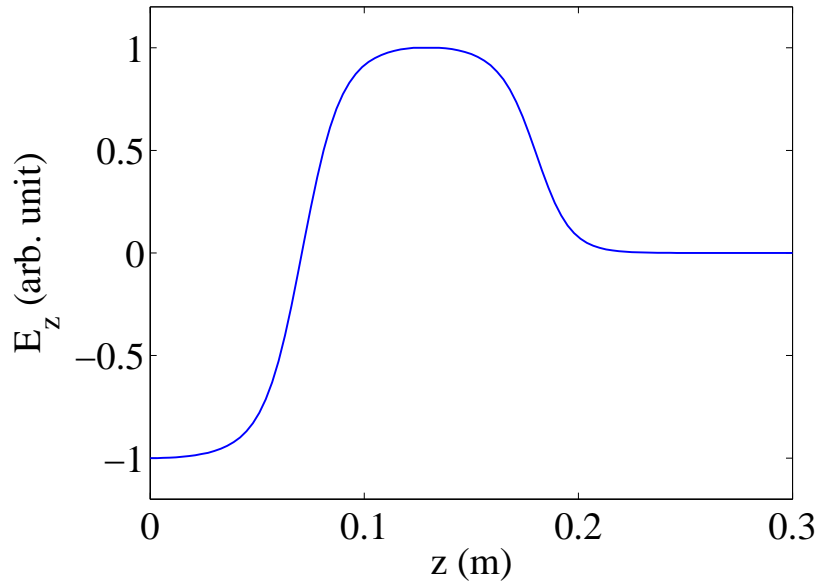
Figure 5.6: Longitudinal electric field on z-axis for the accelerating mode of the FNPL rf gun from SUPERFISH [80] simulation.

The coefficient relating the longitudinal electric field on the photocathode (E_c) and the power dissipated in the gun (P) can be obtained from SUPERFISH simulation:

$$\zeta = E_c/\sqrt{P} = 1.000 \ (\text{MV/m})/\sqrt{1.781 \times 10^{-3} \ (\text{MW})} = 23.7 \ (\text{MV/m}/\sqrt{\text{MW}}).$$
(5.2)

Using this coefficient, we can calculate the field on cathode using the following equation:

$$E_c(\text{MV/m}) = 23.7\sqrt{P(\text{MW})}.$$
(5.3)

For example, with 2.2 MW peak input rf power, the peak accelerating gradient is around 35 MV/m. The electron energy out of the gun can be up to 4.5 MeV.

Using the most recent rf calibration, the power dissipated in the gun can be

calculated from the following equation [61]

$$P(W) = \frac{\left[c_0|V_f| + c_1\ln\left(c_2|V_f|+1\right)\right]^2}{100} \cdot 10^{\left(\frac{A+C+T}{10}\right)} \tag{5.4}$$

where $|V_f|$ is the output of the forward power diode, which can be read from the control room oscilloscope, and $A = 47.42$, $C = 34.65$, $T = -0.17$, $c_0 = 0.0196$, $c_1 = 0.0446$, $c_2 = 3.642$ are calibration constants.

The gun rf phase is set through a *phase-scan* procedure where the bunch charge is measured as the relative phase between the rf and drive laser is varied. A simulation of the phase scan is shown in Fig. 5.7. The gun phase is set to less than $50°$ so that the beam at gun exit will have sufficient charge and energy.
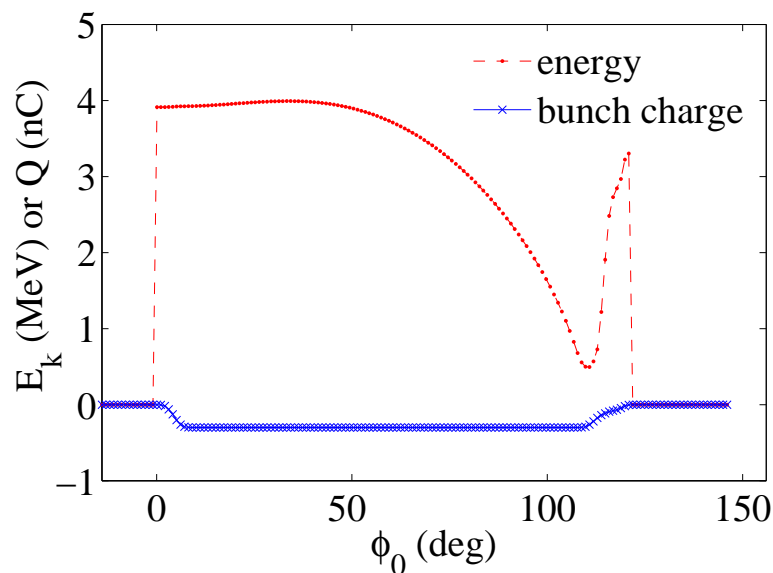
Figure 5.7: Numerical simulation of bunch charge and energy at gun exit as a function of rf phase; maximum bunch charge is set to 0.5 nC in this simulation.

5.3.2   Solenoids and beam-based alignment

Three independently powered solenoids surround the gun for beam focusing and phase-space manipulation; see Figure 5.8. In the flat-beam experiment, the solenoids also provide an axial magnetic field on the order of 10^2 to 10^3 Gauss on the photocathode.
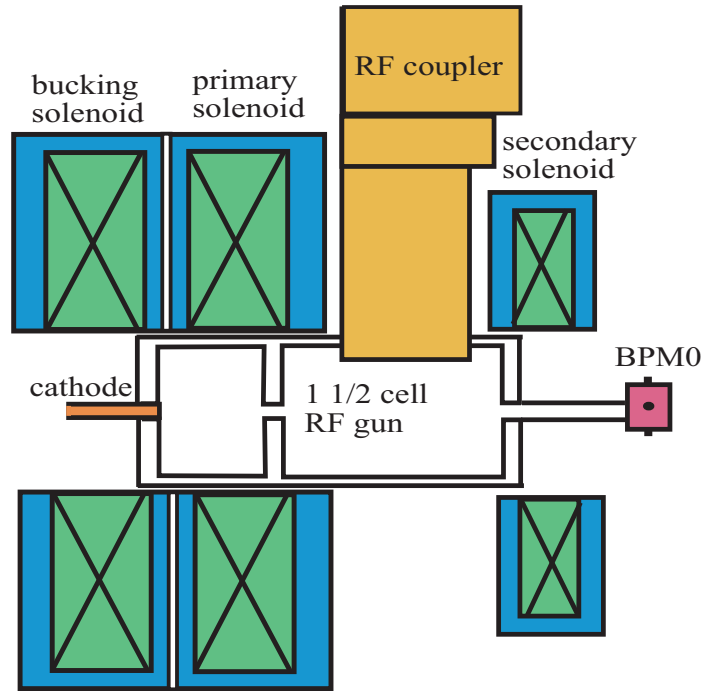
Figure 5.8: Gun, solenoids, and beam position monitor at gun exit (BPM0) used for beam-based alignments.

In operating the photoinjector, we noticed that when the solenoid currents are changed, not only the focusing of the beam along the beamline changes, but also do the beam transverse positions; see Figure 5.9. In this figure, beam positions are measured at the first BPM downstream of the rf gun (BPM0) while scanning the solenoid currents. For each one of the three solenoid current scans, the other two solenoids are turned off.

Beam missteering caused by solenoids is an undesirable effect that leads to emittance growth and complicates the procedures to center the beam in the other elements further down the beamline, such as the booster cavity, etc.
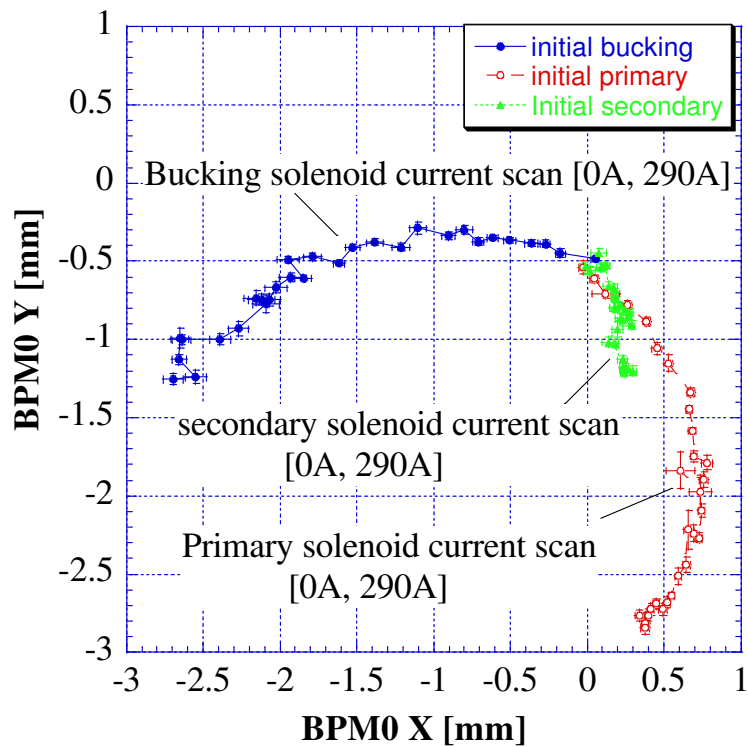
Figure 5.9: Beam positions measured by BPM0 as a function of solenoid currents before beam-based alignment.

The experimental observation mentioned above indicates there are some misalignments between the gun and the solenoids, and/or an offset of the laser light position on the cathode. Using a set of depth meters, we measured the mechanical center of the solenoid with respect to the gun surface; see Figure 5.10. It was found that, with respect to the mechanical center of the gun, the center of the primary and bucking solenoids, which are tied together, is located at $[0.8, 0.1]$ mm on the upper-west direction, and the secondary solenoid center is around $[2.3, 1.8]$ mm on the lower-east.

Following this measurement, a beam-based alignment similar to those performed at TTF [62, 63] was pursued.

To make sure that the electron beam goes through the electromagnetic axis of the rf gun and thus to minimize the steering caused by the gun field, we started the alignment by trying to find the proper laser light position on the cathode.
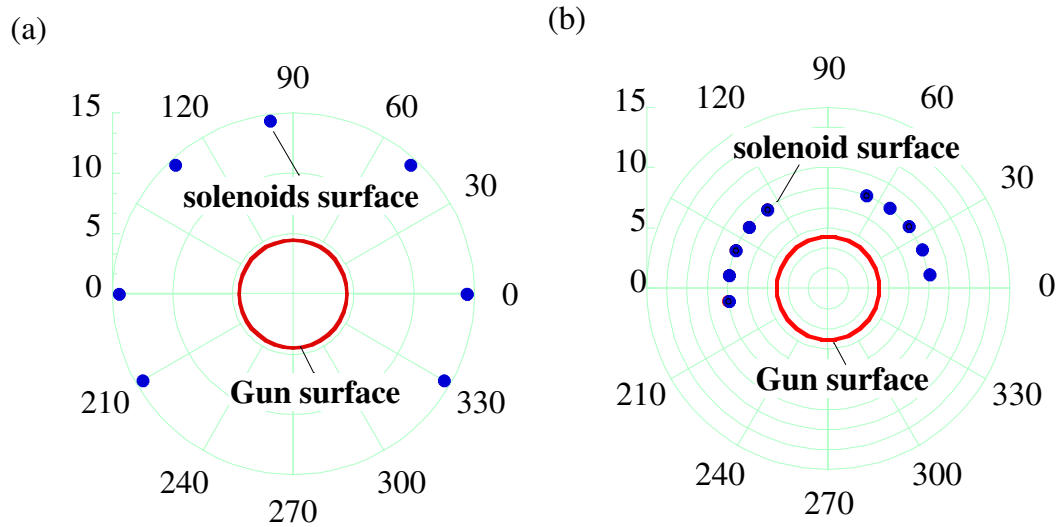
Figure 5.10: Measurement of the solenoid mechanical centers with respect to the gun surface: (a) primary and bucking solenoid; (b) secondary solenoid.

With all three solenoid currents set to zero, we varied the gun gradient and phase for several different laser light locations: the center of the cathode, and four spots around the center. The beam positions measured are shown in Figure 5.11. We see that when laser light hits the center of the cathode, the beam position changes least among the five positions when the gun gradient is varied from 14 MV/m to 38 MV/m. There is still some steering caused by the gun itself. This might be due to the gun rf coupler, which causes an asymmetry of the field and in turn gives the beam a vertical kick. Laser light is kept at the center of the cathode (see Figure 5.12) during the alignment procedures followed hereafter.

ASTRA is used to simulate the initial measurement of beam position at BPM0, as shown in Figure 5.9. Given the center location of the solenoid, beam position at BPM0 is recorded while the magnetic field strength is scanned. Each solenoid has a different longitudinal magnetic filed profile along the beamline, and the maximum of the profile is scaled with current, taking into account the saturation at high currents [52].

It is noticed that our BPM system has a left-hand cartesian system if one takes the beam propagation to be the $+z$ direction. So in the following text, in order to match the simulation with measurement, the signs of measured x values were switched.

Furthermore, from Figure 5.9, one can see that when the solenoid currents are
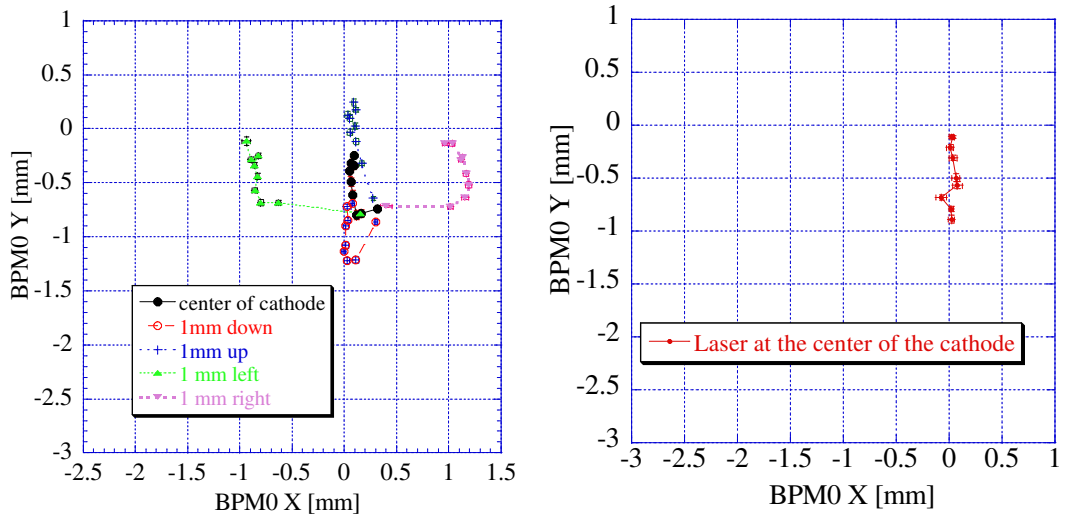
Figure 5.11: Beam positions measure by BPM0 while varying gun gradient for 5 different laser light positions on cathode. For laser light at the cathode center position, beam positions are also measured for different gun phases.

zero, BPM0 has a nonzero reading in y, so 0.5mm were added to measured y values to zero the BPM reading when the solenoid currents are zero.

When the simulation matches the initial measurement as shown in Figure 5.9, the offsets used in simulation are compared to the mechanical measurement of the solenoid center offsets shown in Figure 5.10. The results provide a guide to move the solenoids physically. Once solenoids are physically re-aligned, another set of beam position measurements under solenoid current scans was taken. After a couple of iterations, the beam position changes within 1.5 mm, comparing to 3 mm before the alignment. In figure 5.13, the beam positions under the current scan of primary and bucking solenoids before and after beam-based alignment are plotted.

For the secondary solenoid, ASTRA simulation gives an off-center of [1.5 mm , -1.0 mm], which agrees in directions with the mechanical measurement. In experiment, the solenoid center is first moved 2 mm to the west and beam positions are measured while scanning the secondary solenoid currents; then the solenoid is moved 2 mm up
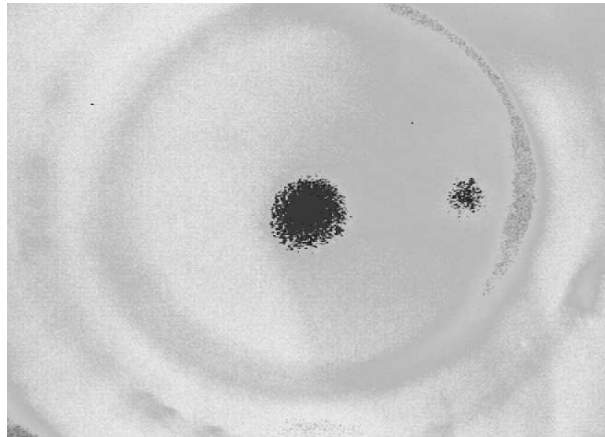
Figure 5.12: A photo of laser light on cathode. The dark spot at the center of the circle is the HeNe laser light, which is aligned along the UV laser. The small spot on the side is a reflection of the HeNe light from some components in the beamline.

before the final measurements. The final measurement of beam positions are within the accuracy of BPM0, for secondary solenoid current range from 0 A to 290 A; see Figure 5.14.

When a new gun was installed in the FNPL beamline later, the same beam-based-alignment procedure was done and similar results are obtained; see Figure 5.15 for the initial and final scenarios.
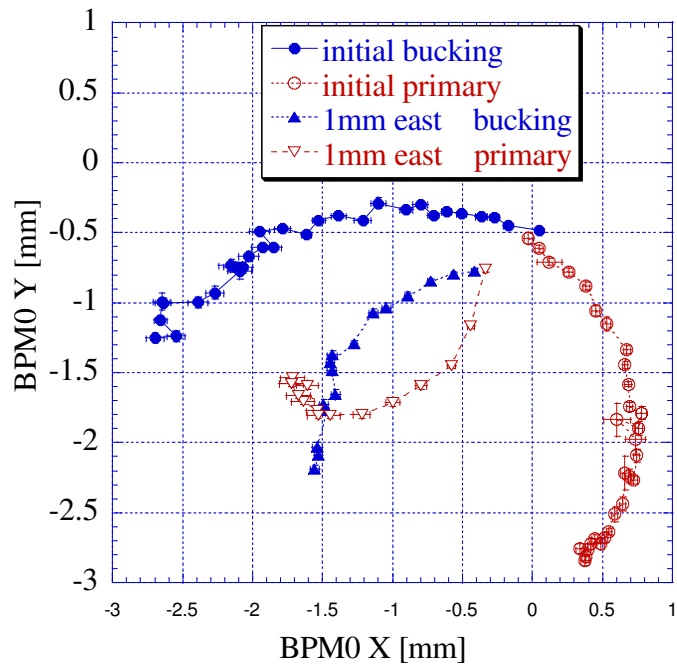
Figure 5.13: Before and after beam-based alignment: primary and bucking solenoid current scans.
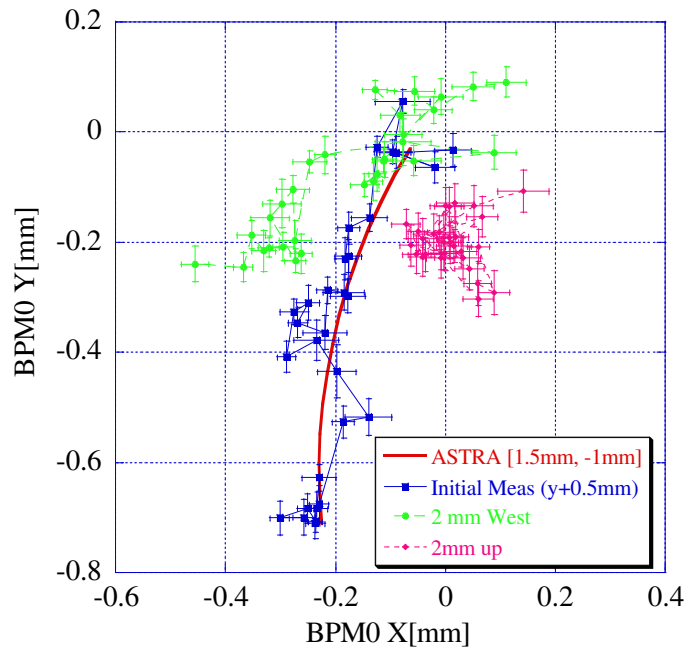
Figure 5.14: Beam position measured by BPM0 when the secondary solenoid current is scanned from 0 A to 290 A.
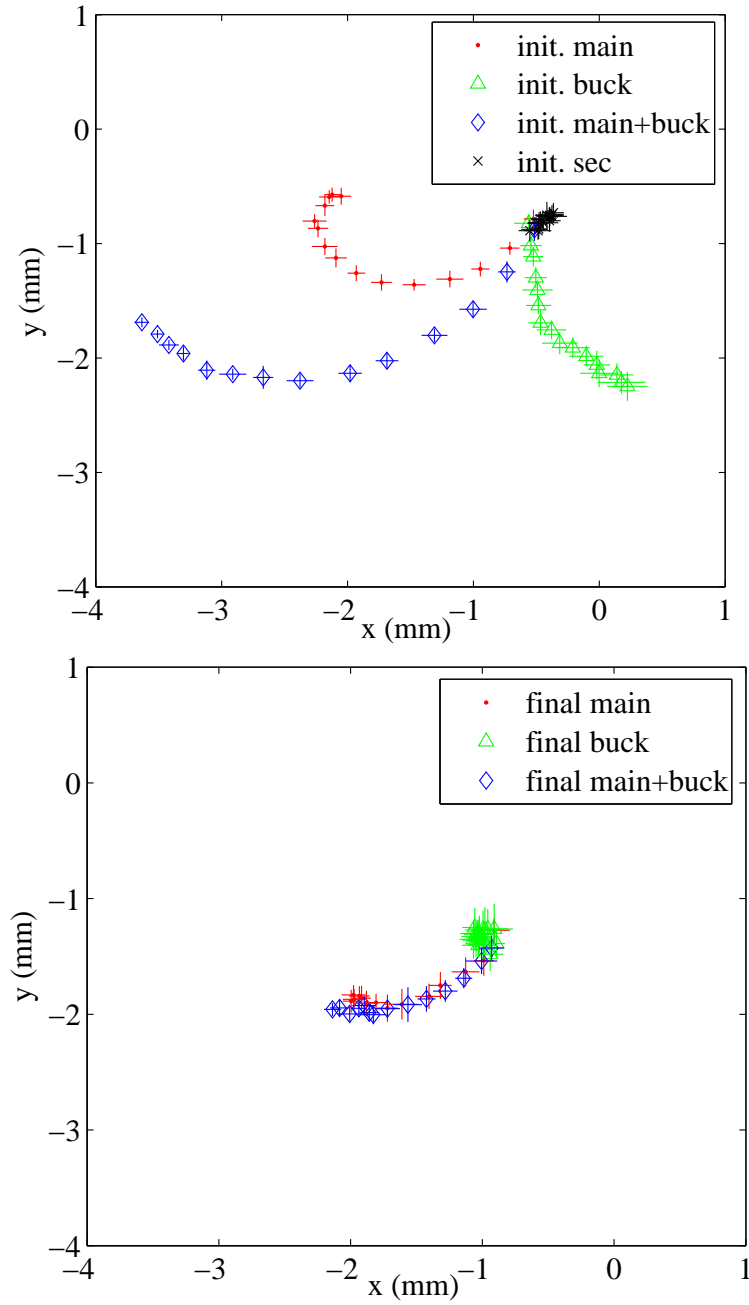
Figure 5.15: Beam position as measured by the BPM0 before and after beam-based-alignment.

5.3.3 Superconducting booster cavity

A TESLA-type superconducting 9-cell niobium cavity (see Figure 5.16) follows the rf gun [64]. The cavity operates at 1.3 GHz in TM_{010} π-mode, boosting the beam energy up to 16 MeV; hence, it is also referred to as the *booster cavity.* For a perfectly tuned cavity, the longitudinal accelerating electric field on the z-axis is shown in Figure 5.17.

Figure 5.16: The TESLA style 9-cell niobium cavity.
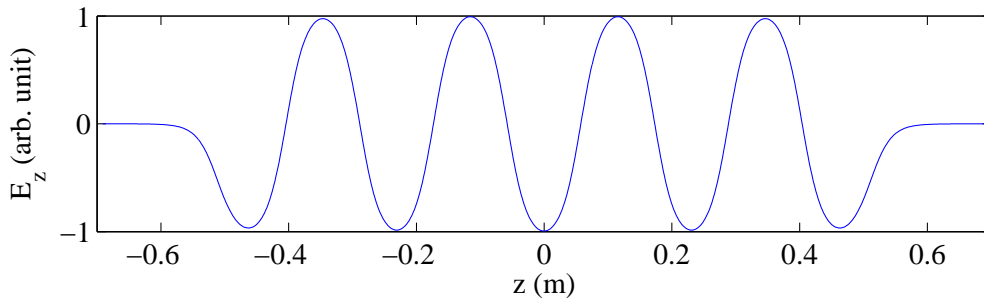
Figure 5.17: Longitudinal electric field on z-axis for the accelerating mode of the 9-cell cavity from MAFIA simulation.

Under nominal operating conditions, the booster cavity is at 1.8 K temperature and the average accelerating gradient is 12 MV/m. The energy gain from the booster cavity is about 12 MeV. The total beam energy of FNPL is thus around 16 MeV, as the beam energy from the rf gun is about 4 MeV. The beam energy is measured with a dipole spectrometer; see Section 5.4.2.

Apart from raising the beam energy, the booster cavity also has some influence on the transverse motions of the particles, such as focusing and/or deflecting. The effects in the transverse plane, to first order, can be expressed via the linear transfer matrix of the cavity. The measurement of the booster cavity transfer matrix is presented in Appendix D.

5.4   Beam diagnostics

Beam diagnostics comprise an essential part of a photoinjector facility. Various apparatuses are necessary for the measurements of different quantities such as transverse beam size, transverse position, bunch length, bunch charge, and beam energy etc. Next we will discuss the equipment needed for different beam parameter measurements.

5.4.1   Transverse beam diagnostics

Beam viewers and cameras

In order to measure transverse rms beam sizes, we need to image the beam density profile in the (x, y) plane. For this purpose, an optical transition radiation (OTR) or a fluorescence YAG-powder-based screen is used to view radiation at visible wavelengths generated as the electron beam strikes it. Such screens are also called beam *viewers*. The screen's normal axis makes a $45°$ angle with the beam propagation axis, and the radiation is centered around the specular axis which is perpendicular to the beam propagation axis. The screen is located inside a six-way cross (see Figure 5.18), allowing the radiation to be extracted from vacuum via an optical window mounted on one of the cross's ports. In our configuration, the radiation shines out along the horizontal axis. A $45°$ mirror reflects the radiation down toward the ground to an optical system consisting of a SONY digital charge-coupled device (CCD) camera (model XCD-X710) equipped with a PENTAX 50 mm lens [65]. The choice of the SONY camera was dictated by its dynamical range (up to 10 bits) and the pixel array size of 728×1024. The camera is mounted vertically below the beamline axis for

easier shielding in order to minimize the radiation damage to the CCD. Analytically we estimated a focal length of 50 mm should provide the proper magnification to demagnify the viewer circular area with axes $22.5 \times 22.5/\sqrt{2}$ mm^2 onto the CCD array of dimension 4.6080×3.4560 mm^2 (the array consists of 1024×768 pixels, each pixel being a square of 4.5 μm).
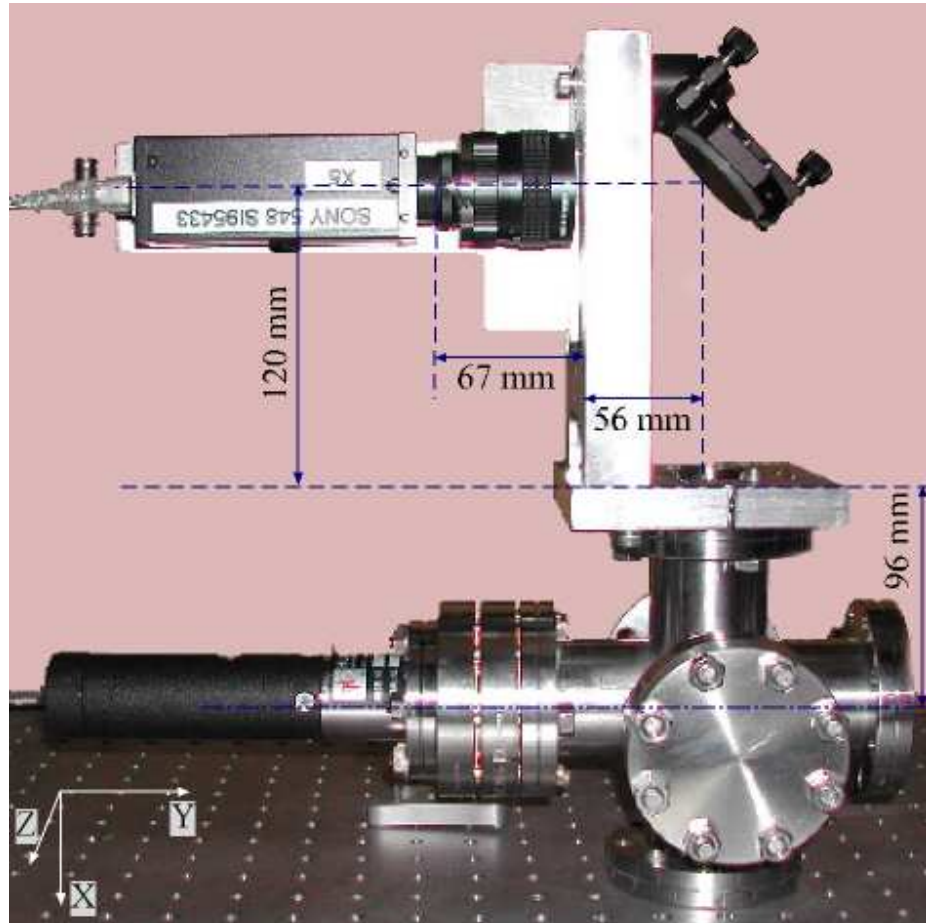
Figure 5.18: SONY digital camera setup for taking photos of beam density profile on viewers. Beam direction is coming out of the paper.

The imaging system was optimized by adjusting two parameters: (1) the spacing between the lens and the CCD array of the camera, and (2) the length between the lens and the OTR or YAG screen. A spacer of 9 mm was needed between the lens and camera mount. The optimized distances are indicated in Figure 5.18, and a corresponding image of the screen is shown in Figure 5.19. In the example shown
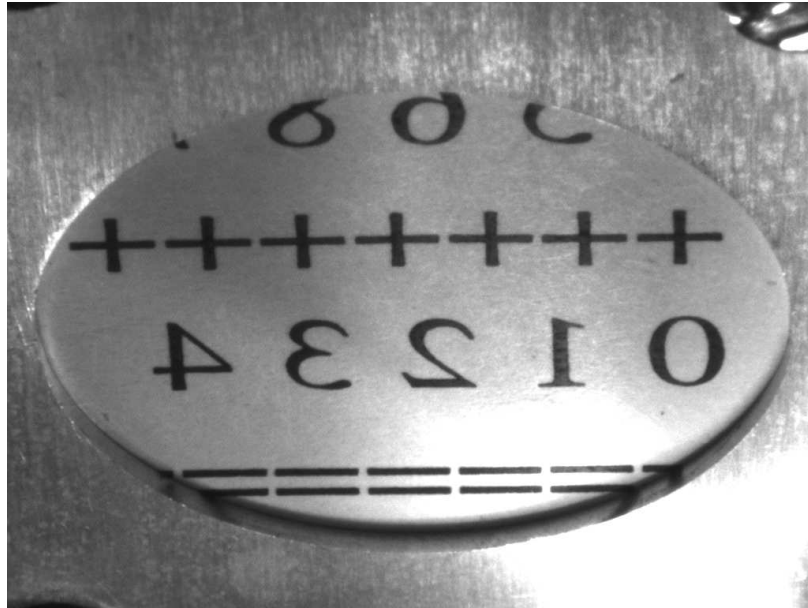
Figure 5.19: Example of calibration pattern. Horizontal and vertical axis for this picture correspond respectively to y and x directions in the accelerator.

here, the viewer calibrations are found to be 21μm/pixel and 23μm/pixel for the horizontal and vertical directions. The difference might be attributed to the screen tilt angle not being exactly $45°$ during our measurements.

Next we measured the resolution of the imaging system. We assumed the gain and shutter setting on the digital cameras do not significantly influence the resolution of the system (as long as the system is operated in the linear regime). Such an assumption was verified in an earlier test of the SONY CCD camera [66].

Given the optical setup, the system resolution will essentially depend on the manual iris aperture used in the lens system. Although the iris has the main purpose to provide a controllable attenuation of the OTR intensity reaching the CCD array, it also affects the resolution via depth-of-field and diffraction effects.

The diffraction effects for a cylindrically symmetric system limited by an aperture of diameter D is quantified by the Rayleigh criterion: two point-sources (radiating at wavelength λ) separated by an angle larger than $\delta\theta \simeq 1.22\lambda/D$ can be resolved by the optical system. If L is the distance between the object plane and the aperture, and δx the distance between the two point sources, we have the diffraction resolution

limit $\delta x \simeq 1.22\lambda/\psi$ where ψ is the angle subtended by the aperture: $\tan\psi = D/L$. The factor 1.22 in the previous equations comes from the fact the resolution is defined in terms of the Airy disk radius, i.e., the first zero of the function $J_1(\zeta)/\zeta$ ($1.22 \simeq 3.832/\pi$). In our case we are interested in the rms resolution, and we define it by replacing the factor 1.22 by 0.49 ($\simeq 1.553/\pi$) deduced from the calculation of the rms size of the Airy disk. We estimate the diffraction-limited rms resolution to be about $\sigma_{\rm dif} \simeq 0.49\lambda/\mathrm{atan}[f/(2FL)]$ where $F = f/D$ is the *F-number* of the system (f is the focal length and D the aperture diameter). Taking $\lambda = 440$ nm, $L = 300$ mm, and $f = 50$ mm we found $\sigma \in [0.34, 1.8]$ pixels for $F \in [2.6, 16]$. Hence a larger aperture gives better resolution if only diffraction is considered.

Contrary to diffraction effects, the depth of field calls for a small iris diameter. The depth of field effects results in a resolution limit of $\delta x \simeq 4F^2\lambda$.
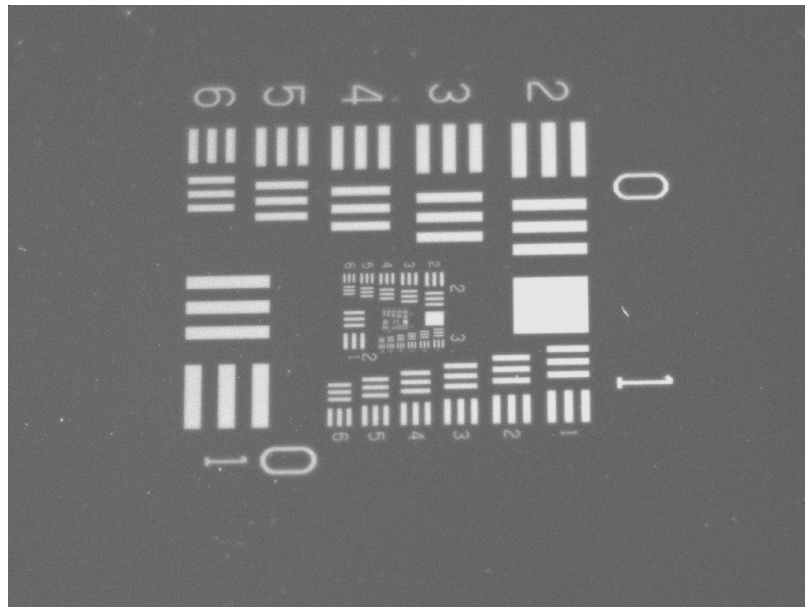
Figure 5.20: A photo of a USAF target taken by the SONY digital camera. For this image, the F-number of the lens is 8.

In principle the resolution measurement consists of measuring the modulation transfer function of the optical system for various modulation patterns. In practice

the resolution was measured using the so-called sharp edge technique. In signal processing theory, the resolution of a system is a measure of the system response to an impulse (δ-like signal). However, generating a δ-like point light source is not easy in practice. A common technique is to use a sharp edge instead. If we assume the system to be linear so that the input image signal $I(x, y)$ is mapped to an output image signal $O(x, y)$ via a relation of the form $I(x, y) \rightarrow O(x, y) = \sum_\lambda a_\lambda I(x, y)$, then upon differentiation with respect to, e.g., x, we also have a relation of the form $\partial_x I(x, y) \rightarrow \partial_x O(x, y) = \sum_\lambda a_\lambda \partial_x I(x, y)$. Thus measuring the system response to an input $\delta(x)$ is equivalent to measuring the response of the system to a sharp transition, a Heaviside-like function $H(x)$, since $\partial_x H(x) = \delta(x)$.

We used the patterns provided by a special target (the USAF 1951 target [67]), as pictured in Figure 5.20, to do such a measurement. Consider one vertical bar with width $2d$ along the horizontal axis; its normalized intensity distribution can be formulated as

$$\hat{I}(x, y) = H(x + d) - H(x - d), \tag{5.5}$$

where H is the Heaviside function ($H(\zeta) = 1$ for $\zeta > 0$ and $H(\zeta) = 0$ elsewhere). The derivative of $\hat{I}(x, y)$ with respect to x is then

$$\partial_x \hat{I}(x, y) = \delta(x + d) - \delta(x - d). \tag{5.6}$$

In a perfect optical system without resolution limit, the derivative of the output signal will be given by $\partial_x \hat{O}(x, y) \propto \partial_x \hat{I}(x, y)$. However, for a finite resolution system, the δ-function is widened. Replacing the δ-function by a Gaussian[2] in Eq. (5.6), we get for the output signal

$$\partial_x \hat{O}(x, y) \propto \left[\exp\left(-\frac{(x + d)^2}{2\sigma_x^2}\right) - \exp\left(-\frac{(x - d)^2}{2\sigma_x^2}\right) \right]. \tag{5.7}$$

---

2. This is motivated by the simple fact that a δ-function can be viewed as a Gaussian function with variance taken to zero.

Direct integration of Eq. (5.7) ($\int_{-\infty}^{x} d\xi \partial_x \hat{O}(\xi, y)$) yields

$$\hat{O}(x,y) = A \left[\mathrm{erf}\left(\frac{x+d}{\sqrt{2}\sigma_x} \right) - \mathrm{erf}\left(\frac{x-d}{\sqrt{2}\sigma_x} \right) \right].\tag{5.8}$$
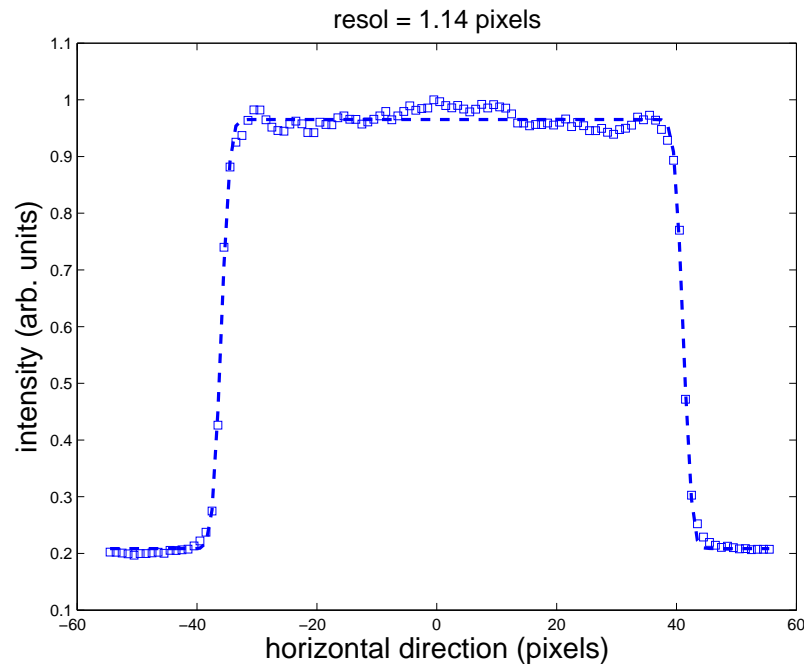
Figure 5.21: Example of resolution measurement by fitting the profile of a rectangular bar of the USAF target using Eq. (5.8).

From the USAF target, we can measure profiles associated with bars. This profile can then be fitted with Eq. (5.8), A, d, and σ_x being the fit parameters, to yield the resolution (σ_x) of the system. An example of such a fit on a bar profile is presented in Figure 5.21.

The system depicted in Figure 5.18 was used to measure the resolution. The camera was first focused on the screen (to yield an image similar to the one presented in Figure 5.19). The mirror was then removed and an USAF resolution target was put in front of the camera at a distance similar to the distance to the screen (the distance was adjusted to produce a well focused image of the target). An example of target image is shown in Figure 5.20. The target image was back illuminated using
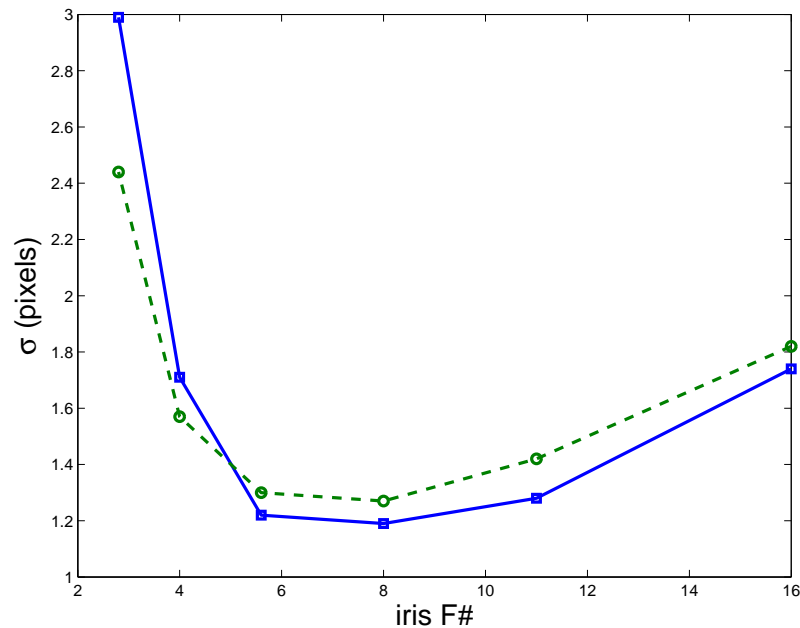
Figure 5.22: Measured resolution for vertical (squares) and horizontal (circles) directions versus iris F-number.

white light (we however expect chromatic effects in the optical system to be very small over the visible spectrum since the lenses are said to be optimized to reduce chromatic effects [68]).

Using the sharp-edge technique described, we measured the resolution of the system for various iris diameters (or F-numbers). The results are shown in Figure 5.22. For F-Numbers $F \in [5.6, 11]$, the resolution is about 1.3 times the pixel size in the object plane, that is $23 \times 1.3 \simeq 30$ μm. For larger F-numbers ($F \geq 11$), the resolution limit increases due to diffraction effects, whereas for smaller F-numbers ($F \leq 6$), it degrades due to depth-of-field effects.

It is interesting to estimate the amount of OTR radiation that is captured by the optical system as the F-number of the system is varied. If we estimate the half-angular acceptance of the system to be approximately $\theta \simeq \mathrm{atan}[f/(2FL)]$ and assume the system to be centered on the radiation source emission axis, then the fraction of

radiated intensity within a cone of half-angle θ is (see also [69]):

$$R(\theta) = \frac{\int_0^\theta \frac{\sin^3 \vartheta}{(1-\beta^2 \cos^2 \vartheta)^2} d\vartheta}{\int_0^{\pi/2} \frac{\sin^3 \vartheta}{(1-\beta^2 \cos^2 \vartheta)^2} d\vartheta} \tag{5.9}$$

The function $R(\theta)$ is plotted in Figure 5.23, where we compare the expected normal-
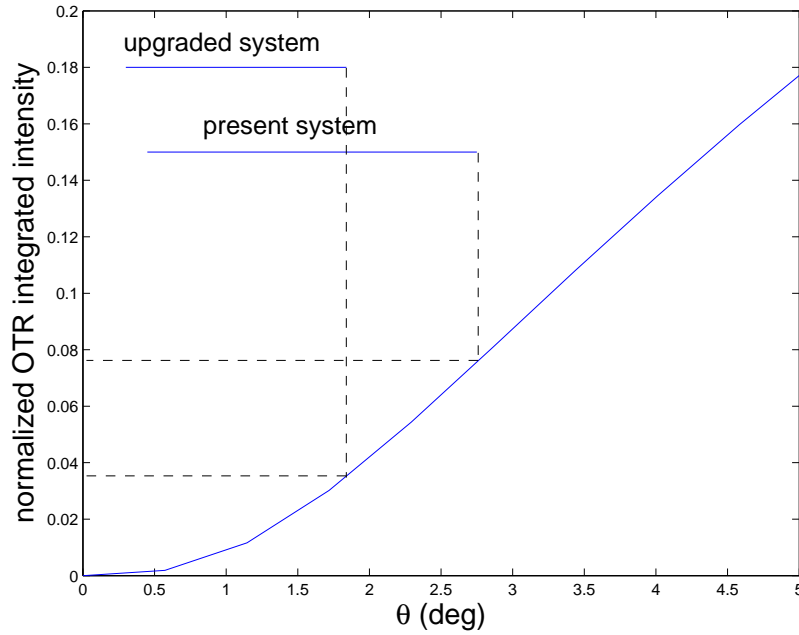
Figure 5.23: Normalized OTR intensity versus half-angle acceptance of the optical system. The normalization is done with respect to the total intensity emitted within a half-angle acceptance of $90°$.

ized OTR intensity for the upgraded system with respect to the present system. Since the lens is located at 300 mm from the screen in the upgraded system (compared to 100 mm in the present case), the intensity will drop by a factor of approximately 2. Extra focusing lenses might be needed in order to focus the beam on the CCD to detect the OTR signal with a good signal-to-noise ratio.

Slits

Aside from the screens, there are several locations in the beamline where horizontal or vertical, single-slit or multislit tungsten plates can be inserted for emittance and angular momentum measurement. More details will be discussed in Section 6.4.1.

Beam position monitors

While one can measure the beam location using the OTR or YAG screens, there are other means to measure the beam centroid locations as well. We have eight button-type electromagnetic beam position monitors (BPMs) distributed along the beam-line[3]. Each BPM has four button-type electrodes with a diameter around 11 mm, distributed evenly inside the round beam pipe on the top, bottom, left and right. When the electron beam passes though the BPM at an offset with respect to the center of the beam pipe, it induces different signals on each electrode. The beam's transverse offset can be inferred from the difference of the signals from the four electrodes [70]. The systematic error of the FNPL BPM system is around 100 μm.

---

3. The electronics of the FNPL BPM system was provided by DESY, Hamburg. We thank R. Neumann and M. Wendt from DESY, and P. Prieto from Fermilab for making the system functional.

5.4.2   Longitudinal beam diagnostics

Streak camera

At FNPL, the durations of the UV laser pulse and the electron beam are both on a pico-second scale and can be measured using a streak camera. While the UV light can be aligned to the streak camera directly, the electron bunches need to generate light first by hitting an OTR screen. The OTR light is then transported into the streak camera. The principle [71, 72] of a streak camera is shown in Figure 5.24.
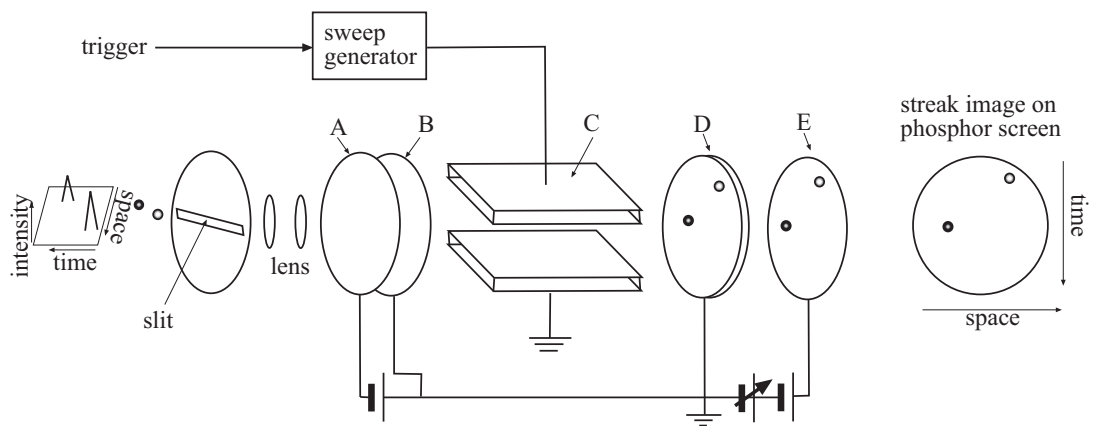
Figure 5.24: Operating principle of streak camera. A: photocathode; B: accelerating electrode; C: sweep electrode; D: micro-channel plate; E: phosphor screen.

The light pulses to be measured are projected onto the slit and focused by the lens to the photocathode of the streak tube. Consider two light pulses with slightly different temporal and spatial position, each with a different light intensity. Two electron pulses, with intensity proportional to the light intensity of the corresponding light pulse, are generated from the photocathode of the streak tube when the light pulses hit it. These electrons are accelerated toward the phosphor screen direction by the accelerating electrode. On their path to the phosphor screen, the electrons are deflected between a pair of sweep electrodes where a high-speed sweep voltage is applied. The deflection magnitude is proportional to the arrival time at the streak tube, with the earlier arrival pulse at the top space in the vertical direction. The deflected electrons are then conducted to a micro-channel plate (MCP), and they are

amplified by thousands of times, and then converted back into light when they bombard a phosphor screen. Finally light emitted from the phosphor screen is registered by a CCD camera. So on a streak camera photo, the time axis flows from top to bottom (top being earlier in time), and the horizontal direction corresponds to the positions of the incident light in horizontal direction in space.

The streak camera of FNPL is a Hamamatsu C5680-21S with M5676 fast sweep module. A Pulnix progressive scan CCD camera captures the light from the phosphor screen, and the rms bunch length can be calculated from the image profile along the vertical axis, i.e., the time axis; see Figure 5.25. A calibration of 3.6 pixel/ps is used for the FNPL streak camera at the fastest sweep speed [53].
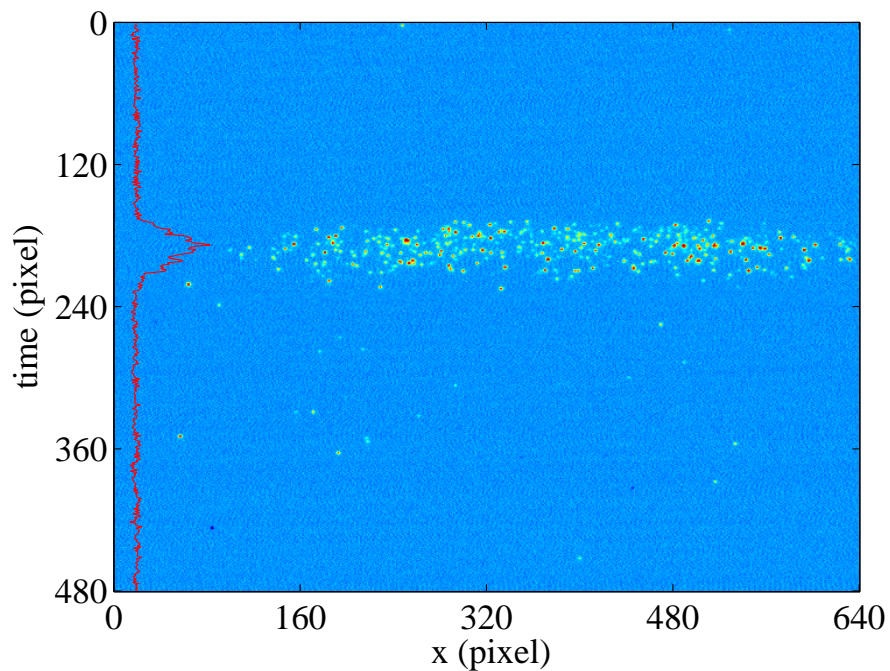
Figure 5.25: A photo taken by the streak camera for electron bunch length measurement in the time domain. The solid line is the projection of the image on the time axis.

Spectrometer

A dipole magnet which bends the beam by 45° in the horizontal plane serves as the FNPL spectrometer at the end of the beamline. Assuming the trajectory of the beam as it enters the spectrometer is normal to the magnet pole face, then the current needed to bend the beam by 45° is related to the longitudinal beam momentum p_z via

$$p_z(\text{MeV/c}) = 1.619\, I(\text{A}), \tag{5.10}$$

where I is the spectrometer current. The constant in Eq. (5.10) is obtained from the most recent spectrometer and booster cavity rf calibration, detailed in [73, 74].

We center the beam on two screens separated by a drift space upstream of the spectrometer to make sure that it enters the spectrometer normal to the pole face, and adjust the spectrometer current such that the beam is centered on the screen at the exit of the spectrometer, which is aligned to have an angle of 45° with respect to the beamline prior to the spectrometer.

While the beam enters the FNPL spectrometer normal to the pole face, it exits at an angle of 22.5° with respect to the normal of the pole surface. The dispersion function at a drift L downstream from the exit of the spectrometer is [75]

$$\eta = (\rho_0 + L\tan\delta)(1 - \cos\theta) + L\sin\theta, \tag{5.11}$$

where $\rho_0 \approx 370$ mm is the bending radius of the spectrometer, $\theta = 45°$ the dipole bending angle, and $\delta = 22.5°$ is the angle between the beam direction and the normal of the pole face at the dipole exit. For example, at the viewer downstream of the spectrometer where L is about 253 mm, we have the dispersion $\eta \approx 318$ mm from Eq. (5.11).

5.4.3   Bunch charge measurement

The electron bunch charge can be measured either destructively by using a Faraday cup, or nondestructively by using an integrating current transformer (ICT).

The ICT used at FNPL is a standard commercial product [76], consisting of a

toroid which is placed outside the vacuum pipe. When an electron bunch passes through the toroid, it induces a signal in the toroid. The integral of the induced signal over time is proportional to the bunch charge of the electron. The image charge induced by the electron bunch is diverted outside the toroid by means of a copper tape; see Figure 5.26.
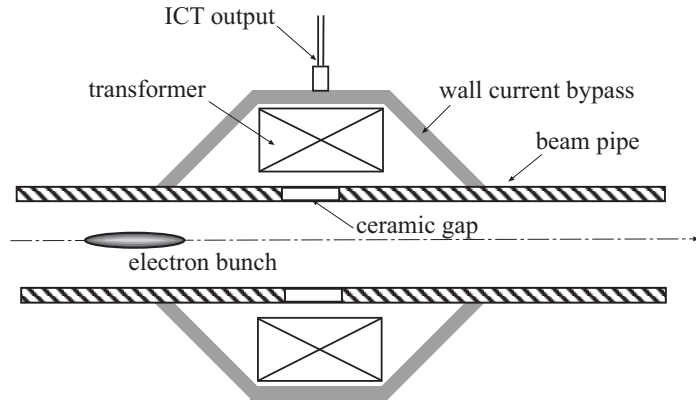
Figure 5.26: Sectional view of an ICT installed in the beamline.

The calibration of the ICT was detailed in Ref. [77]. Given the output signal $V(t)$, the bunch charge is given by

$$Q = \mathcal{C} \int V(t) \mathrm{d}t, \quad \text{where} \quad \mathcal{C} = 0.8 \, \frac{\mathrm{C}}{\mathrm{V} \cdot \mathrm{s}} \,. \tag{5.12}$$

CHAPTER 6
EXPERIMENTS AND NUMERICAL SIMULATIONS

6.1 Introduction

For the experiment of angular-momentum-dominated and flat electron beams, key elements in the beamline include the solenoids, rf cavities and skew quadrupoles, as shown in Figure 6.1. The average canonical angular momentum of the electrons born at the photocathode is proportional to the magnetic field on the cathode provided by the solenoids. At the gun exit, the beam kinetic energy could be up to 4 MeV; the booster cavity raises the kinetic energy up to $16 - 17$ MeV; see Figure 6.2. The round-to-flat beam transformer composed of three skew quadrupoles is located downstream of the booster cavity (three of the four skew quadrupoles shown in Figure 6.1 are used.). A proof-of-principle flat beam generation experiment was reported in References [27] and [28]. Our goal here is to understand each step of the round-to-flat beam transformation and improve the flat-beam emittance ratio.
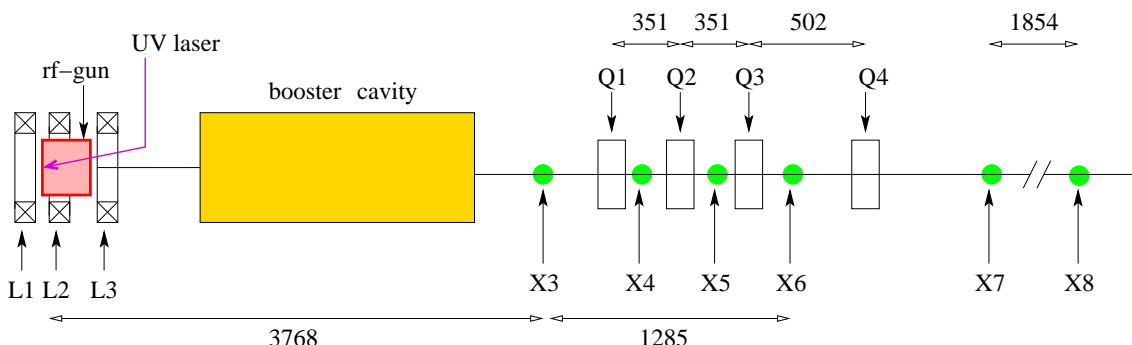
Figure 6.1: Overview of the FNPL beamline. Here only the elements pertaining to the flat-beam experiment are shown. The letters represents solenoidal magnetic lenses (L), skew quadrupoles (Q), and diagnostic stations (X, which means "cross"). Dimensions are in mm.

The diagnostics for the measurements of angular momentum and emittances include OTR or YAG viewers, multislit or single-slit tungsten plates, and CCD cameras. For example, to measure the canonical angular momentum of the electron beam, OTR viewers at X3, X6 and a multislit plate at X3 are used; to measure the flat-beam emit-
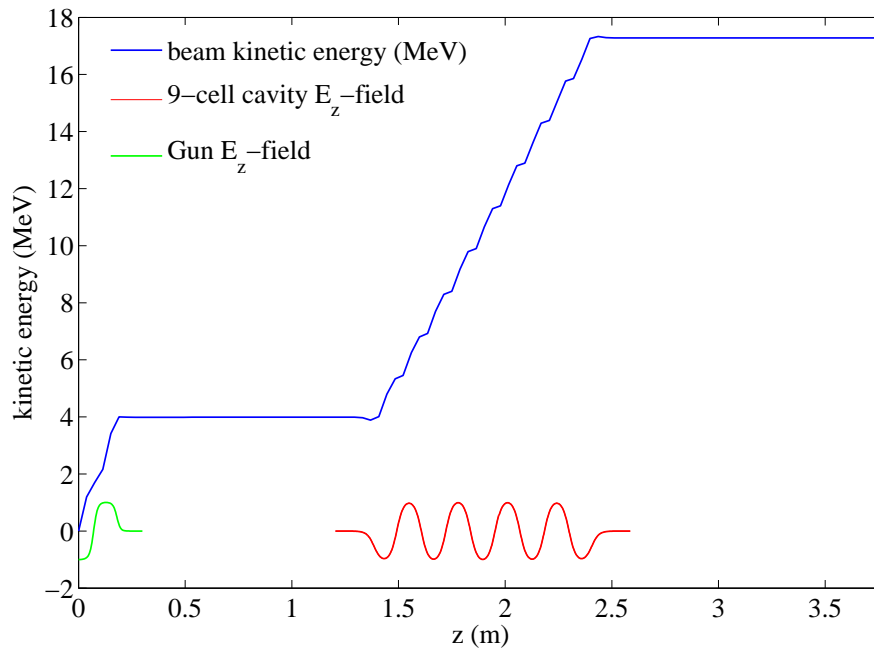
Figure 6.2: An example of beam kinetic energy along z-axis with the schematic drawing of the rf gun and 9-cell booster cavity accelerating field E_z.

tances, the OTR viewer at X7, the YAG viewer at X8, and single horizontal/vertical plates at X7 are used.

We start with the angular momentum measurements of an angular-momentum-dominated beam, then follow with the flat-beam generation and emittance measurements.

6.2 Angular momentum measurements

6.2.1 Experimental method

Due to the cylindrical symmetry of the system (UV drive-laser light, external electromagnetic fields), the canonical angular momentum of each electron is conserved. In an axial magnetic field $B_z(z)$, the canonical angular momentum of an electron, L,

in circular cylindrical coordinates (r, ϕ, z) is [19]

$$L = \gamma m r^2 \dot{\phi} + \frac{1}{2} e B_z(z) r^2, \tag{6.1}$$

where γ is the Lorentz factor, $\dot{\phi}$ the time derivative of ϕ, m and e are respectively the electron rest mass and charge.

The average canonical angular momentum of the electrons, $\langle L \rangle$, is obtained by averaging Eq. (6.1) over the beam distribution. At the photocathode location, we have $\langle \dot{\phi} \rangle = 0$ and

$$\langle L \rangle = \frac{1}{2} e B_0 \langle r^2 \rangle = e B_0 \sigma_c^2, \tag{6.2}$$

where $B_0 = B_z(z = 0)$ is the axial magnetic field on the photocathode, and σ_c is the transverse rms beam size on the photocathode in cartesian coordinates. For a cylindrically symmetric beam, $\sigma_c^2 = \langle r^2 \rangle / 2$.

The canonical angular momentum at the photocathode surface is obtained from Eq. (6.2). Given the experimental settings of the solenoidal lens currents, the magnetic field, B_0, is inferred via simulations using the POISSON [80] program, which is benchmarked against calibration of the solenoidal lenses [52]. The value of σ_c used in Eq. (6.2) is directly measured from an image of the UV laser beam on a "virtual photocathode". The virtual photocathode is a calibrated UV-sensitive screen located outside of the vacuum chamber, being a one-to-one optical image of the photocathode.

Outside the solenoidal field region, where B_z vanishes, an electron acquires axial mechanical angular momentum due to the torque exerted on it in the transition region. Since $B_z(z) = 0$, the second term of Eq. (6.1) vanishes and the canonical angular momentum is given by the first term of Eq. (6.1), which is the axial mechanical angular momentum.

To measure the mechanical angular momentum, let's consider an electron, in a magnetic field-free region, at longitudinal location z_1 with transverse radial vector $\vec{r}_1 = r_1 \vec{e}_x$. After propagating through a drift space, the electron reaches $\vec{r}_2$ at location z_2. Let $\theta = \angle(\vec{r}_1, \vec{r}_2)$ be the angle between the two radial vectors $\vec{r}_1$ and $\vec{r}_2$ (hereafter referred to as the "shearing angle"). It can be experimentally measured by inserting

at location z_1 a multislit mask and measuring the corresponding shearing angle of the beamlets at the location z_2; an illustration of the measurement technique is shown in Figure 6.3. A couple of experimental photographs are presented in Figure 6.4.
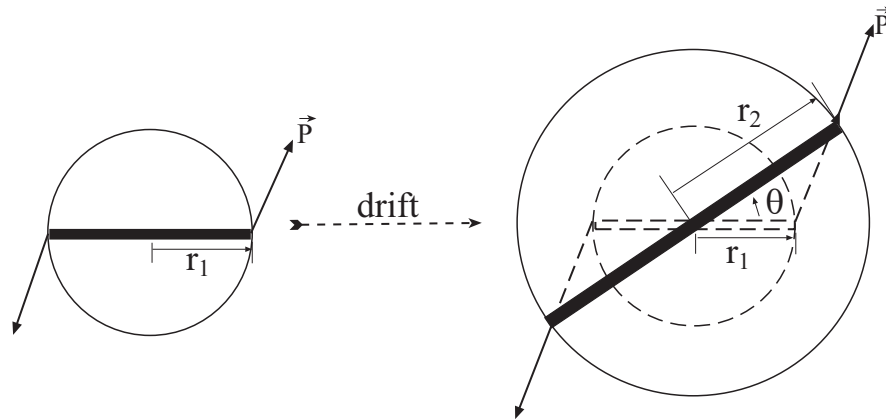
Figure 6.3: Beam with canonical angular momentum induced sheers in a drift. The dark narrow rectangular can be a slit inserted into the beamline in order to measure the shearing angle.

The mechanical angular momentum of the electron, $\vec{L}$, is given by:

$$\vec{L} = r_1 \vec{e}_x \times \vec{P} = r_1 P_y \vec{e}_x \times \vec{e}_y. \tag{6.3}$$

Let $y' = \frac{\mathrm{d}y}{\mathrm{d}z} = \frac{p_y}{p_z}$, where p_y and p_z are the vertical and longitudinal components of the momentum; y' is a constant in a drift space for an angular-momentum-dominated beam. The change in y coordinate, Δy, can be calculated via

$$\Delta y = \int_0^D y' \mathrm{d}z = y' D.$$

On the other hand, from Figure 6.3, we have $\Delta y = r_2 \sin\theta$, hence $y' = r_2 \sin\theta / D$ and Eq. (6.3) can be re-written in the following form:

$$\vec{L} = r_1 p_z y' \vec{e}_z = p_z \frac{r_1 r_2 \sin\theta}{D} \vec{e}_z. \tag{6.4}$$

Let the rms beam radii be σ_1^r and σ_2^r at z_1 and z_2, respectively. For a laminar
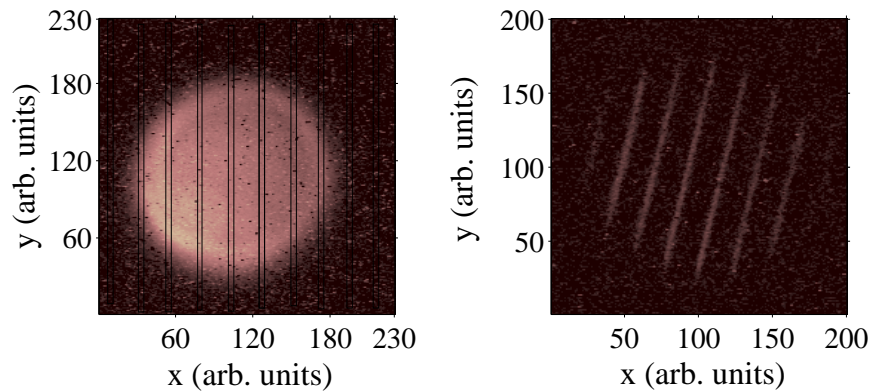
Figure 6.4: Images used for mechanical angular momentum measurement. Beam transverse density on X3 (left), and beamlets on X6 when the vertical multislit mask is inserted at X3 (right). The vertical lines superimposed on the X3 image is an illustration of vertical slits when the multislit mask is inserted.

beam, the canonical angular momentum averaged over the beam distribution can then be calculated via:

$$\langle L \rangle = p_z \frac{\sigma_1^r \sigma_2^r \sin \theta}{D}. \tag{6.5}$$

Finally, for a cylindrically symmetric beam, the rms beam size on the horizontal and vertical axes, σ_x and σ_y, are related to the rms beam radius by: $\sigma_x = \sigma_y = \sigma_r/\sqrt{2}$. Thus Eq. (6.5) can be written as:

$$\langle L \rangle = 2p_z \frac{\sigma_1 \sigma_2 \sin \theta}{D}, \tag{6.6}$$

where $\sigma_1 = \sigma_{x1} = \sigma_{y1}$, $\sigma_2 = \sigma_{x2} = \sigma_{y2}$.

So measurements of rms beam sizes at location z_1 and z_2 along with the corresponding shearing angle, as the beam propagates from z_1 to z_2, provide the required information for calculating the beam mechanical angular momentum.

Eq. (6.2) and Eq. (6.6) are the major results of this subsection [78]. In the following several subsections we will use these two equations to measure the average angular momentum of the electron beam and compare it with the simulation results as well as theoretical expectations.

6.2.2 Dependence on the magnetic field on the photocathode

The magnetic field on the cathode can be varied by properly adjusting the solenoid currents; see Table 6.1. The bucking solenoid current is set to zero. The column "POISSON" are simulation results by putting the solenoid currents directly into the simulation, while the "linear combination" column are results from the following linear equation: $B_z[\text{Gauss}] = 774.54 \times \frac{I_p[\text{A}]}{170} + 9.38 \times \frac{I_s[\text{A}]}{70}$, where I_p and I_s are the primary and secondary solenoid current, respectively. The constants in the linear equation are obtained from POISSON simulations. The laser transverse spot size on the cathode was held constant and measured to be $\sigma_x \simeq \sigma_y \simeq 0.97 \pm 0.04$ mm. This measurement together with the estimated value of the longitudinal magnetic field on the photocathode can be plugged in Eq. (6.2) to yield the canonical angular momentum.

Table 6.1: Axial magnetic field on the photocathode at different primary and secondary solenoid current settings.

solenoid current [A]		magnetic field on cathode [Gauss]	
primary	secondary	POISSON	linear combination
40	295	229	222
60	295	325	313
80	195	421	404
100	295	517	495
120	295	613	586
140	255	702	672
160	255	794	763
180	220	877	850
200	180	959	935
220	80	1031	1013
240	0	1105	1094

The mechanical angular momentum downstream of the TESLA cavity can be measured at X3 and X6 (see Figure 6.1). At X3 ($z_1 = 3.678$ m), either an OTR screen (for beam spot size measurements), or a multislit mask (for shearing angle measurement) can be inserted. After a drift of distance 1.375 m, another OTR viewer is available at X6 ($z_1 = 5.053$ m). The measurement consists of the following sequence:

(1) measure the beam rms size at location z_1 and z_2, and (2) insert the vertical multislit mask at location z_1 and measure the shearing angle from the slit images at location z_2. An example of the measurement sequence is depicted in Figure 6.5. The measurements of the rms beam sizes at z_1 and z_2 along with the corresponding
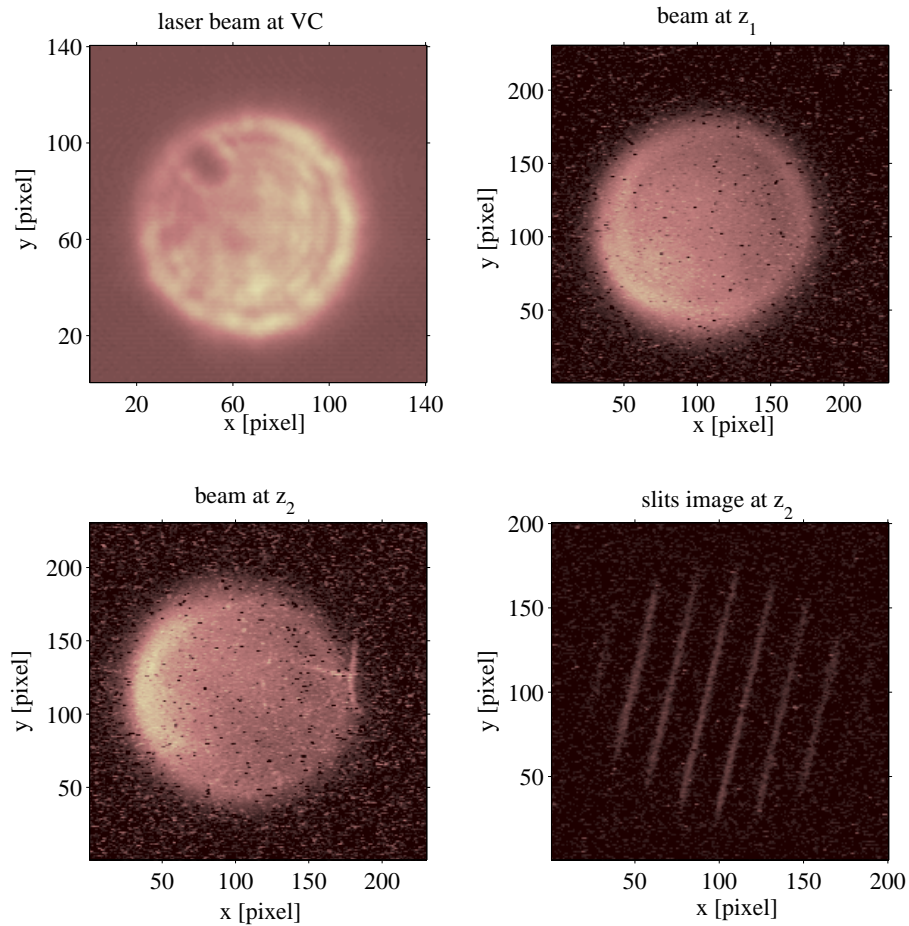
Figure 6.5: Example of an experimental measurement sequence needed to calculate the canonical angular momentum at the photocathode (top-left, virtual cathode photo) and mechanical angular momentum downstream of the TESLA cavity.

shearing angle θ are summarized in Figure 6.6.

The computer program ASTRA is used to simulate the beam dynamics using the experimental conditions of the drive laser, rf-field amplitudes and phases, etc. First, we compare in Figure 6.7 the canonical angular momentum of the beam at the photocathode (computed as $\sum_{i=1}^{N_{\text{mac}}} \frac{1}{2} e B r_i^2$ where the sum is performed over the

macroparticles used in the simulation, and N_{mac} is the number of macroparticles) with the mechanical angular momentum downstream of the TESLA cavity (computed as $\sum_{i=1}^{N_{\mathrm{mac}}} \frac{1}{p_{z,i}}(x_i p_{y,i} - y_i p_{x,i})$). The agreement is excellent.

Second, the simulations of the measurement technique for the various solenoid settings considered in the experiment are summarized in Figure 6.8 (this Figure should be compared with Figure 6.6). The beam spot sizes at z_1 and z_2 were directly evaluated after tracking the beam with ASTRA. A multislit mask samples the phase space produced by ASTRA at z_1, and the so-generated beamlets at z_1 were tracked up to z_2 using linear transport matrix. The linear transport matrix is checked against ASTRA simulation by comparing the beam sizes at z_2 produced from either method.

Finally, in Figure 6.9 we compare the measured mechanical angular momentum with the canonical angular momentum calculated from the magnetic field on the cathode from Eq. (6.2). A weighted least-squares linear fit is performed and the slope is found to be 0.98±0.03; see the blue solid line in Figure 6.9. The measured mechanical angular momentum agrees well with the measured canonical angular momentum on the photocathode, which confirms the fact that canonical angular momentum on the photocathode is converted into mechanical angular momentum in a magnetic-field-free region.

For each measurement point presented in Figure 6.9, we compare the strengths of the space charge, emittance, and angular momentum terms in the envelope equation [see Eq. (2.1)]. The evaluations are performed at location z_1 and z_2, as shown in Figure 6.10 (a) and (b), respectively. We see that the angular momentum term indeed dominates the other two terms, with the exception of the point at lowest magnetic field on the cathode, where the angular momentum is the smallest.
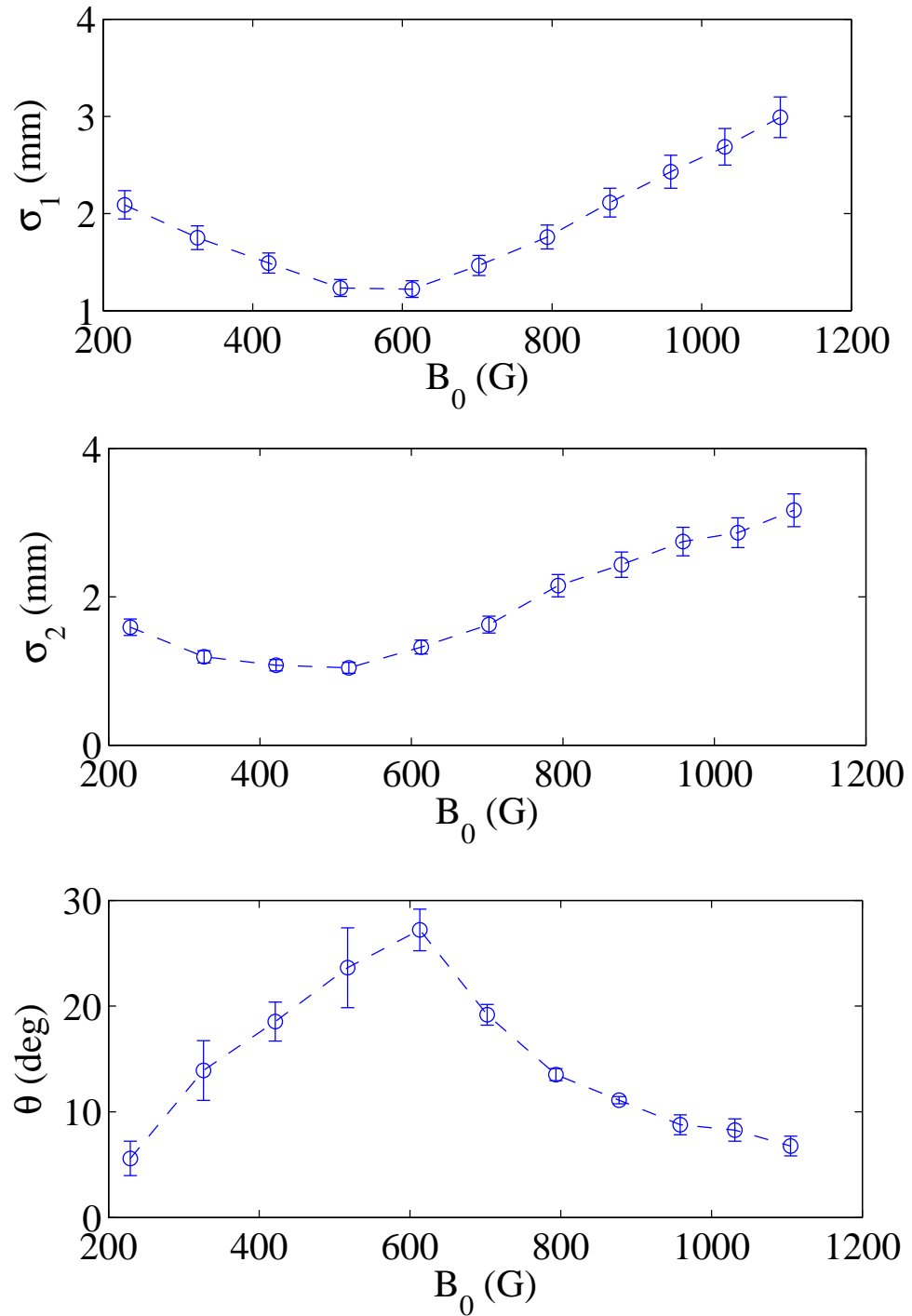
Figure 6.6: Measured rms beam sizes at locations z_1 and z_2 (top two plots), rotation angle at z_2 from slits inserted at z_1 (bottom plot).
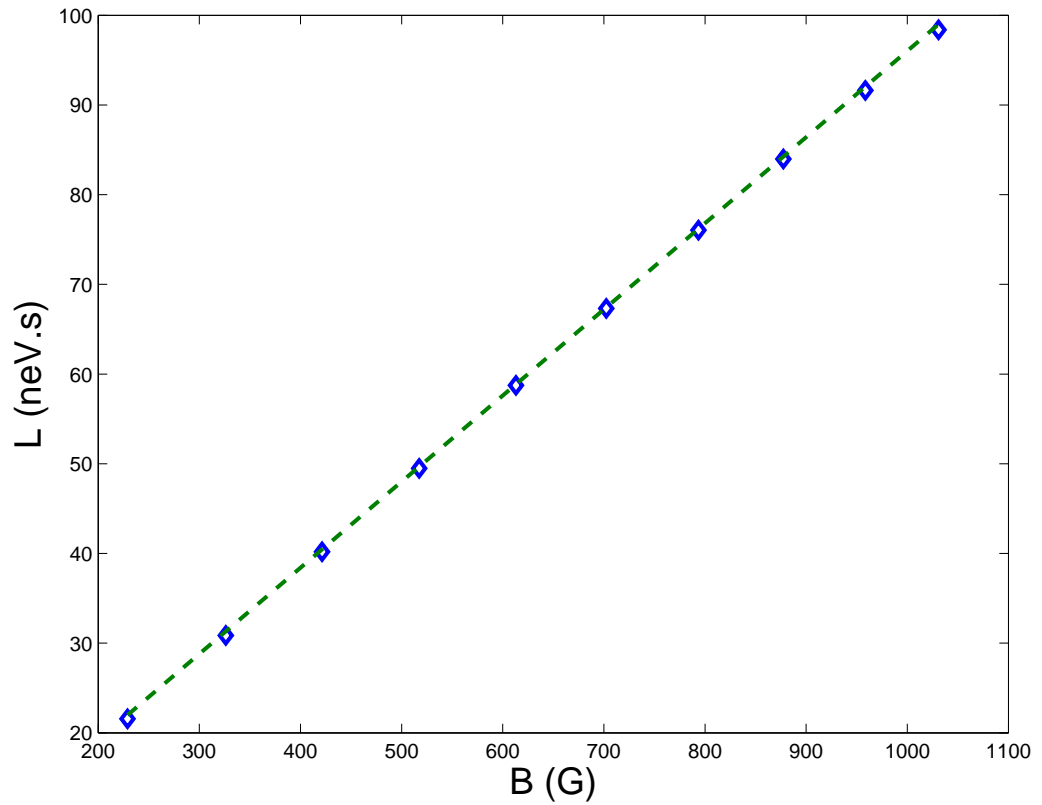
Figure 6.7: Comparison of the canonical angular momentum computed at the photo-cathode with mechanical angular momentum calculated downstream of the TESLA cavity. The tracking from the photocathode to downstream of the TESLA cavity has been performed using ASTRA with space charge included.
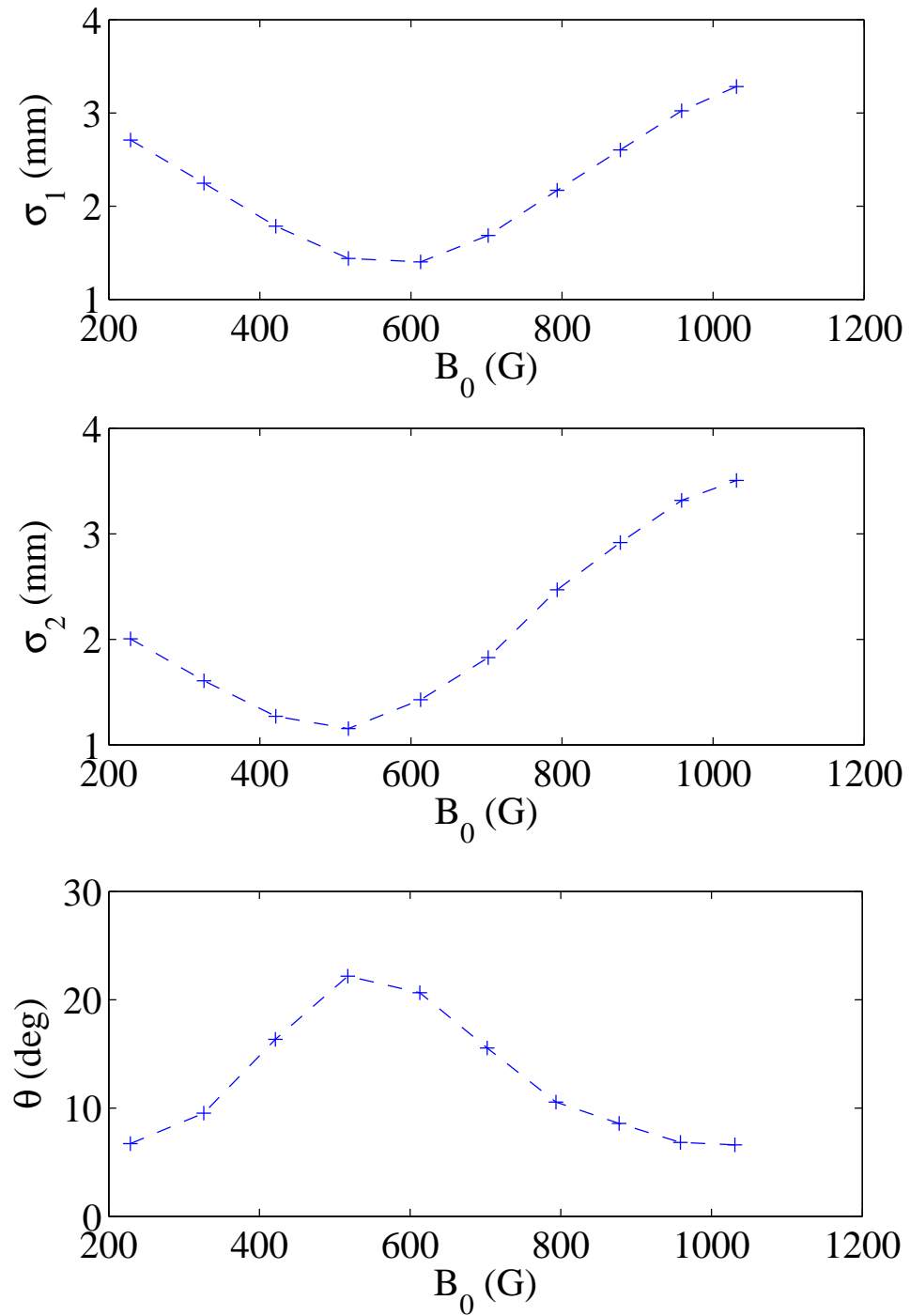
Figure 6.8: Simulation of the experiment: rms beam sizes at locations z_1 and z_2 (top two plots), rotation angle at z_2 from slits inserted at z_1 (bottom plot).
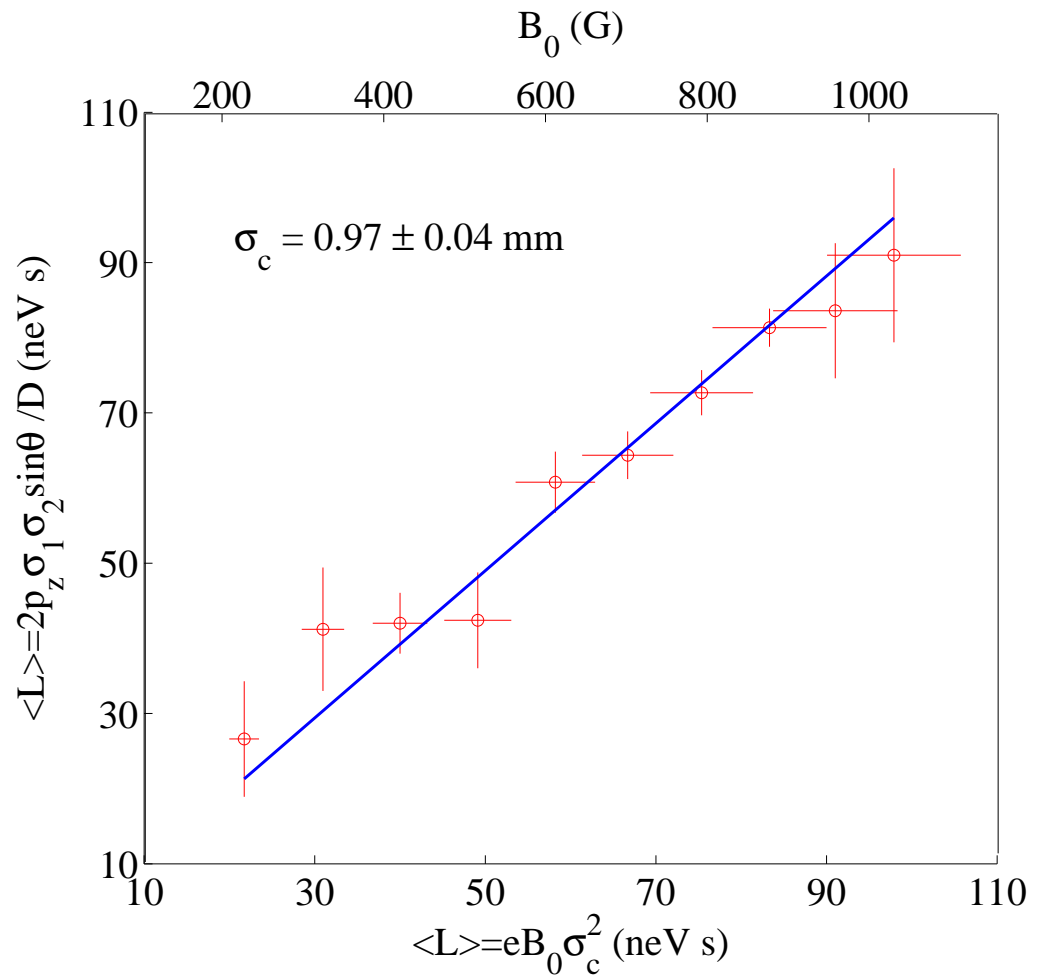
Figure 6.9: Experimental measurements (circles) of mechanical angular momentum from Eq. (6.6) versus the canonical angular momentum from Eq. (6.2). The solid line is a linear fit.
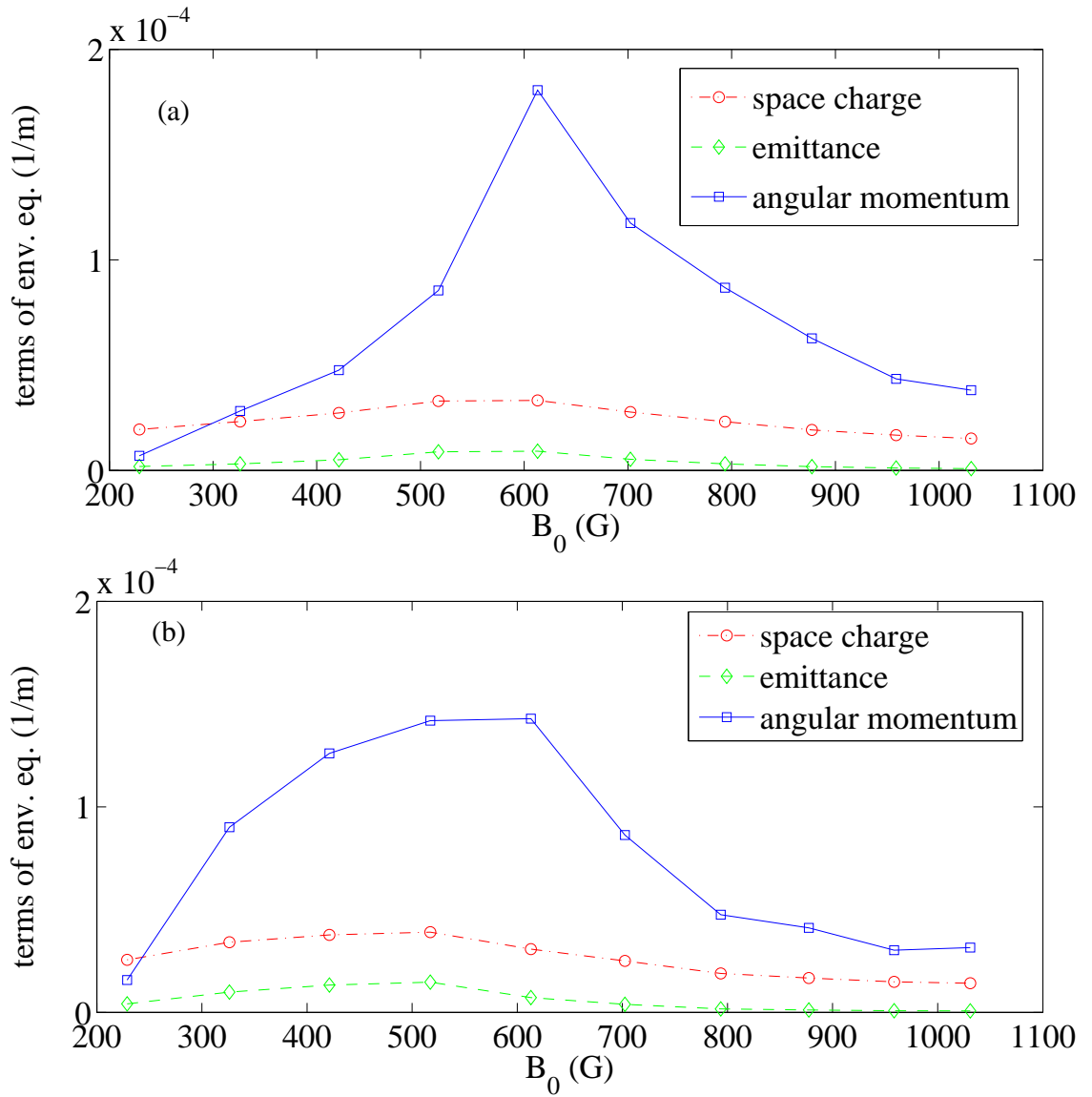
Figure 6.10: Comparison of the values of the space-charge, emittance and angular momentum terms in the envelope equation.

6.2.3   Dependence on bunch charge

To study space charge effects on angular momentum, we vary the bunch charge while keeping the magnetic field and beam spot size on the cathode constant. This is achieved by adjusting the drive-laser intensity via a "volume knob" which is composed of a half-wave plate and a cubic polarizer.
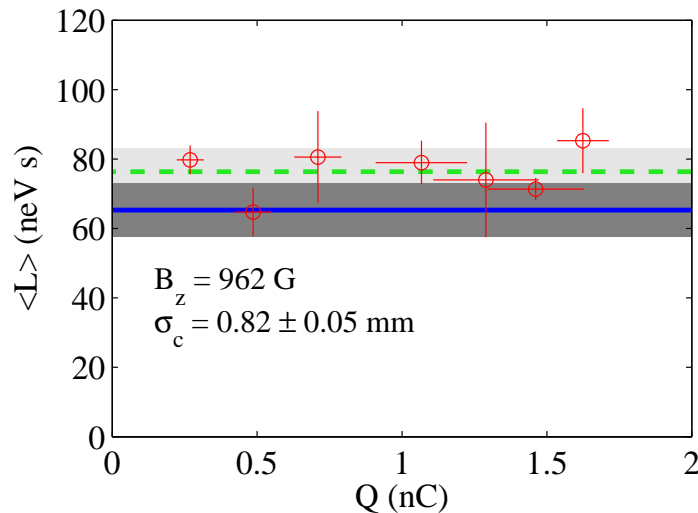
Figure 6.11: Angular momentum versus bunch charge. The experimental data (circles) are compared with theoretical values of the canonical angular momentum calculated from Eq. (6.2). The dashed line represents the average value of all the data points, and the shaded areas cover the uncertainties in the measurements either from Eq. (6.2) (darker strip) or from Eq. (6.6) (lighter strip).

For the measurements shown in Figure 6.11 the bunch charge is varied from 0.2 nC to 1.6 nC. Within the experimental error (10% relative spread), the measured mechanical angular momentum stays constant, and we conclude that the beam is indeed angular-momentum-dominated within the region explored.

6.2.4   Dependence on drive-laser spot size

The value of angular momentum has a quadratic dependence on the beam size on the photocathode, as displayed by Eq. (6.2). To explore this dependence, the angular momentum is measured for different drive-laser spot sizes on the photocathode. A

remotely controllable iris is used to control the drive-laser spot size on the cathode. The magnetic field on the photocathode is kept constant. The measured angular momenta are then plotted against the theoretical values as expected from Eq. (6.2); see Figure 6.12. Again, there is good agreement.
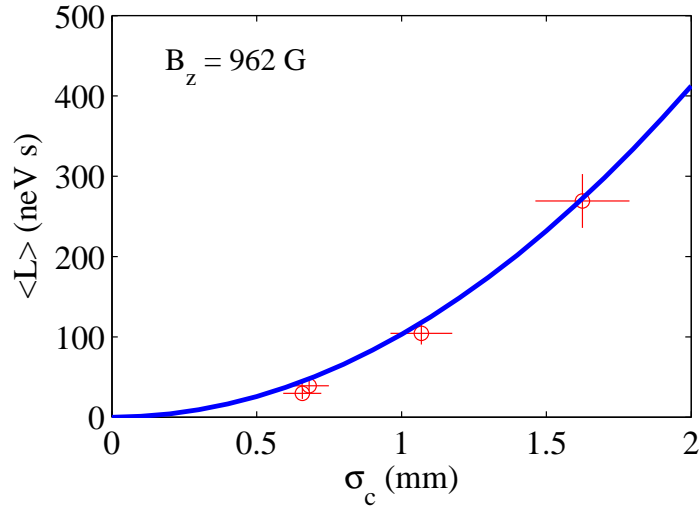
Figure 6.12: Angular momentum versus photocathode drive-laser spot size. The experimental data (circles) are compared with theoretical values of the canonical angular momentum from Eq. (6.2).

6.2.5 Propagation of the angular momentum along the beamline

In principle, angular momentum is conserved along the beamline. We investigate the conservation of angular momentum by measuring the mechanical angular momentum at different locations downstream. The results are shown in Figure 6.13. Notice that at $z = 0$, the canonical angular momentum is calculated from Eq. (6.2) while downstream of the cathode where B vanishes, we used Eq. (6.6), as explained in Section 6.2.1.
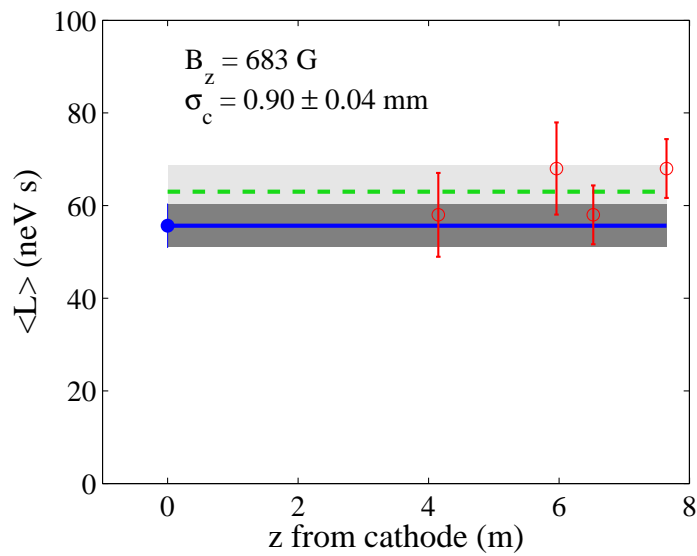
Figure 6.13: Evolution of canonical angular momentum along the beamline. At the photocathode location (dot), the canonical angular momentum is calculated from Eq. (6.2), and the solid line is this value extended along z. At other locations (circles), mechanical angular momentum is obtained from Eq. (6.6), and the dashed line is the average. The shaded areas have the same meanings as in Figure 6.11.

6.3   Study of the round-to-flat beam transformer

6.3.1   Demonstration of the removal of angular momentum

To remove angular momentum, it is necessary to apply a torque on the beam (see Section 3.4). A quadrupole can exert a net torque only on an incoming asymmetric beam. Thus more than one quadrupole is needed to remove the angular momentum of a cylindrically symmetric beam. The first quadrupole will introduce asymmetry in the x-y space as the beam drifts downstream, while the other quadrupoles downstream are properly tuned to apply a total net torque such that the angular momentum is removed at the exit of the quadrupole section.

For the series of measurements and simulations presented in this section, a set of three skew quadrupoles (Q1, Q2, Q4 in Figure 6.1) are used to remove the angular momentum and generate a flat beam.

Given the photoinjector parameters, numerical simulations of the beamline (from the photocathode up to the entrance of the transformer) are performed using ASTRA. The four-dimensional phase-space coordinates are propagated downstream of the transformer using a linear transfer matrix. The initial values of the skew quadrupole strengths are those derived, under the thin-lens approximation, in Ref. [44]. They are then optimized using a least-squares technique to minimize the x-y coupling terms of the beam matrix at the exit of the transformer. The final optimized quadrupole strengths are used for subsequent ASTRA simulation of the beam dynamics through the transformer.

Further empirical optimization around the predicted values is generally needed to insure the angular momentum is totally removed, as inferred by observation of the x-y coupling at several locations downstream of the transformer. Evolution of transverse density throughout the transformer is in good agreement with expectations from simulations, as shown in Fig. 6.14. Each of the top six photos is a superposition of 5 bunches with charge of 0.55 ± 0.10 nC. In the sequence of measurements and simulations presented there, the incoming round beam (X3) is transformed into a flat beam characterized by a large asymmetry (X7 and X8). The mechanical angular momentum is removed: there is no noticeable shearing as the beam propagates from

X7 to X8, which are separated by a 1.854 m drift.

6.3.2 Spacing between quadrupoles

There are four skew quadrupoles located downstream of the 9-cell cavity (see Figure 6.1); three could be chosen as a round-to-flat beam transformer. In order to decide which three to use, ASTRA simulations are done for all possible combinations. The skew quadrupole currents are listed in Table 6.2. We see that in some configurations higher currents are required than others. The corresponding flat-beam emittance ratio and rms beam sizes along the beamline are plotted in Figure 6.15.

Table 6.2: Skew quadrupole currents needed for flat beam generation when different skew quadrupoles are chosen.

quadrupole NOT used	quadrupole currents [A]			
	Q1	Q2	Q3	Q4
Q1	0	-2.1791	3.4585	-8.2714
Q2	-1.2534	0	2.6543	-5.7956
Q3	-1.8136	2.3313	0	-3.4472
Q4	-2.3971	4.6226	-14.8073	0

When Q1, Q2 and Q4 are chosen, the flat beam sizes diverge more slowly, and the minimum values are higher than the other combinations of quadrupoles. This is an advantage because a spot size that is too small is hard to measure due to the finite resolution of the measurement system and is more sensitive to the dispersion in the beamline, and a spot that is too big might fall out of the viewer area (round with diameter around 2.5 cm).
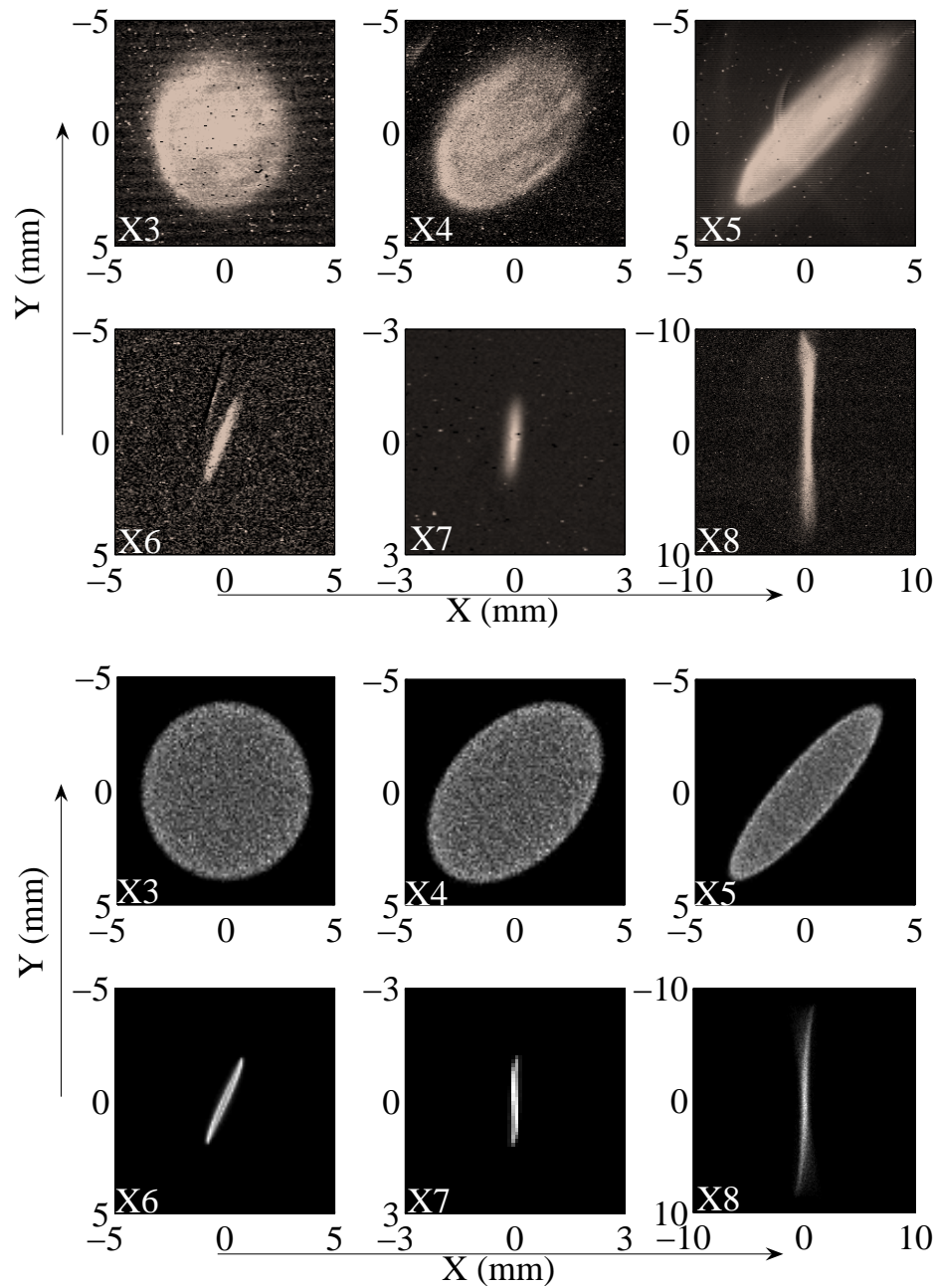
Figure 6.14: Measured (top six photos) and simulated (bottom six plots) beam transverse density evolution in the transformer. The consecutive plots correspond to locations X3, X4, X5, X6, X7 and X8 shown in Figure 6.1. The smaller strip on measured photo at X6 is *dark current* which consists of electrons produced by processes other than photo-emission.
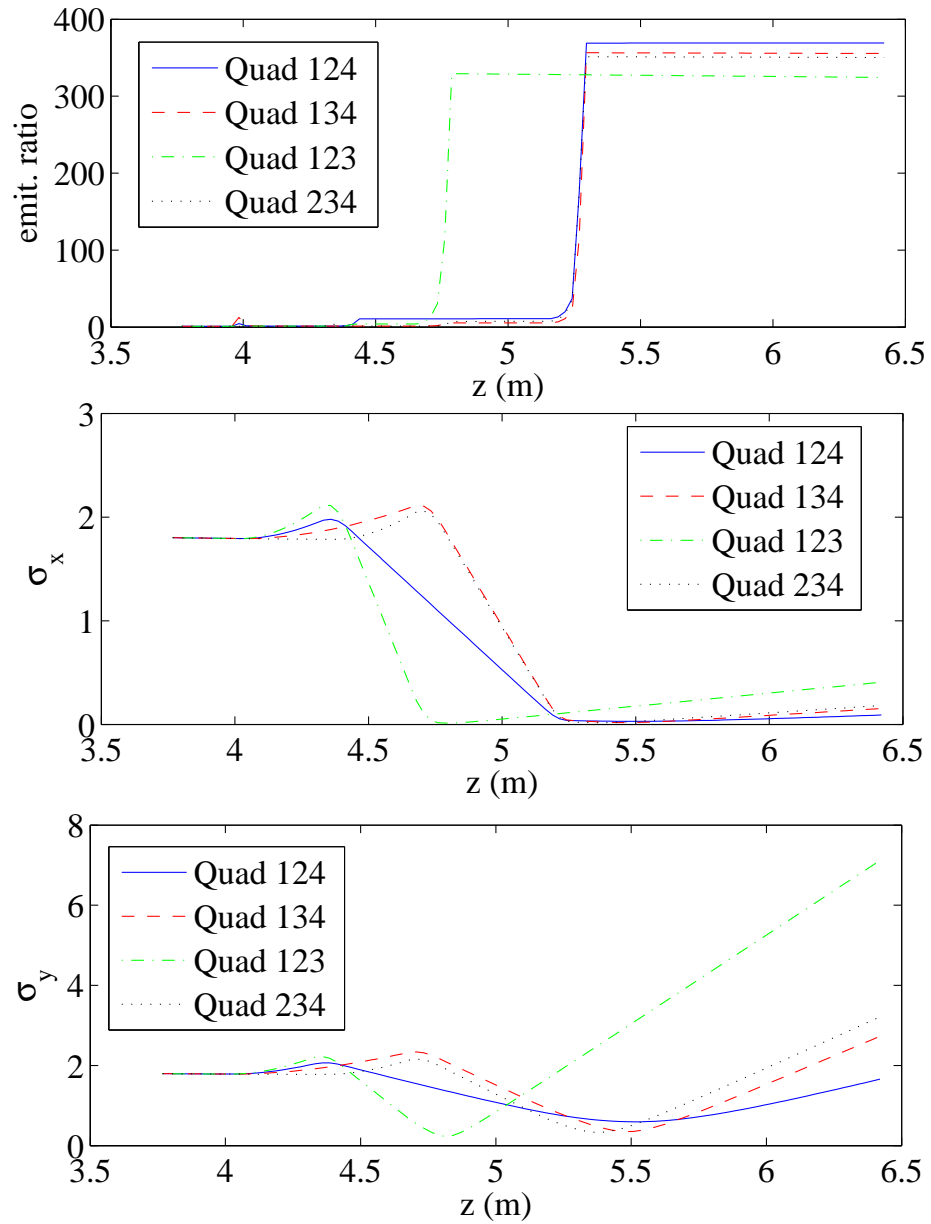
Figure 6.15: Effect of the quadrupole spacing on the emittance ratio and rms beam sizes from ASTRA simulations.

6.3.3   Quadrupole alignment error studies

Using skew quadrupoles Q1, Q2 and Q4, we numerically study the effects on the flat-beam emittance ratio caused by the quadrupole alignment error. This includes the rotational errors around the x, y and z axes, and the displacements dx, dy and dz.

The rotation angle around the longitudinal axis should be $45°$ for a skew quadrupole. In Figure 6.16, we scan the tilt angle of each quadrupole by $\pm 2°$ in simulation. The emittance ratio is more sensitive to the first and second quadrupole tilt angles, and much less sensitive to the third one. The results from ASTRA and ELEGANT agree with each other very well.

In Figure 6.17, we scan the angle around the horizontal axis (pitch) and vertical axis (yaw) by $\pm 2°$ using ASTRA . The maximum emittance ratio drop is less than 4%.

Finally we scan quadrupole center locations in each axis by a couple of millimeters. As seen from Figure 6.18, the effect on the emittance ratio is comparable to the misalignment in pitch and yaw angles. Usually the quadrupole centers are aligned within 1 mm mechanically.

From simulations shown above, we see that the emittance ratio is neither very sensitive to pitch and yaw rotation, nor to the quadrupole center displacements. The misalignment in some cases, e.g., center location in z-position, can be compensated by readjusting the quadrupole strengths. Furthermore, experimentally we do beam-based alignment by using a couple of steering magnets to center the beam on the electromagnetic axes of the quadrupoles. So in conclusion, we are not concerned with mechanical alignment of the quadrupole centers.

We see that the emittance ratio is sensitive to errors in the rotation angle of the first two skew quadrupoles. Experimentally, the precision of the alignment of the quadrupole angles is better than $\pm 0.25°$.
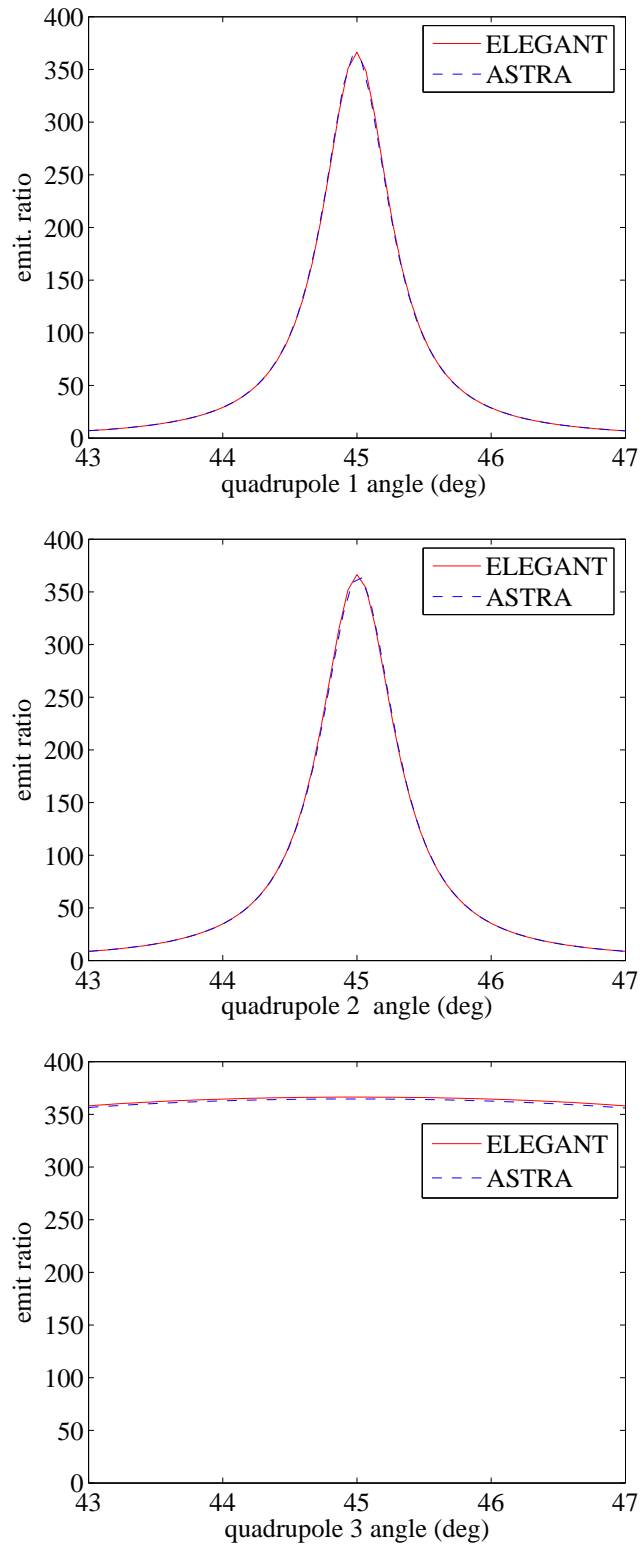
Figure 6.16: Effects of the quadrupole rotation angles around longitudinal axis on the emittance ratio from Astra and Elegant simulations.
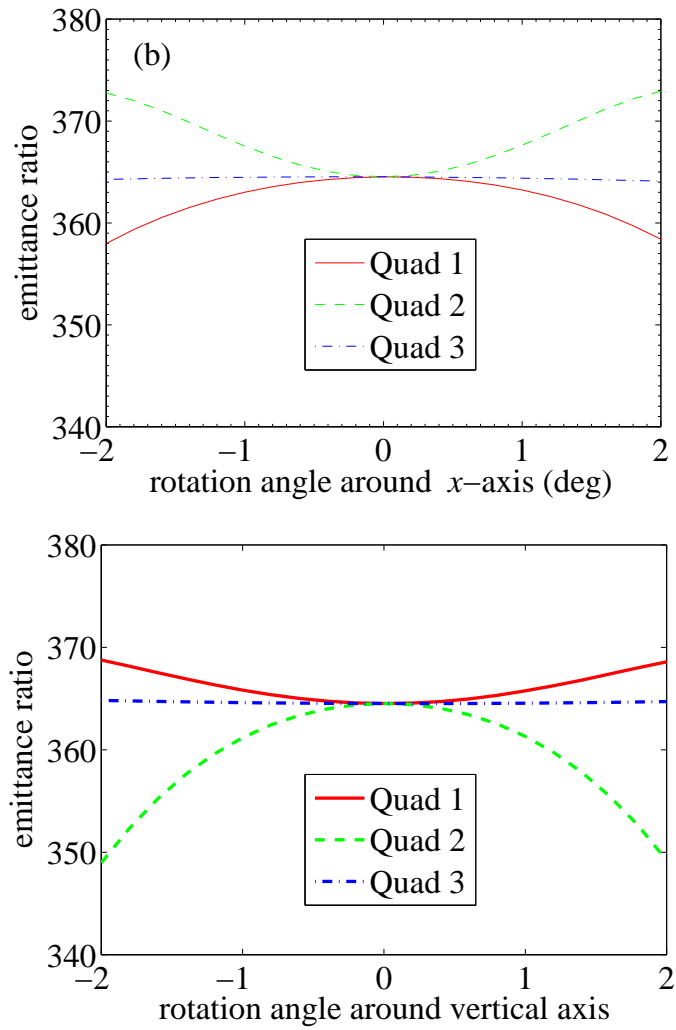
Figure 6.17: Effects of the quadrupole rotation angles around horizontal and vertical axis on the emittance ratio from ASTRA simulations.
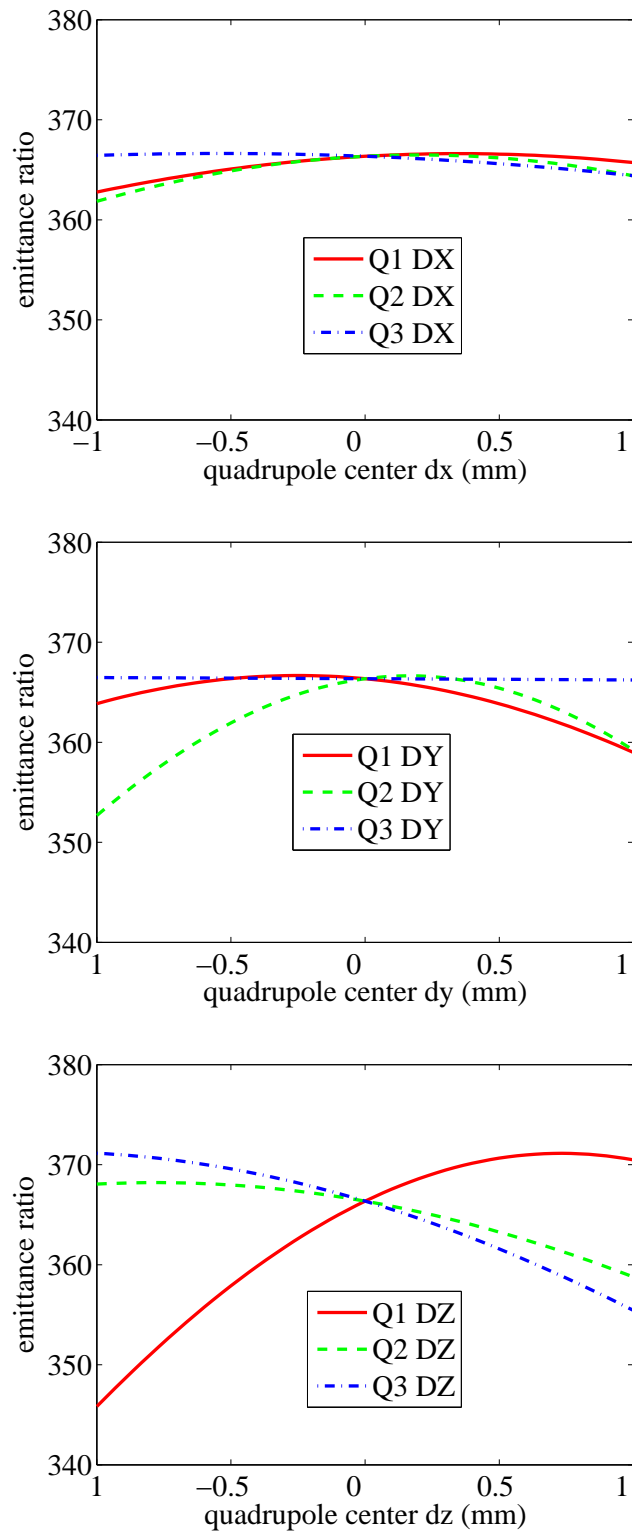
Figure 6.18: Effects of the quadrupole center locations on the emittance ratio.

6.4 Transverse emittance measurements

6.4.1 Measurement method

Introduction

We now discuss the apparatus used for the flat-beam emittance measurements using the *slit method.*

A screen can be inserted at location z_0 to measure the rms beam sizes σ_x and σ_y. If instead of a screen, a horizontal (vertical) slit is inserted at z_0, then only particles passing through the slit opening, i.e., the beamlet, will hit a screen downstream located at z. The vertical (horizontal) rms beam size of the horizontal (vertical) beamlet, σ_x^V (σ_y^H), is measured at location z. Assuming the slit opening is narrow such that it is uniformly illuminated by the beam at z_0, the rms beam divergence σ_x' and σ_y' at the slit location z_0 can be calculated via

$$\sigma_x' = \frac{\sqrt{(\sigma_x^V)^2 - \frac{w^2}{12}}}{z - z_0}, \tag{6.7}$$

$$\sigma_y' = \frac{\sqrt{(\sigma_y^H)^2 - \frac{w^2}{12}}}{z - z_0}, \tag{6.8}$$

where w is the full width of the slit opening. The rms beam emittances can be calculated via

$$\varepsilon_x = \sigma_x \sigma_x', \quad \varepsilon_y = \sigma_y \sigma_y'. \tag{6.9}$$

To measure σ_x^V and σ_y^H, we need to choose the proper slit configurations such as slit thickness along the z-axis, slit-opening width, separation between slits, and the distance between z_0 and z . It is also important to make sure that the smallest dimension that needs to be measured (σ_x^V in our case), is larger than the pixel size of the images taken by the digital cameras [79].

In order to optimize the emittance measurement configuration, numerical simulations are performed using the parameters given in Table 3.1. An angular-momentum-dominated beam is generated and propagated to the entrance of the transformer,

taking into account space-charge effects. The normalized uncorrelated beam emittance and the rms beam size along the beamline are shown in Figure 6.19.
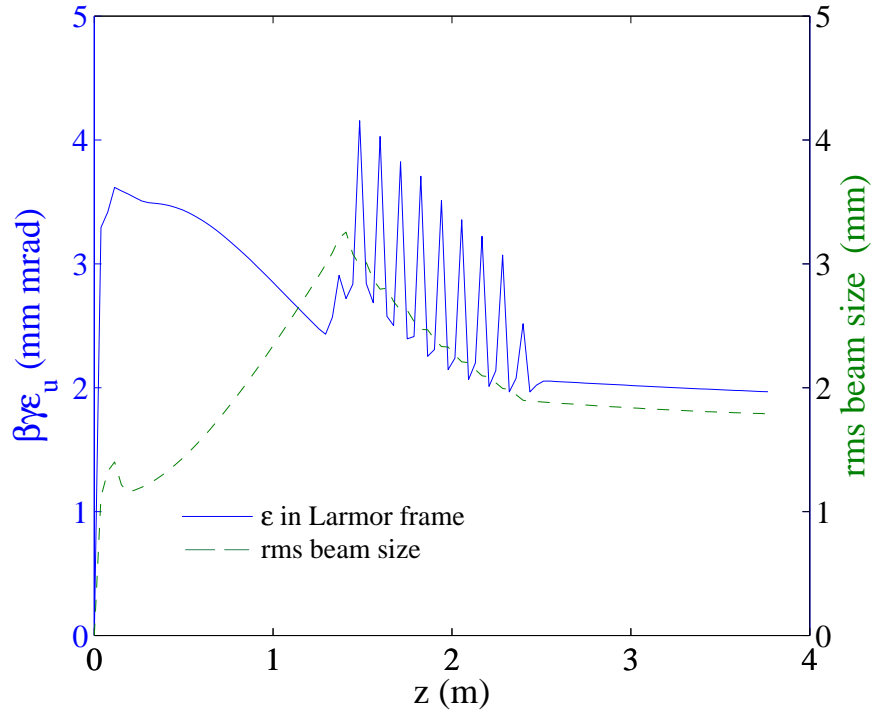
Figure 6.19: Normalized uncorrelated rms emittance and rms beam size of an angular-momentum-dominated beam before the transformer.

From the beam distribution at the transformer entrance, the initial 4×4 beam matrix Σ_0 is calculated and the two expected normalized flat-beam emittances are found to be, from Eq. (3.24):

$$\varepsilon_{nx} = 0.11 \text{ mm-mrad}; \quad \varepsilon_{ny} = 35.31 \text{ mm-mrad}. \tag{6.10}$$

As explained in Section 6.3.2, three skew quadrupoles located at $z_1 = 4.020$ m, $z_2 = 4.371$ m, $z_3 = 5.224$ m are chosen to form the transformer. The 4×4 transfer matrix of the transformer, M, is constructed analytically as a function of the quadrupole strengths. Given Σ_0 and M, the beam matrix at the exit of the transformer, Σ, is obtained from Eq. (3.17).

Two sets of solutions of the skew quadrupole strengths (in units of 1/m) are found

to transfer the round beam into a flat beam (see Section 6.3.1):

$$Q_k^1(1) = -1.6099, \quad Q_k^1(2) = +2.0653, \quad Q_k^1(3) = -3.0157;$$
$$Q_k^2(1) = +1.6299, \quad Q_k^2(2) = -2.5611, \quad Q_k^2(3) = -2.9878. \tag{6.11}$$

Taking 3-D space charge into account, the rms beam sizes and emittance ratio along the beamline for the two sets of solutions are plotted in Figure 6.20 and Figure 6.21.
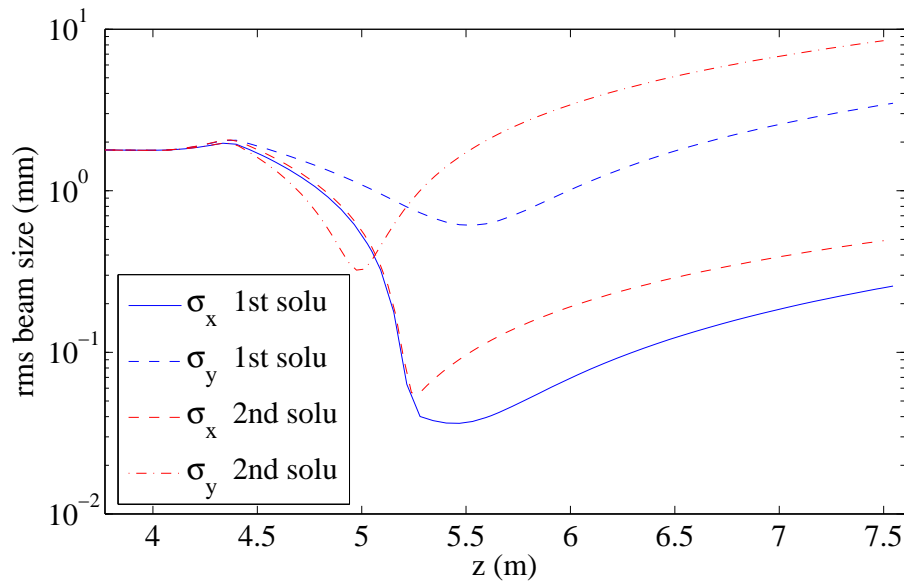
Figure 6.20: rms beam sizes during and after the round-to-flat beam transformer.

Choice of single-slit plate

Hereafter, we will use only the first solution set in our discussions.

Historically, both horizontal and vertical multislit tungsten plates were available at location $z = 5.62$ m. The slit width is 50μm and the space between two neighboring slits is 1 mm.

Inserting such a horizontal multislit plate in the beamline and observing the beamlets on a screen 40 cm downstream, we see that the beamlets passing through different slits are mixed; see Figure 6.22. This makes the measurements of the rms sizes of
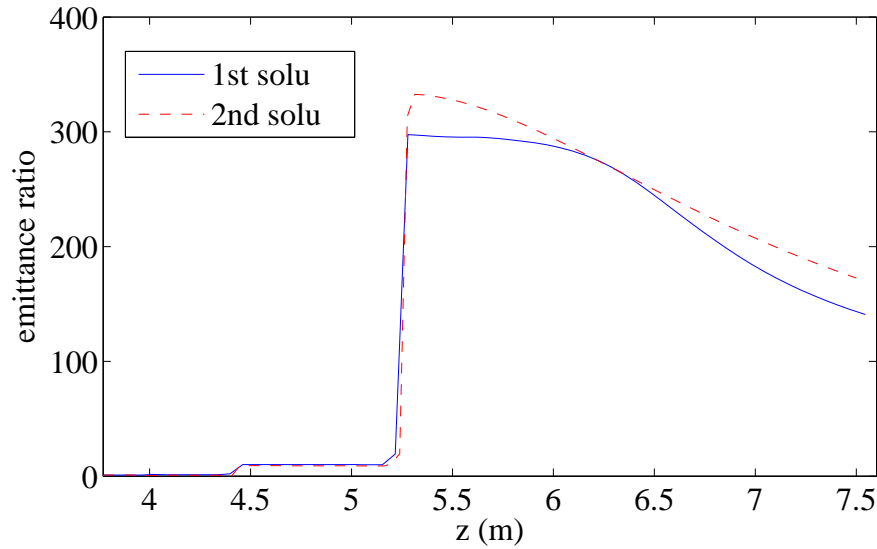
Figure 6.21: Beam emittance ratio along z-axis for the two sets of solutions of skew quadrupole strengths.

each beamlet difficult. Therefore we replace the multislit plates by movable single-slit plates.

The horizontal slit can be moved vertically to sample different vertical locations of the beam. An example of a horizontal slit inserted at the center and top of the beam is shown in Figure 6.23. Similarly, a single vertical slit movable in the horizontal direction is used to measure the horizontal beam divergence; see Figure 6.24.

Distance between slit and downstream viewer

In order to decide the best location of the screen for capturing the beamlet images, we track the beamlet in a drift downstream of the slit with 3D space charge on.

The rms size of the beamlets (σ_x^V and σ_y^H) along the beamline are plotted in Figure 6.25. The growth of σ_y^H is much larger than σ_x^V due to a much larger in emittance in (y, y') trace space. The YAG viewer has a diameter of 2.54 cm, therefore approximately a beam with rms size less than 0.5 mm may be fully captured on the viewer. We decided to locate the YAG screen at about 80 cm downstream of the slit. At this location, we have $\sigma_x^V = 70$ μm, $\sigma_y^H = 1.2$ mm. Given the camera calibration ($\approx 29\mu$m per pixel), σ_x^V is larger than the pixel size.
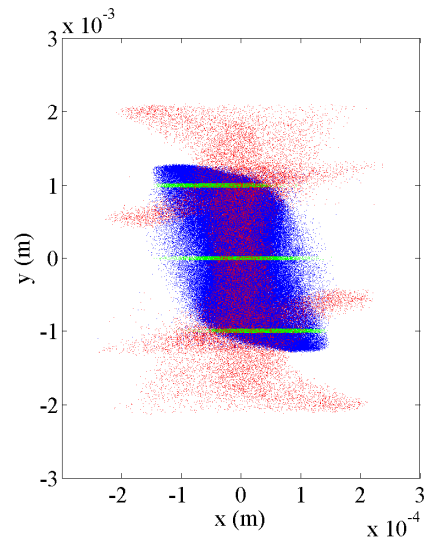
Figure 6.22: Beam on the viewer at $z = 5.62$ m (blue), horizontal slits inserted at the same location (green), and the beamlets as seen 40 cm drift downstream (red).
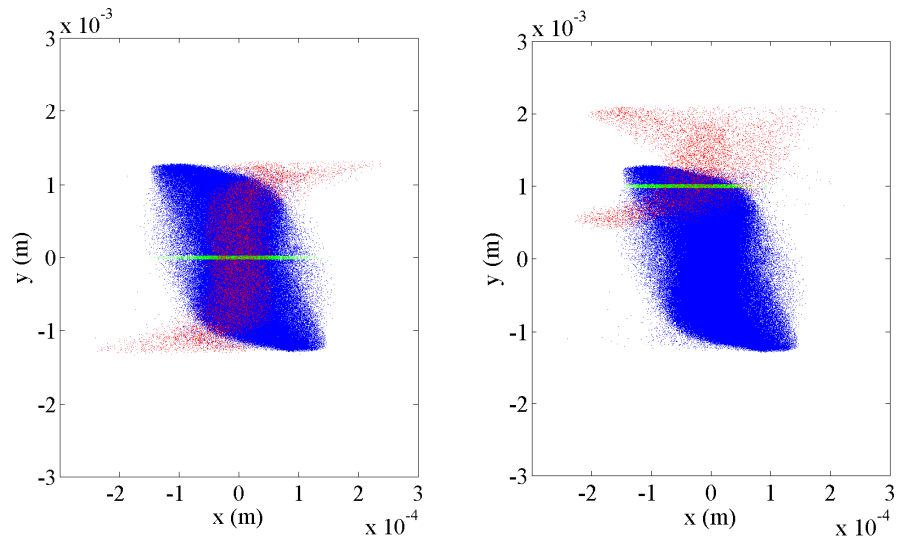
Figure 6.23: Beam on the viewer at $z = 5.62$ m (blue), a horizontal slit inserted at the same location (green) at the beam center or top, and the beamlets as seen 40 cm downstream (red).
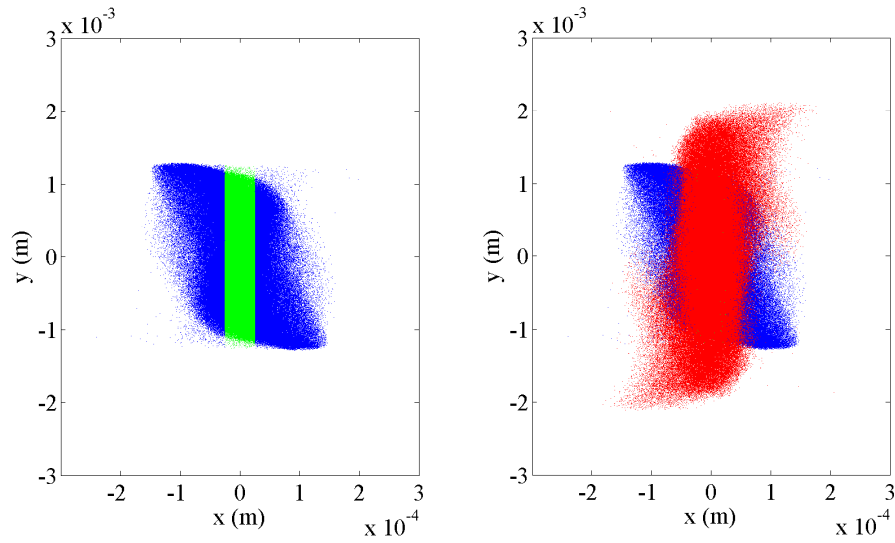
Figure 6.24: Beam on the viewer at $z = 5.62$ m (blue), a vertical slit inserted at the same location (green) at the center of the beam, and the beamlet as seen 40 cm downstream (red).
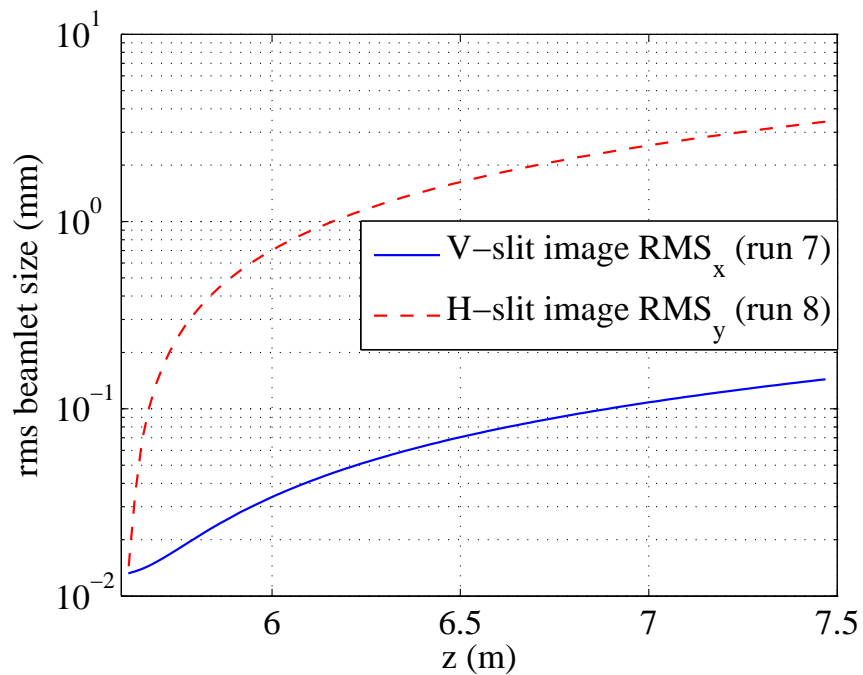
Figure 6.25: σ_x of a vertical beamlet and σ_y of a horizontal beamlet along the beam-line.

Thickness of the slit plate

Now we will turn to the discussion of the thickness of the tungsten plate. The nominal multislit plates are 6 mm thick. For the single-slit plate under consideration, we reconsidered the required slit thickness because only 2-mm-thick tungsten plates were available. The fraction of the beam that did not go through the slit should be either stopped or scattered at large angle. The rms angle of the scattered distribution, assumed to be Gaussian, is given by Molière theory [81]:

$$\langle\theta^2\rangle^{1/2} = \frac{13.6(\text{MeV})}{\beta c p} Z \sqrt{x/X_0}\left[1 + 0.038\log(x/X_0)\right], \qquad (6.12)$$

where p and Z are the particle incoming momentum and charge number, x is the particle path length in the material, and X_0 is the radiation length of the material (3.5 mm for tungsten [81]). Given the nominal operating energy of FNPL (~ 16 MeV), a tungsten segment of 2 mm thickness yields a rms scattering angle of 0.63 rad, which is much larger than the angular acceptance determined by the YAG viewer used to image the beamlet (which is 2 cm/80 cm≈ 25 mrad).

To refine our study, the computer program SHOWER [82] is used.[1] The beam is tracked through a 2 mm thick tungsten plate with a horizontal or a vertical slit of width 50 μm. The transverse beam distributions on a screen located 80 cm downstream are shown in Figure 6.26. These images are simulations of what one would observe experimentally on the YAG screen, including the resolution imposed by a 768×1024 pixel CCD array in the digital camera. The projections of the beamlet on x or y axis are also plotted in Figure 6.26. The noise observed at large positions with respect to the beam core corresponds to electrons that have been scattered with a small angle (for instance partially going through the slit and hitting the slit edge).

In Table 6.3 we summarize the results of computed beam and beamlet spot sizes along with the estimated transverse emittances. Our calculation indicates that the retrieved emittance from Eq. (6.9) matches the initial emittance computed for the incoming phase-space distribution within 15% approximately. Therefore we found

---

1. The input beam to SHOWER is generated by ASTRA simulation.

that a 2-mm-thick tungsten plate can be used as the single-slit plate.

Table 6.3: Summary of beam and beamlet transverse dimensions (σ and σ_{slit}) along with retrieved normalized emittance ε_r, compared with normalized emittance computed in the initial phase space (ε_i), given by Eq. (6.10).

	σ (μm)	σ_{slit} (μm)	σ_{slit} (μm)	ε_r (mm-rad)	ε_i (mm-rad)
horizontal	40.5	–	78.2	0.14	0.11
vertical	633.9	1484.7	–	40.97	35.31

Summary

We conclude that a tungsten plate with a single horizontal or vertical slit would be helpful to avoid the mixing of multiple beamlet. A YAG screen located 80 cm downstream of the slit provides a good compromise between capturing the whole horizontal beamlet image (whose rms size in y increases rapidly right after the slit) and getting enough resolution of the vertical beamlet image.

The slit plate thickness is reduced from 6 mm to 2 mm. This has the advantage of relaxing the angular alignment tolerance by a factor of 3.

6.4.2 Space-charge force manifested in (x, y) space

We now take a small detour from the emittance measurements. What is remarkable in Figure 6.22 is that the beamlet passing through the top horizontal slit has a "fishbone" shape after a drift (red dots). We can turn off the space charge from the photocathode to the end of the beamline and plot the corresponding beam distribution at the same longitudinal location; see Figure 6.27. The "fishbone" structure is gone. To further investigate this point, a simulation is run with space charge on before the transformer and off during the transformer; see Figure 6.28. The result closely resembles Figure 6.22. So the "fishbone" is caused primarily by the space charge force before the round-to-flat beam transformer. This agrees with our discussion in Section 4.3.
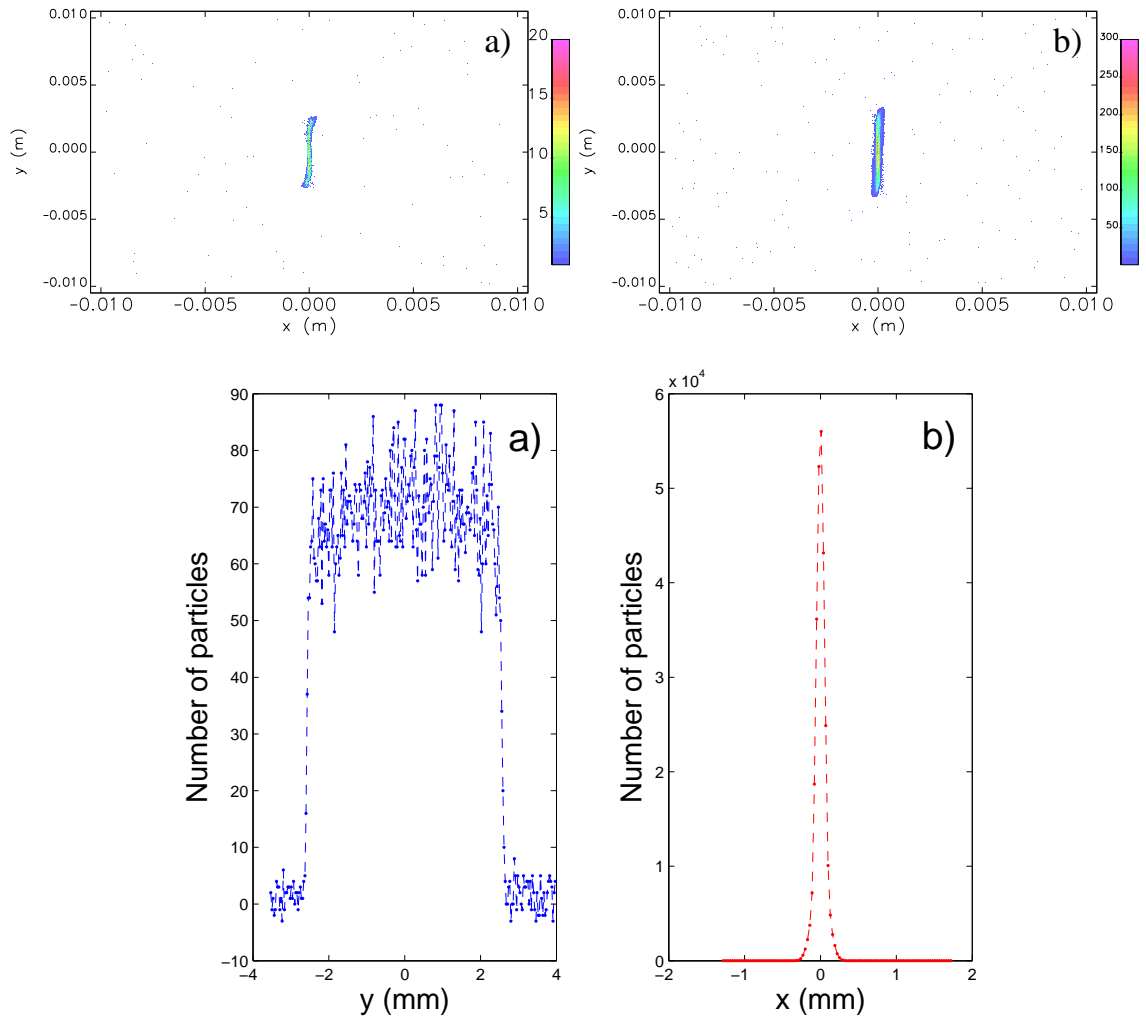
Figure 6.26: Top: Simulated images for a beamlet going through a horizontal a) and vertical b) slit. Bottom: The projections of the images along y or x axis, correspondingly.
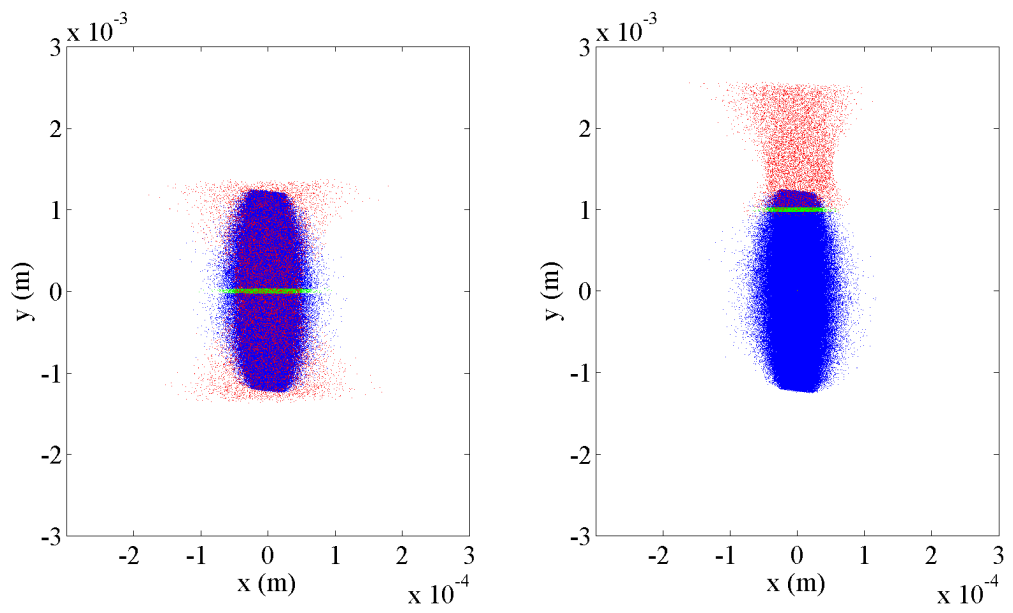
Figure 6.27: Space charge off from start to end: Beam on the viewer at $z = 5.62$ m (blue), horizontal slit inserted at the z-location (green) at the center and top of the beam, and the beamlets as seen 40 cm downstream of the slits (red).
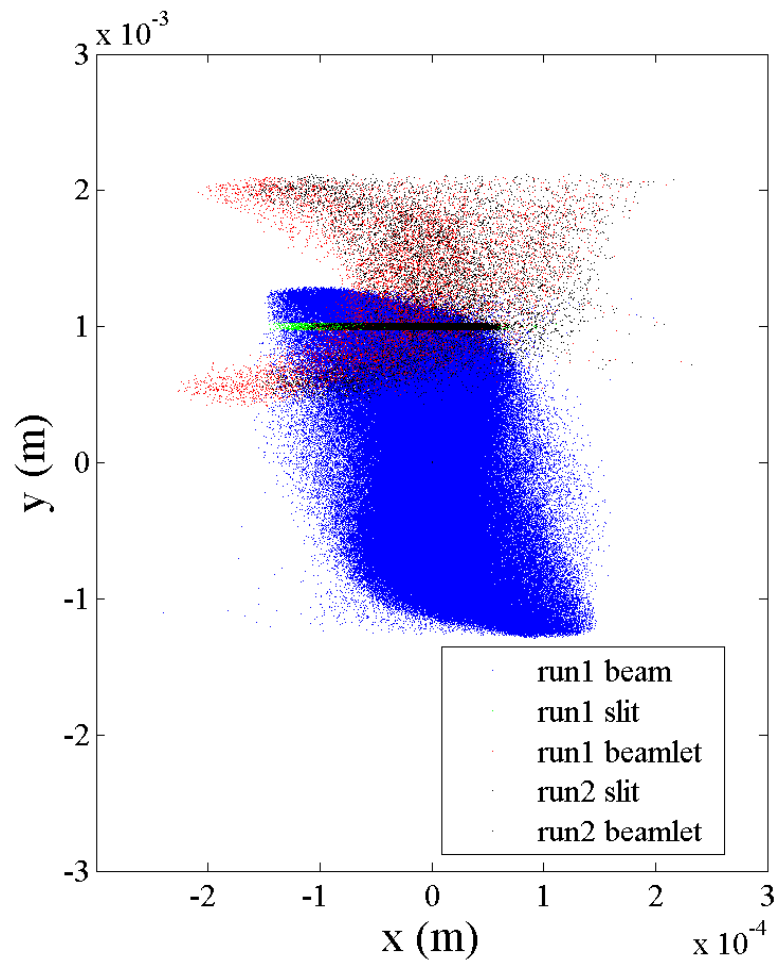
Figure 6.28: Space charge on: beam on the viewer at $z = 5.62$ m (blue), horizontal slits inserted at the same location (green) at the top of the beam and the beamlets as seen 40 cm downstream (red); and space charge off (black dots) only through the transformer (from $z = 3.77$ m to 7.50 m along the beamline).

6.4.3 Experimental results and comparison with simulations

Machine parameters

A flat beam is generated using the nominal machine parameters shown in Table 6.4. While the gun and booster-cavity settings are kept the same, the drive-laser spot size on the photocathode and the solenoid currents are adjusted for different sets of measurements.

Table 6.4: Nominal settings for the photocathode drive laser, rf gun and accelerating section during the flat-beam experiment.

parameter	value	unit
laser injection phase	25	degree
rms laser light size on cathode	$0.75 \sim 1$	mm
laser pulse duration (Gaussian)	3	ps
bunch charge	0.5	nC
E_z on cathode	32	MV/m
B_0 on cathode	~ 900	Gauss
booster cavity peak gradient	23	MV/m
main solenoid currents	~ 190	A
secondary solenoid current	~ 75	A
bucking solenoid current	0	A

Numerical simulations with ASTRA are performed using the parameters given in Table 6.4.

The initial skew quadrupole strengths are obtained from a least-squares MATLAB searching code, as explained in Section 6.4.1. The skew quadrupole strengths are then fine-tuned empirically by observing the beam on several viewers downstream of the transformer. Upon removal of the angular momentum, the beam should be flat and upright on all these viewers.

For two cases of rms laser spot sizes (0.76 mm and 0.97 mm), the final quadrupole currents used in the experiment and the initial values as used in ASTRA simulation are gathered in Tables 6.5 and 6.6.

Table 6.5: The skew quadrupole currents used in experiment and simulation for drive laser spot rms size around 0.76 mm. I_i stands for the current of the ith skew quadrupole.

quadrupole current	experiment	ASTRA
I_1 (A)	-1.92	-2.03
I_2 (A)	2.40	2.57
I_3 (A)	-2.99	-4.01

Table 6.6: The skew quadrupole currents used in experiment and simulation for drive laser spot rms size around 0.97 mm. I_i stands for the current of the ith skew quadrupole.

quadrupole current	experiment	ASTRA
I_1 (A)	-1.97	-1.98
I_2 (A)	2.56	2.58
I_3 (A)	-4.55	-5.08

Experimental and simulation results

In the measurements of transverse emittances, most of the images on an OTR or YAG screen are taken with a single-bunch beam. A set of experimental photos needed to get the two transverse flat-beam emittances is shown in Figure 6.29, along with the corresponding numerically simulated images. Several shots of each of the three images shown in Figure 6.29 are taken and analyzed to obtain the rms beam sizes. The results are then averaged and a statistical error is attributed to the mean. In Section 6.5, the details of data analysis are discussed.

The rms quantities of the beam, both experimentally measured and numerically simulated, are given in Tables 6.7 and 6.8 for the two different laser spot sizes on the photocathode, respectively. The transverse emittances along the beamline and the emittance ratio for the two cases are plotted in Figure 6.30.

The smaller of the two flat-beam normalized transverse emittance is measured to be $0.3 - 0.4$ mm-mrad, and the corresponding emittance ratio is around $70 - 90$.

Table 6.7: Drive laser spot rms size around 0.76 mm: flat-beam parameters measured and simulated.

parameter	experimental values 90%	95%	Astra simulation	unit
σ_{vc}	0.71±0.05	0.76±0.06	0.76	mm
σ_x^{X7}	0.077±0.005	0.087±0.006	0.047	mm
σ_y^{X7}	0.59±0.03	0.63±0.04	0.56	mm
$\sigma_x^{X8vslit}$	0.12±0.01	0.13±0.01	0.081	mm
$\sigma_x^{X8hslit}$	1.15±0.02	1.24±0.02	1.50	mm
ε_{nx}	0.36±0.04	0.45±0.06	0.18	mm-mrad
ε_{ny}	26±2	30±2	30	mm-mrad
$\varepsilon_{ny}/\varepsilon_{nx}$	73±10	68±10	165	
$\sqrt{\varepsilon_{ny}\varepsilon_{nx}}$	3.1±0.2	3.7±0.3	2.3	mm-mrad

Table 6.8: Drive laser spot rms size around 0.97 mm: flat-beam parameters measured and simulated.

parameter	experimental values 90%	95%	Astra simulation	unit
σ_{vc}	0.97		0.97	mm
σ_x^{X7}	0.084±0.001	0.095±0.001	0.058	mm
σ_y^{X7}	0.58±0.01	0.63±0.01	0.77	mm
$\sigma_x^{X8vslit}$	0.12±0.01	0.13±0.01	0.11	mm
$\sigma_x^{X8hslit}$	1.57±0.01	1.68±0.01	1.50	mm
ε_{nx}	0.39±0.02	0.49±0.02	0.27	mm-mrad
ε_{ny}	35.2±0.5	41.0±0.5	53	mm-mrad
$\varepsilon_{ny}/\varepsilon_{nx}$	90±5	83±4	196	
$\sqrt{\varepsilon_{ny}\varepsilon_{nx}}$	3.7±0.3	4.5±0.3	3.8	mm-mrad
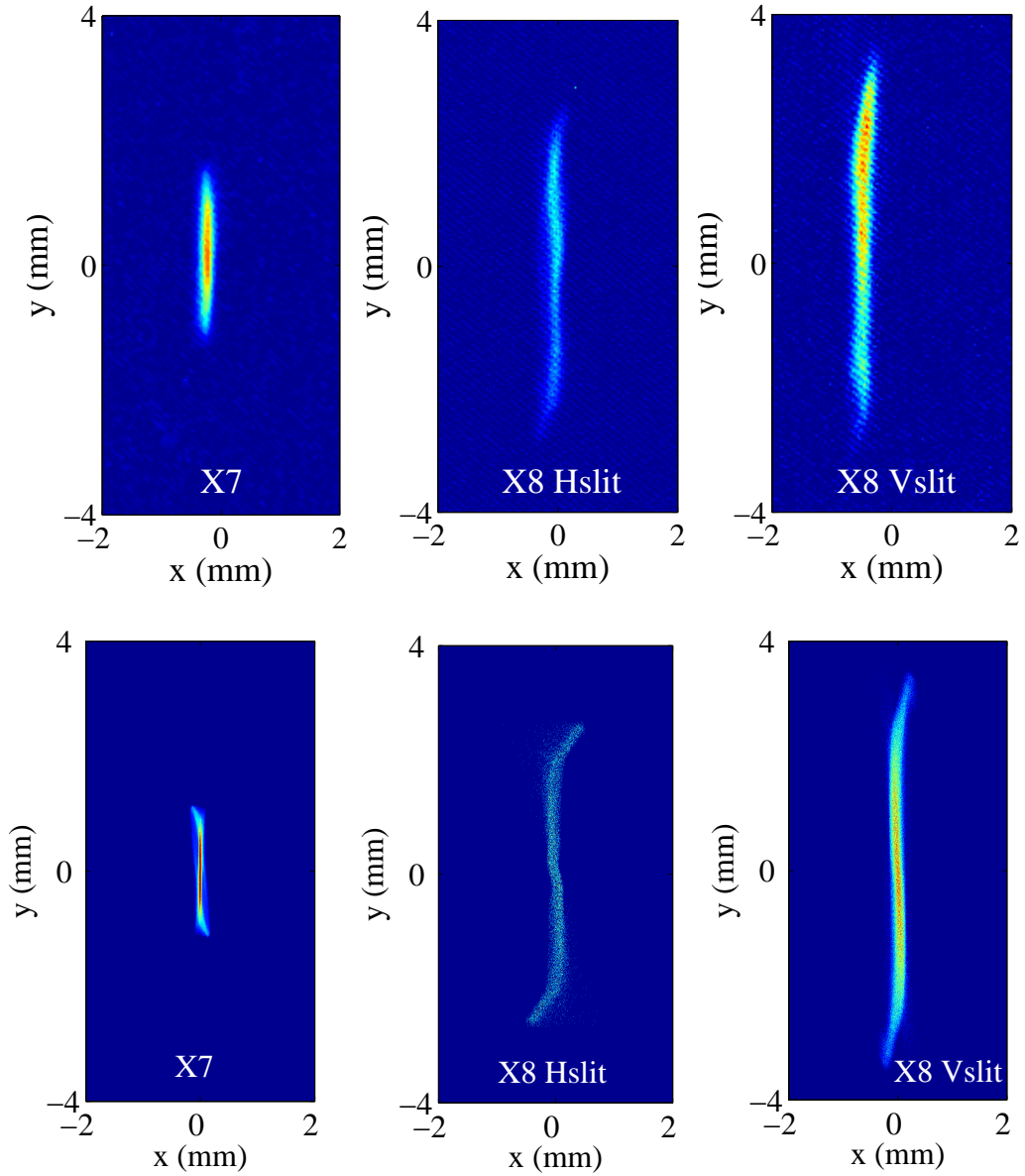
Figure 6.29: The top three images are taken by the digital cameras: beam at X7 (OTR viewer), horizontal and vertical slit images at X8 (YAG viewer). The bottom three are the corresponding beam profiles from ASTRA simulations. These images are associated with the flat beam presented in Table 6.7.
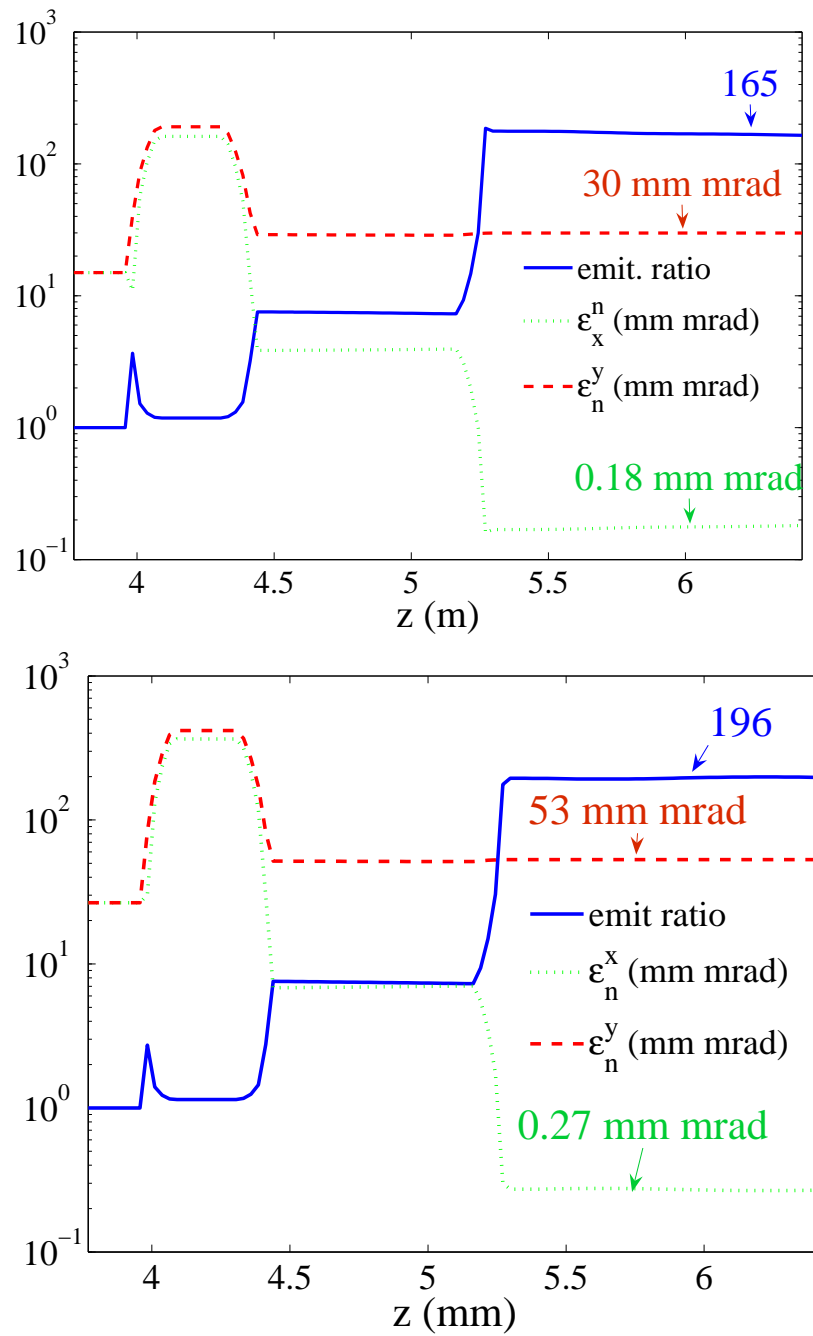
Figure 6.30: For laser spot size around 0.76 mm (top) and 0.97 mm (bottom): simulation results of the normalized transverse beam emittances and emittance ratio along z-axis as the beam propagates through the transformer.

Measurements of $\varepsilon_\pm = \sqrt{\varepsilon_u^2 + \mathcal{L}^2} \pm \mathcal{L}$ [Eq. (3.28)]

From Eq. (3.28), the expected normalized flat-beam emittances, $\varepsilon_n^\pm$, are given by

$$\varepsilon_n^\pm = \sqrt{(\varepsilon_n^u)^2 + (\beta\gamma\mathcal{L})^2} \pm (\beta\gamma\mathcal{L}), \qquad (6.13)$$

where $\varepsilon_n^u = \beta\gamma\varepsilon_u$ is the normalized uncorrelated emittance of the angular-momentum-dominated beam.

To complete the flat-beam experiment, it is of interest to extract experimentally the expected flat-beam emittances from the angular-momentum-dominated beam, and compare them with the flat-beam emittances measured downstream of the transformer. The quantities that need to be measured are $\mathcal{L}$ and the uncorrelated rms emittance ε_u of the angular-momentum-dominated beam.

$\mathcal{L}$ is related to the canonical angular momentum of the beam via Eq. (3.14). As detailed in Section 6.2.1, the canonical angular momentum can be measured either from Eq. (6.2) or Eq. (6.6). Corresponding to these two ways of measuring angular momentum, $\mathcal{L}_1$ or $\mathcal{L}_2$ is obtained from Eq. (3.14).

Meanwhile, the uncorrelated normalized rms emittance ε_n^u can be measured using the slit method from the beam image at X3 and beamlet image at X5.

The results of such measurements on an angular-momentum-dominated beam are presented in Table 6.9. The corresponding flat beam is presented in Table 6.8, from which some of the relevant parameters are extracted and listed in Table 6.9 for comparison.

We see that for the smaller flat-beam emittance, the two experimental values agree very well. Both are significantly larger than simulated values, which may be attributed to camera resolution, beamline dispersion and the transformer alignment errors; see Section 6.4.3.

In the case of the larger flat-beam emittance, the measured value of the round beam agrees well with simulation, and both are about 25% higher than the value measured from the actual flat beam. This might caused by some imperfection in the setup of the round-to-flat beam transformer.

Table 6.9: Parameters (all in mm-mrad) measured from the angular-momentum-dominated round beam and the corresponding flat beam. To calculate $\varepsilon_n^{\pm}$, $\mathcal{L}$ is taken as the average of $\mathcal{L}_1$ and $\mathcal{L}_2$. The "flat beam" column is extracted from Table 6.8.

parameters	round beam (95%)	flat beam (95%)	simulation
$\beta\gamma\mathcal{L}_1$	24.5±0.7	–	26.1
$\beta\gamma\mathcal{L}_2$	26.6±0.5	–	26.4
ε_n^u	5.1±0.7	4.5±0.3	3.8
$\varepsilon_n^+ = \sqrt{(\varepsilon_n^u)^2 + (\beta\gamma\mathcal{L})^2} + (\beta\gamma\mathcal{L})$	53.8±0.9	41.0±0.5	53
$\varepsilon_n^- = \sqrt{(\varepsilon_n^u)^2 + (\beta\gamma\mathcal{L})^2} - (\beta\gamma\mathcal{L})$	0.49±0.13	0.49±0.02	0.27

Sources of expansion for very small beams

We see in Tables 6.7 and 6.8 that for the larger beam dimensions (σ_y's), the measured values are in good agreement with simulation results. However, for the smaller dimensions which are of the order of 10's of μm, the simulation values are much smaller than the measured ones. The smaller the rms size, the larger is the discrepancy. This might be attributed to two different sources: the dispersion in the beamline, and the camera resolution. Let the dispersion along the beamline be η, the rms energy spread of the beam be δ, and camera resolution be σ_{res}; the measured rms beam size is:

$$\sigma = \sqrt{\sigma_0^2 + \eta^2\delta^2 + \sigma_{\mathrm{res}}^2} \;, \tag{6.14}$$

where σ_0 represents the emittance contribution to the rms beam size.

As an example, let's look into the values of σ_x^{X7} in Tables 6.7 and 6.8. Simulation shows that $\sigma_x^{X7} = 47$ μm and 58 μm, respectively. The rms energy spread of the beam δ is around 0.15% for bunch charge around 0.5 nC; the dispersion η at X7 is estimated using code ELEGANT with the magnet strength from experiment to be around 4 cm, and the best measured camera resolution is around 1.2 pixels $\approx$ 35 μm (see Section 5.4.1; here the calibration is about 29 μm/pixel). From Eq. (6.14) we have $\sigma_x^{X7} \approx 83$ μm and 90 μm, respectively. These results are within 5% of the measured values shown in Tables 6.7 and 6.8.

In the numerical example above, we used reasonable estimated values for dis-

person and best measured camera resolution. In fact the dispersion at each viewer location depends on the settings of magnetic elements, such as the steering magnets and quadrupoles. The camera resolution is related to the camera iris settings, which is detailed in Section 5.4.1.

Table 6.10: Corrected flat-beam parameters for drive laser-spot rms size around 0.76 mm: the contribution from the camera resolution is subtracted quadratically from the measured values.

parameter	corrected experimental values		unit
	90%	95%	
σ_x^{X7}	0.069±0.004	0.080±0.006	mm
σ_y^{X7}	0.59±0.03	0.63±0.04	mm
$\sigma_x^{X8vslit}$	0.11±0.01	0.12±0.01	mm
$\sigma_x^{X8hslit}$	1.15±0.02	1.24±0.02	mm
ε_{nx}	0.29±0.03	0.37±0.05	mm-mrad
ε_{ny}	26±2	30±2	mm-mrad
$\varepsilon_{ny}/\varepsilon_{nx}$	90±12	81±12	

Table 6.11: Corrected flat-beam parameters for drive laser-spot rms size around 0.97 mm: the contribution from the camera resolution is subtracted quadratically from the measured values.

parameter	corrected experimental values		unit
	90%	95%	
σ_x^{X7}	0.076±0.001	0.088±0.001	mm
σ_y^{X7}	0.58±0.01	0.63±0.01	mm
$\sigma_x^{X8vslit}$	0.11±0.01	0.12±0.01	mm
$\sigma_x^{X8hslit}$	1.57±0.01	1.68±0.01	mm
ε_{nx}	0.32±0.02	0.41±0.02	mm-mrad
ε_{ny}	35.2±0.5	41.0±0.5	mm-mrad
$\varepsilon_{ny}/\varepsilon_{nx}$	110±7	100±5	

The *true* flat-beam emittances, i.e., the emittances one would have measured with zero dispersion and infinitely small camera resolution, are less than those presented in Tables 6.7 and 6.8. The upper limit of the true flat-beam emittances could be obtained by subtracting quadratically the best measured camera resolution contribution from

the measured rms beam size; see Tables 6.10 and 6.11. Therefore the best flat-beam emittance ratio measured at 95% of beam intensity is 100 ± 5 for bunch charge 0.5 nC and beam energy around 16 MeV .

Reproductivity of flat-beam experiment

Finally it is worth to point out that the examples of the flat beam reported in this section are readily repeatable in experiment. Once the rf gun, booster cavity and drive-laser spot size are set to the nominal values, a flat beam can be reproduced by reloading the corresponding values of currents into solenoids, skew quadrupoles, and steering magnets.

6.5 Data reduction and error analysis

6.5.1 Introduction

Transverse beam rms size is obtained by analyzing the images of the light produced by an electron bunch when it hits on a viewer (see Section 5.4.1). Several sources of error need to be addressed, such as area-of-interest, criteria to determine rms beam size and the corresponding error and background level.

We start by taking an image of the viewer with beam on it, then closing the UV laser-beam shutter and taking another image of the viewer with only background signals which includes *dark currents*.[2] Subtracting the background from the beam image, we obtain a clean image of the beam, as shown in Figure 6.31.

6.5.2 Area-of-interest

To calculate beam rms sizes, we take the projections of the beam image on the x or y-axis. Usually for the projection, an *area-of-interest* is chosen instead of the

---

2. Dark currents consist of parasitic electrons produced by mechanisms (e.g., field emission or secondary emission) other than photoemission; with proper initial conditions, dark currents could be accelerated by the rf cavities.

whole 1024×768 square-pixel image, as shown in Figure 6.31. We will now discuss the effect of the size of the area-of-interest on rms beam size calculation.
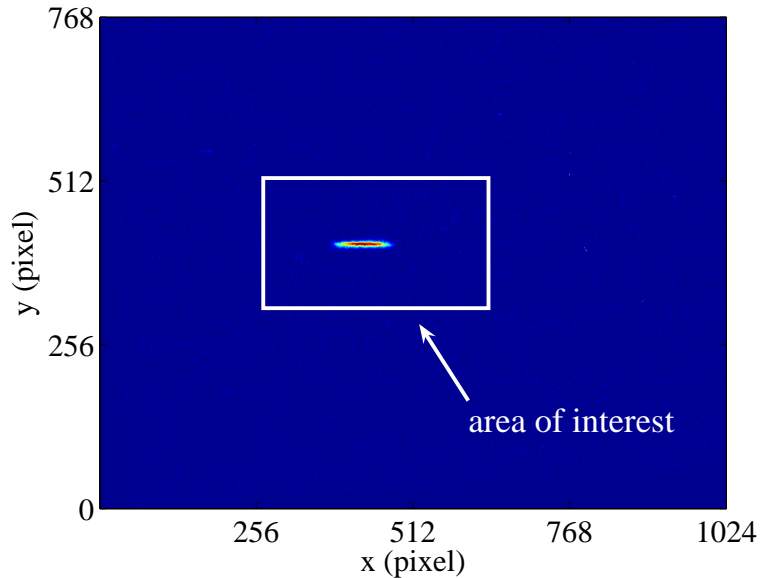
Figure 6.31: An example of beam image with background signals subtracted. A white rectangular is drawn to illustrate a possible "area-of-interest" for rms size calculation.

In the following discussions, we take the calculation of σ_x as an example (the calculation of σ_y is similar.). Keeping the beam roughly centered in the area-of-interest, we take the projection of the area-of-interest on the x axis; see Figure 6.32. The beam center x_0 is calculated as the mean of the projection. Starting from x_0 and increasing the number of pixels on both sides of x_0 symmetrically to a range of $[x_{\min}, x_{\max}]$, the rms value is calculated via

$$\sigma_x = \left[\frac{\int_{x_{\min}}^{x_{\max}} x^2 I(x) \mathrm{d}x}{\int_{x_{\min}}^{x_{\max}} I(x) \mathrm{d}x} - \left(\frac{\int_{x_{\min}}^{x_{\max}} x I(x) \mathrm{d}x}{\int_{x_{\min}}^{x_{\max}} I(x) \mathrm{d}x} \right)^2 \right]^{1/2}, \tag{6.15}$$

where $I(x)$ is the intensity of the projection. The results are shown in Figure 6.33. As the number of pixels between $[x_{\min}, x_{\max}]$ increases, the rms size also increases; however, there is a clear shoulder indicating the correct rms beam size.
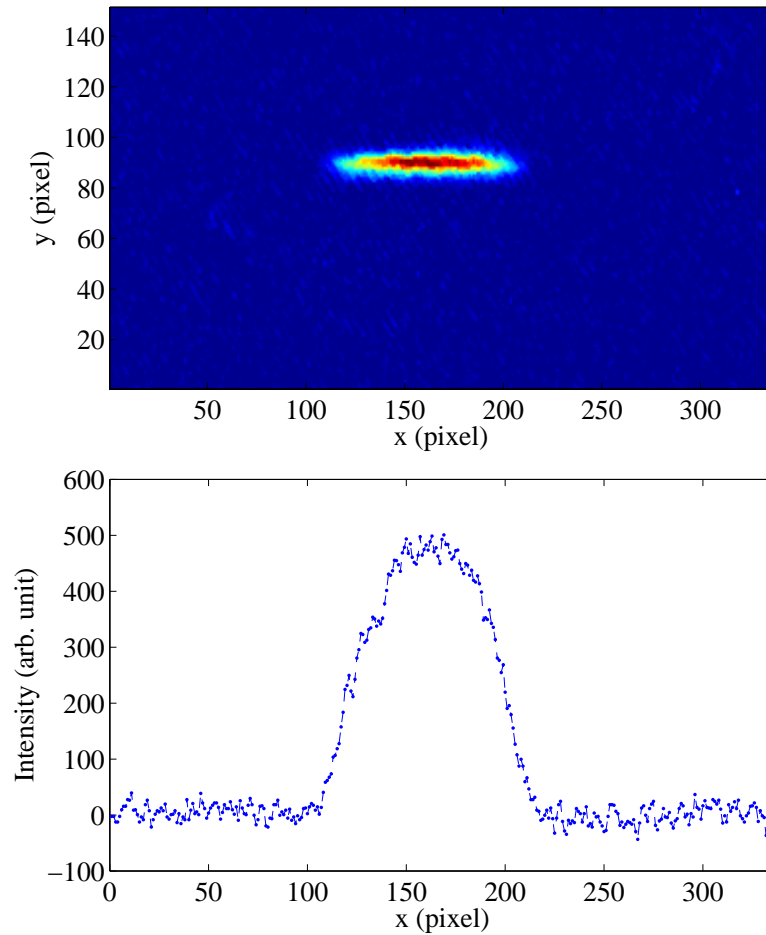
Figure 6.32: An area-of-interest is chosen (top) to take the projection on the x-axis (bottom).

6.5.3   rms sizes at certain percentage of the beam

Instead of using the absolute number of pixels, we can plot σ_x versus the percentage of area in $[x_{\min}, x_{\max}]$ versus the total area under the projection curve, i.e., *percentage-of-the-beam*, see Figure 6.34. Therefore it makes sense to talk about rms beam size at a certain percentage-of-the-beam. As an example, in Figure 6.34, σ_x at 95% is 22.74 ± 0.14 pixels.
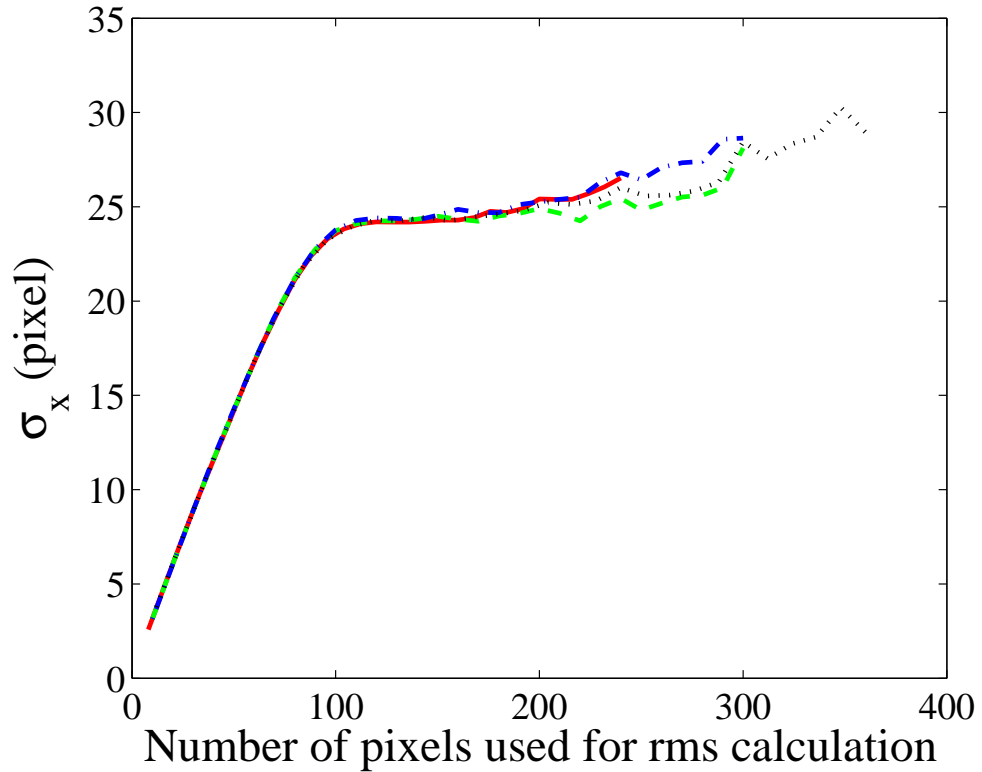
Figure 6.33: A shoulder appears as the data range is increased symmetrically around the beam center. Different lines represents different sizes of initial area-of-interest.

6.5.4   Background level

Now we turn to the discussion of the choice of background level. Let the average background of the projection be $I_{\mathrm{bk}} \pm \sigma_{\mathrm{bk}}$, which can be calculated from the projection curve far from the beam signal area. For a certain range of $[x_{\min}, x_{\max}]$, backgrounds from $I_{\mathrm{bk}} - \sigma_{\mathrm{bk}}$ to $I_{\mathrm{bk}} + \sigma_{\mathrm{bk}}$ are subtracted from the projection $I(x)$ in several steps, and the rms sizes calculated for each background level are shown in Figure 6.35.

6.5.5   The case of Gaussian distribution

In the discussion above, we used a real beam image whose projection on the x-axis is far from Gaussian. However the discussion results are not sensitive to the detailed shapes of beam distributions. To show this, we consider the case of a Gaussian
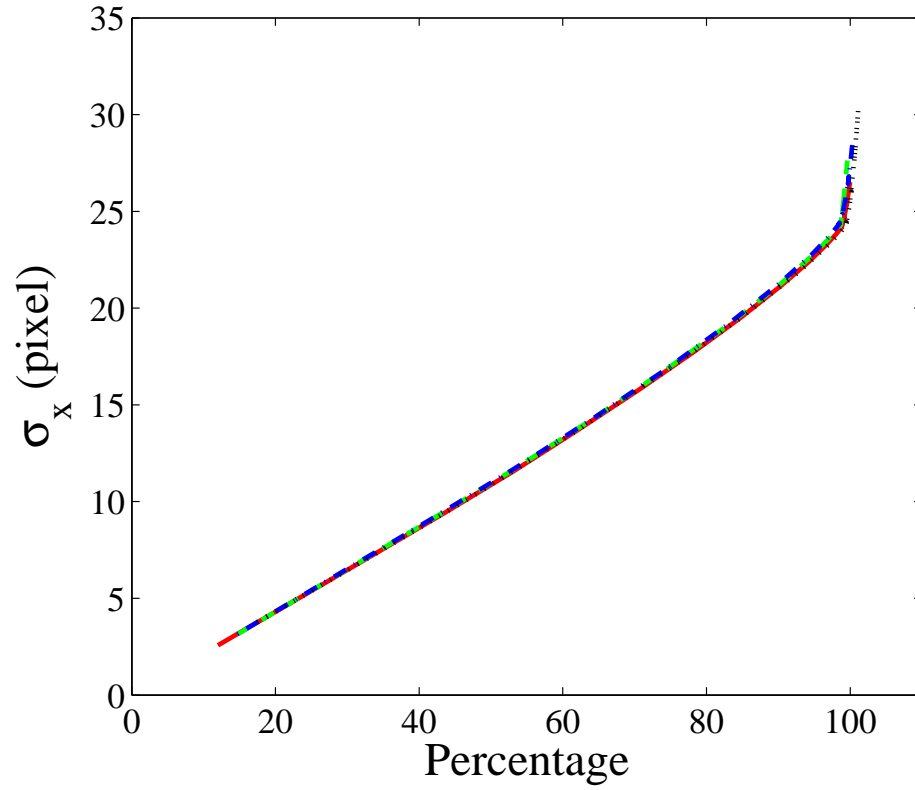
Figure 6.34: Calculated rms beam size as a function of the percentage-of-the-beam.

distribution

$$I(x) = e^{-(x-x_0)^2/2\sigma_x^2}, \tag{6.16}$$

where $x_0 = 50$, $\sigma_x = 5$; see Figure 6.36 (a). The rms sizes calculated for different sizes of area-of-interest are shown in Figure 6.36 (b) and (c). Similar to the previous example, we see that a clear shoulder appears in Figure 6.36 (b), and the rms size at a certain percentage-of-the-beam is well defined in Figure 6.36 (c).
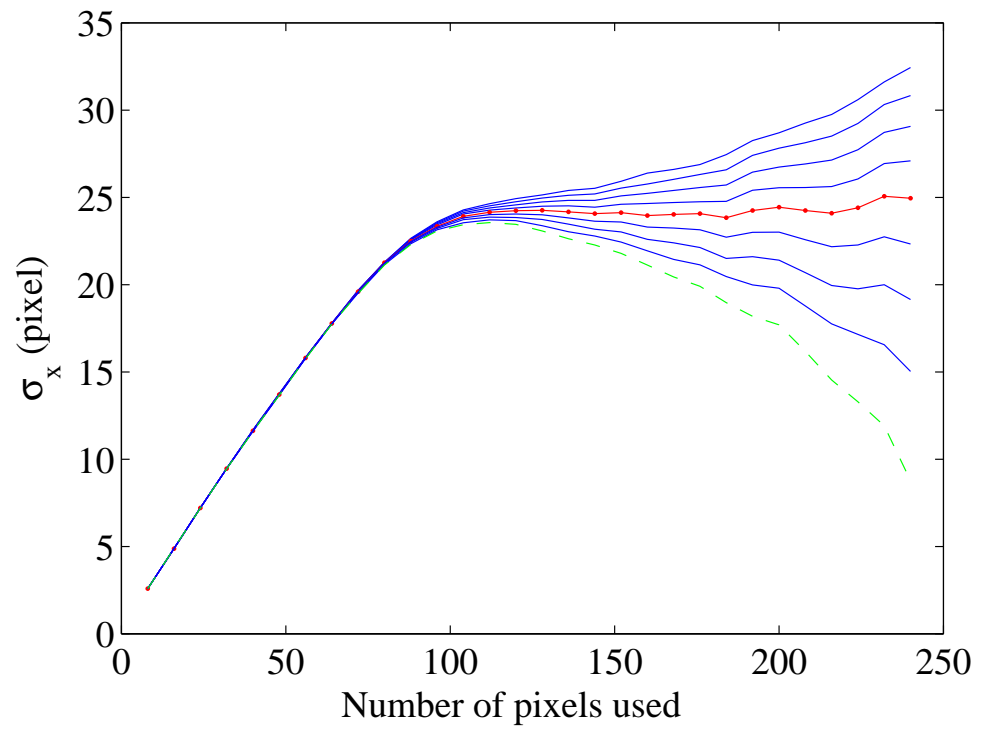
Figure 6.35: rms beam size calculated at different background levels but within the same window of $[x_{\min}, x_{\max}]$. Background level is raised by $2\sigma_{\mathrm{bk}}$ from top line to bottom line, with red line with dot marker using the correct background level (I_{bk}).
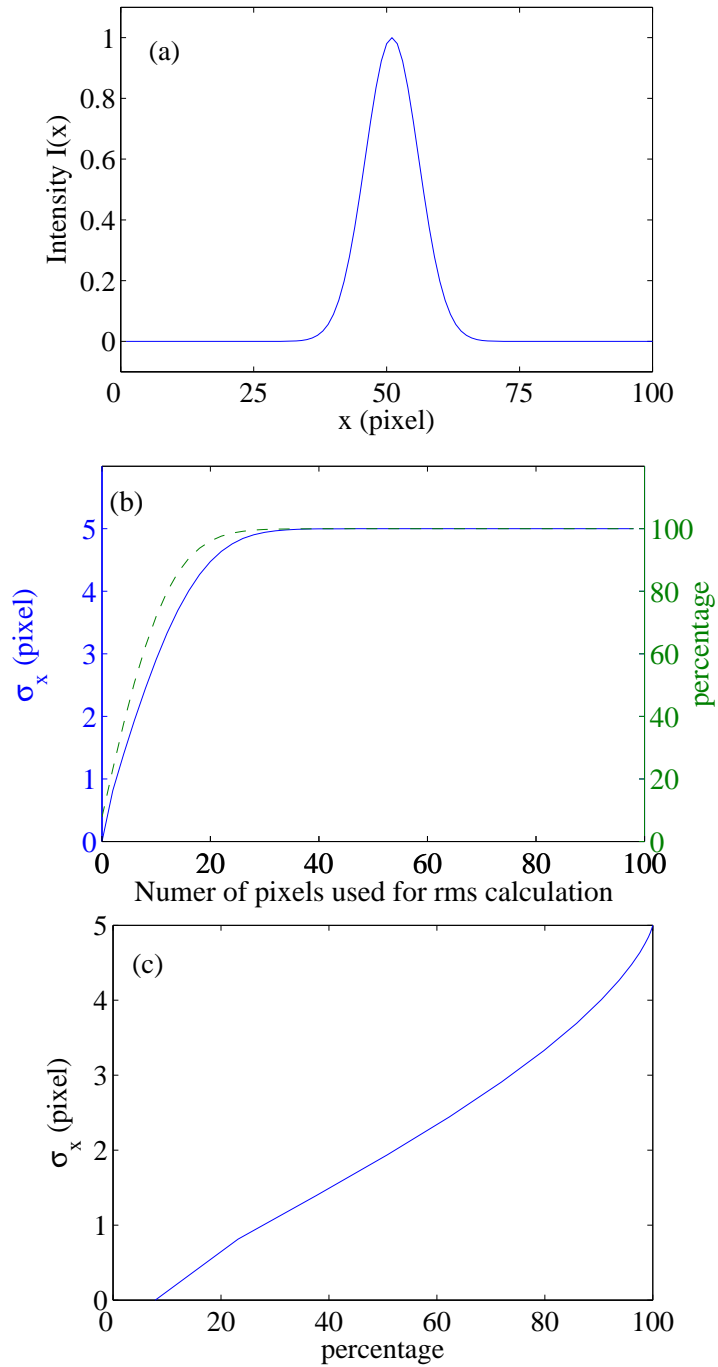
Figure 6.36: rms size of a perfect Gaussian distribution. (a) Gaussian distribution generated from Eq. (6.16); (b) calculated rms size (solid line) and percentage-of-the-beam (dashed line) as a function of absolute number of pixels used for the calculation; (c) calculated rms size versus percentage-of-the-beam.

CHAPTER 7
CONCLUSIONS

In this dissertation we have studied theoretically and experimentally the principles and limitations of flat beams − beams with a large ratio of emittances in the two transverse directions. The experiment was carried out at FNPL. The facility consists of a laser-driven photocathode rf gun in which electron beams are generated and accelerated to 4.5 MeV, a booster cavity to further accelerate the beam to 16 MeV, and a beam manipulation section thereafter.

The first step in the flat-beam generation is the production of round, angular-momentum-dominated beams by immersing the photocathode and rf gun in an axial magnetic field. The dependencies of angular momentum on initial conditions such as photocathode drive-laser spot size, the strength of the magnetic field, etc., were measured and found to be in good agreement with predictions based on theory and simulation.

The second step is to remove the angular momentum of the beam after the booster cavity. This is achieved by means of three skew quadrupoles (referred to as the round-to-flat beam transformer). The quadrupoles are skewed so that the beam emittance is small (large) in the horizontal (vertical) direction. In the pioneering experiment by D. Edwards et al. [27, 28], an emittance ratio of $40 - 50$ was reported. The ratio is improved to 100 ± 5 in the present experiment for a bunch charge of 0.5 nC. The emittance ratio could become even higher by removing the horizontal dispersion.

Several factors contributed to this improvement. First, a least-squares method was used to predict the optimal quadrupole strengths based on the more accurate knowledge of the incoming angular-momentum-dominated beam. While a further tuning of the quadrupole strengths was generally required, the final values agree with the predicted values within 10%. Second, special care is taken to center the beam via steering dipoles at each quadrupole location. Third, the emittance diagnostics was improved. Single-bunch[1] measurement was possible with the upgraded camera

---

1. A single-bunch consists of electrons generated by a single UV laser light pulse at 1 Hz repetition frequency. In contrast, a multi-bunch is generated by a train of laser pulses separated by 1 μs, see

system, thus eliminating the error caused by taking beam images of a bunch train consisting of bunches of different charges. Finally, the resolution of the measurement system was improved by a factor of two.

We have investigated various factors limiting the flat-beam production, such as thermal emittance, space-charge effects, chromatic effects, and asymmetry in the angular-momentum-dominated beam. The influences of the skew quadrupole alignments on flat-beam emittance ratio are also studied. Among the six degrees of freedom for each quadrupole, rotations around the longitudinal axis of the first two quadrupoles are found to be the most influential on the flat-beam emittances. Among all the limiting effects we studied, the space-charge effect in the gun area turns out to be the most important one: It gives rise to the uncorrelated transverse emittance, resulting in a reduction in the achievable flat-emittance ratio from orders of thousands to hundreds.

Among various applications discussed in Chapter 2, the one for the linear collider is probably the most challenging in emittance requirements. For example, the TESLA-500 GeV (center-of-mass energy) design requires transverse emittances of 0.03 mm-mrad (vertical) and 10 mm-mrad (horizontal) at the interaction point for a bunch charge of 3.2 nC [83]. While this is difficult to achieve with the current machine parameters at FNPL, it is shown with simulations in Ref. [24] that such emittances could be obtained with a specially designed photoinjector.[2] Comparing to FNPL machine parameters (see Table 6.4), higher rf gun accelerating gradient and the magnetic field on photocathode are used; more importantly, a flat-top laser pulse of duration 100 ps is chosen to reduce the space-charge effects in the rf gun area.

Another important application of the flat-beam technique is for producing ultrashort x-ray pulses as proposed for the LUX project [32, 86]. The requirement for this application appears to be within the capability of the current state-of-art. The horizontal emittance obtained at FNPL is already the one specified by the LUX

---

the time structure of the UV laser pulse in Figure 5.4. The intensity fluctuation in the laser pulse train results in bunch charge variation in a multi-bunch electron beam.

2. Linear collider also requires the electron beam to be polarized. For example, TESLA-500 assumes 80% electron polarization. Special photocathode material such as gallium arsenide could be used to generate polarized electrons, as demonstrated at SLAC and Nagoya [84, 85].

design. However, the bunch charge for the LUX project is 1 nC − twice that in our experiment. We can predict what emittances are achievable at FNPL for 1 nC bunches. After optimizing the machine parameters, we found numerically that normalized emittances of 0.4 mm-mrad and 24 mm-mrad could obtained for rms laser spot size around 0.68 mm at FNPL. These values meet the design goal of LUX. It should be noted that in our case the transformation is performed at 16 MeV instead of 120 MeV as designed in LUX; we are therefore more sensitive to chromatic and space-charge effects. So the simulation result is favorable.

We see that for the two applications of flat beam discussed above, the requirements on the emittances, bunch charge and beam energy are all different. In both cases, simulation shows that flat beams of the required parameters are feasible. The experimental results obtained at FNPL, together with the good agreement obtained with simulations, are very encouraging for further improvement of flat-beam generation.

APPENDIX A

TRANSVERSE EMITTANCES OF AN UNCOUPLED BEAM

Denote the coordinates of a particle in transverse trace space by two vectors:

$$X = \begin{bmatrix} x \\ x' \end{bmatrix} \text{ and } Y = \begin{bmatrix} y \\ y' \end{bmatrix}. \tag{A.1}$$

If the beam is not coupled initially, the 4×4 beam matrix can be written as

$$\Sigma_i = \begin{bmatrix} \langle X\widetilde{X} \rangle & 0 \\ 0 & \langle Y\widetilde{Y} \rangle \end{bmatrix}. \tag{A.2}$$

From Eq. (1.30), the initial emittances are

$$\varepsilon_{x0}^2 = |\langle X\widetilde{X} \rangle|, \quad \varepsilon_{y0}^2 = |\langle Y\widetilde{Y} \rangle|. \tag{A.3}$$

Let M be the symplectic transfer matrix between position i and f:

$$M = \begin{bmatrix} A & B \\ C & D \end{bmatrix}. \tag{A.4}$$

From Eq. (1.31), the transformation of the beam matrix is given by

$$\Sigma_f = M\Sigma_i\widetilde{M}, \tag{A.5}$$

which is

$$\Sigma_f = \begin{bmatrix} A\langle X\widetilde{X} \rangle\widetilde{A} + B\langle Y\widetilde{Y} \rangle\widetilde{B} & A\langle X\widetilde{X} \rangle\widetilde{C} + B\langle Y\widetilde{Y} \rangle\widetilde{D} \\ A\langle X\widetilde{X} \rangle\widetilde{C} + B\langle Y\widetilde{Y} \rangle\widetilde{D} & C\langle X\widetilde{X} \rangle\widetilde{C} + D\langle Y\widetilde{Y} \rangle\widetilde{D} \end{bmatrix}. \tag{A.6}$$

The final emittances are

$$\varepsilon_x^2 = |A\langle X\widetilde{X} \rangle\widetilde{A} + B\langle Y\widetilde{Y} \rangle\widetilde{B}|,$$
$$\varepsilon_y^2 = |C\langle X\widetilde{X} \rangle\widetilde{C} + D\langle Y\widetilde{Y} \rangle\widetilde{D}|. \tag{A.7}$$

139

Introduce the *symplectic conjugate* of a 2×2 matrix defined by:

$$A^\dagger = J^{-1}\widetilde{A}J, \tag{A.8}$$

where J is the 2×2 unit symplectic matrix,

$$J = \begin{bmatrix} 0 & 1 \\ -1 & 0 \end{bmatrix}. \tag{A.9}$$

Direct calculation shows that

$$A^\dagger A = |A|I_2, \tag{A.10}$$

where $I_i(i =\text{integer})$ is the $i \times i$ identity matrix.

Similarly, the symplectic conjugate of M is

$$M^\dagger = J_4^{-1}\widetilde{M}J_4 \tag{A.11}$$

where J_4 is given by:

$$J_4 = \begin{bmatrix} J & 0 \\ 0 & J \end{bmatrix}. \tag{A.12}$$

It follows from Eq. (A.11) that

$$M^\dagger M = J_4^{-1}\widetilde{M}J_4 M = J_4^{-1}J_4 = I_4, \tag{A.13}$$

where we used the symplectic condition $\widetilde{M}J_4 M = J_4$, and I_4 is the 4×4 identity matrix.

Substituting Eq. (A.6) into Eq. (A.13), we obtain

$$\begin{bmatrix} A^\dagger A + C^\dagger C & A^\dagger B + C^\dagger D \\ B^\dagger A + D^\dagger C & B^\dagger B + D^\dagger D \end{bmatrix} = I_4, \tag{A.14}$$

i.e.,

$$A^\dagger A + C^\dagger C = I_2, \quad B^\dagger B + D^\dagger D = I_2, \tag{A.15}$$

$$A^\dagger B + C^\dagger D = 0, \quad B^\dagger A + D^\dagger C = 0. \tag{A.16}$$

Eqs. (A.10) and (A.15) yield

$$|A| + |C| = 1, \quad |B| + |D| = 1. \tag{A.17}$$

Similarly by calculating $MM^\dagger$ one can show that

$$|A| + |B| = 1, \quad |C| + |D| = 1. \tag{A.18}$$

From Eqs. (A.17) and (A.18), we have

$$|A| = |D|, \quad |B| = |C|, \tag{A.19}$$

which is a result of M being symplectic.

Using the fact that for two 2×2 matrices P and Q,

$$|P + Q| = |P| + |Q| + \mathrm{Tr}(P^\dagger Q), \tag{A.20}$$

Eq. (A.21) can be written as

$$\begin{aligned}
\varepsilon_x^2 &= |A|^2 \varepsilon_{x0}^2 + |B|^2 \varepsilon_{y0}^2 + \mathrm{Tr}\big[\big(A\langle X\widetilde{X}\rangle\widetilde{A}\big)^\dagger (B\langle Y\widetilde{Y}\rangle\widetilde{B})\big], \\
\varepsilon_y^2 &= |C|^2 \varepsilon_{x0}^2 + |D|^2 \varepsilon_{y0}^2 + \mathrm{Tr}\big[\big(C\langle X\widetilde{X}\rangle\widetilde{C}\big)^\dagger (C\langle Y\widetilde{Y}\rangle\widetilde{C})\big],
\end{aligned} \tag{A.21}$$

Using $\langle X\widetilde{X}\rangle = \langle \widetilde{X}X\rangle$ and $J^{-1} = -J$, we have

$$\begin{aligned}
&\mathrm{Tr}\big[\big(A\langle X\widetilde{X}\rangle\widetilde{A}\big)^\dagger (B\langle Y\widetilde{Y}\rangle\widetilde{B})\big] \\
&= \mathrm{Tr}\big[\big(J^{-1}A\langle X\widetilde{X}\rangle\widetilde{A}J\big)(B\langle Y\widetilde{Y}\rangle\widetilde{B})\big] \\
&= \mathrm{Tr}\big[-A\langle X\widetilde{X}\rangle JJ^{-1}\widetilde{A}JB\langle Y\widetilde{Y}\rangle JJ^{-1}\widetilde{B}J)\big] \\
&= \mathrm{Tr}\big[-\langle X\widetilde{X}\rangle JA^\dagger B\langle Y\widetilde{Y}\rangle JB^\dagger A\big].
\end{aligned} \tag{A.22}$$

Similarly,

$$\text{Tr}\big[(C\langle X\widetilde{X}\rangle\widetilde{C})^{\dagger}(C\langle Y\widetilde{Y}\rangle\widetilde{C})\big]$$
$$=\text{Tr}\big[-\langle X\widetilde{X}\rangle JC^{\dagger}D\langle Y\widetilde{Y}\rangle JD^{\dagger}C)\big]. \tag{A.23}$$

From Eq. (A.16) we have

$$\text{Tr}\big[-\langle X\widetilde{X}\rangle JA^{\dagger}B\langle Y\widetilde{Y}\rangle JB^{\dagger}A)\big] = \text{Tr}\big[-\langle X\widetilde{X}\rangle JC^{\dagger}D\langle Y\widetilde{Y}\rangle JD^{\dagger}C)\big]; \tag{A.24}$$

thus

$$\text{Tr}\big[\big(A\langle X\widetilde{X}\rangle\widetilde{A}\big)^{\dagger}(B\langle Y\widetilde{Y}\rangle\widetilde{B})\big] = \text{Tr}\big[\big(C\langle X\widetilde{X}\rangle\widetilde{C}\big)^{\dagger}(C\langle Y\widetilde{Y}\rangle\widetilde{C})\big]. \tag{A.25}$$

From Eqs. (A.21), (A.17), (A.19) and (A.25), we have

$$\varepsilon_x^2 - \varepsilon_y^2 = \varepsilon_{x0}^2(|A|-|C|) - \varepsilon_{y0}^2(|B|-|D|) = \big(\varepsilon_{x0}^2 - \varepsilon_{y0}^2\big)(|A|-|C|). \tag{A.26}$$

From Eq. (A.26) we see for an initially uncoupled beam, if the emittances are equal, i.e., $\varepsilon_{x0} = \varepsilon_{y0}$, then at all points downstream, the emittances ε_x and ε_y are also equal [9].

APPENDIX B
THE END FIELD OF A SOLENOIDAL LENS

Let B_z be the longitudinal magnetic field which is large on the photocathode and zero at the exit of the solenoidal field. Consider Maxwell's Equation

$$\nabla \cdot \vec{B} = 0.$$

In circular cylindrical coordinates, we have

$$\frac{1}{r}\frac{\partial(rB_r)}{\partial r} + \frac{\partial B_z}{\partial z} = 0$$

$$\Rightarrow B_r = -\frac{r}{2}\frac{\partial B_z}{\partial z} \Rightarrow \begin{cases} B_x = -\frac{x}{2}\frac{\partial B_z}{\partial z}, \\ B_y = -\frac{y}{2}\frac{\partial B_z}{\partial z}. \end{cases}$$

If electron trajectories remain close to the longitudinal axis in the solenoidal field region, then to the first order, $B_z(r, z) = B_z(r = 0, z) = B_z(z)$ and $\frac{\partial B_z}{\partial z} = \frac{dB_z}{dz}$.

The Lorentz force $\vec{F}$ on an electron with velocity $\vec{v}$ from the magnetic field $\vec{B}$ is given by

$$\vec{F} = e\vec{v} \times \vec{B} \Rightarrow \begin{cases} F_x = -ev_zB_y = +\frac{1}{2}ev_zy\frac{dB_z}{dz}, \\ F_y = +ev_zB_x = -\frac{1}{2}ev_zx\frac{dB_z}{dz}. \end{cases} \tag{B.1}$$

From the equation of motion, assuming that v_z is a constant, we have

$$\begin{aligned} F_x &= \gamma m\ddot{x} = \gamma mv_z^2x'', \\ F_y &= \gamma m\ddot{y} = \gamma mv_z^2y''. \end{aligned} \tag{B.2}$$

Eq. (B.1) and Eq. (B.2) yield

$$\begin{aligned} \frac{dx'}{dz} &= +\frac{ey}{2p_z}\frac{dB_z}{dz}, \\ \frac{dy'}{dz} &= -\frac{ex}{2p_z}\frac{dB_z}{dz}. \end{aligned} \tag{B.3}$$

where $p_z = \gamma mv_z$ is the longitudinal momentum.

Integrating Eq. (B.3) over z from the photocathode location ($B_z = B_c$) to the exit

of the solenoidal field ($B_z = 0$), we obtain the changes in the phase space coordinates x' and y', $\Delta x'$ and $\Delta y'$ as

$$\Delta x' = -\kappa y, \quad \Delta y' = +\kappa x,$$

where $\kappa = \frac{eB_c}{2p_z}$ and x, y are assumed to be constant. So the electron trace space coordinates become

$$X = \begin{bmatrix} x \\ x' - \kappa y \end{bmatrix}, \quad Y = \begin{bmatrix} y \\ y' + \kappa x \end{bmatrix}. \tag{B.4}$$

APPENDIX C

COUPLER-KICK-INDUCED EMITTANCE GROWTH

As the rf waveguide is side-coupled to the rf gun's full-cell (see Figure 5.5), the cylindrical symmetry of the gun is broken. Consequently, the electrons receive a vertical kick as they pass through the rf coupler region.

Consider the following picture: An electron is traveling on the electromagnetic (EM) axis, which is the same as the geometric axis of the rf gun, until it reaches the coupler region. In this region, the maximum E_z is shifted vertically due to cylindrical symmetry being broken by the rf coupler, and the EM axis is shifted by h vertically away from the geometric axis; see Figure C.1. We assume that the transverse deflection of the beam is small so the beam is still traveling on the geometric axis, but it receives a vertical kick which we call "coupler kick" hereafter.
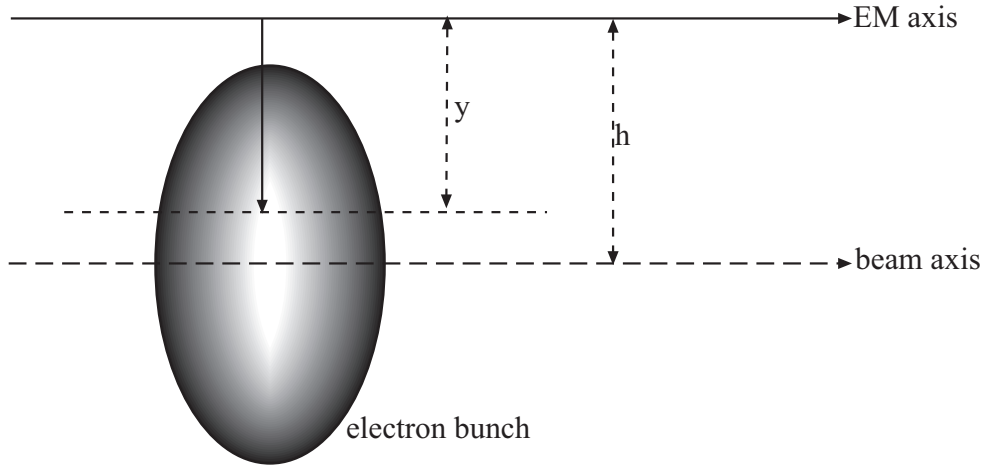
Figure C.1: Electromagnetic axis and the beam axis in the coupler region.

In the coupler kick region, write the longitudinal electric field on the EM axis as

$$E_z = E_0 \cos(kz) \sin(\omega t + \phi_0) \tag{C.1}$$

where E_0 is the peak accelerating field, k is the rf wave number, $\omega = ck$, c being the speed of light.

From Eq. (24) and (25) of Ref. [14], the vertical force F_y and the change in vertical momentum Δp_y can be expressed as

$$
\begin{aligned}
F_y &= -\frac{eE_0 y}{2c}\frac{\mathrm{d}}{\mathrm{d}t}[\sin(kz)\cos(\omega t + \phi_0)], \\
\Delta p_y &= \int \frac{1}{mc}F_y \mathrm{d}t = -\frac{eE_0 y}{2mc^2}\int_{\text{coupler region}} \mathrm{d}[\sin(kz)\cos(\omega t + \phi_0)].
\end{aligned}
\tag{C.2}
$$

Let $\phi = \omega t + \phi_0 - kz$, $\alpha = \frac{eE_0}{2mc^2 k}$, z_i and z_f be the start and end of the coupler region. We have

$$
\Delta p_y = -\alpha k y[\sin(kz_f)\cos(\phi_f + kz_f) - \sin(kz_i)\cos(\phi_i + kz_i)].
\tag{C.3}
$$

Ignoring the small phase slippage of the electrons in the coupler region, we can write $\phi = \langle\phi\rangle + \Delta\phi$, with $\langle\phi\rangle = 90°$, $\langle\Delta\phi\rangle = 0$. Assuming $\Delta\phi \ll kz$, Eq. (C.3) can be written as

$$
\Delta p_y = \alpha k y \sin(kl)[\sin(2kz_m) + \Delta\phi\cos(2kz_m)] = a_1 y + a_2 y \Delta\phi,
\tag{C.4}
$$

where $l = z_f - z_i$, $z_m = \frac{z_f + z_i}{2}$, $a_1 = \alpha k \sin(kl)\sin(2kz_m)$, $a_2 = \alpha k \sin(kl)\cos(2kz_m)$.

The normalized vertical emittance is given by

$$
\varepsilon_{y0} = \sqrt{\langle(y - \overline{y})^2\rangle\langle(p_y - \overline{p_y})^2\rangle - \langle(y - \overline{y})(p_y - \overline{p_y})\rangle^2},
\tag{C.5}
$$

where $\overline{y} = \langle y\rangle$ etc., here we have $\overline{y} = h$ and $\overline{p_y} = 0$, as shown in Figure C.1.

Substituting $p_y \to p_y + \Delta p_y$, $\overline{p_y} \to \langle p_y + \Delta p_y\rangle = a_1 h$ in Eq. (C.5), we have

$$
\varepsilon_y^2 = \langle(y - \overline{y})^2\rangle\langle(p_y + \Delta p_y - a_1 h)^2\rangle - \langle(y - \overline{y})(p_y + \Delta p_y - a_1 h)\rangle^2.
\tag{C.6}
$$

Suppose there is no coupling between transverse and longitudinal phase spaces, then we can take $\langle y\Delta\phi\rangle = 0$:

$$
\begin{aligned}
\langle(p_y + \Delta p_y - a_1 h)^2\rangle &= \langle p_y^2\rangle + a_1^2(\langle y^2\rangle - h^2) + a_2^2\langle y^2\rangle\langle(\Delta\phi)^2\rangle + 2a_1\langle yp_y\rangle, \\
\langle(y - \overline{y})(p_y + \Delta p_y - a_1 h)\rangle &= \langle yp_y\rangle + a_1(\langle y^2\rangle - h^2).
\end{aligned}
\tag{C.7}
$$

The correction to the 2×2 beam matrix in (y, y') trace space is

$$\Delta = \begin{bmatrix} 0 & a_1 \sigma_y^2 \\ a_1 \sigma_y^2 & a_1^2 \sigma_y^2 + [a_2 k (\sigma_y^2 + h^2) \sigma_z]^2 \end{bmatrix},$$

where $\sigma_y^2 = \langle (y - h)^2 \rangle$ is the rms beam size in y and $k^2 \sigma_z^2 = \langle (\Delta \phi)^2 \rangle$.

After some algebra, we find

$$\varepsilon_y = \sqrt{\varepsilon_{y0}^2 + [a_2 k \sigma_z \sigma_y]^2 (\sigma_y^2 + h^2)}, \tag{C.8}$$

where σ_y, σ_z are the rms beam sizes and $\langle \Delta \phi^2 \rangle = k^2 \sigma_z^2$. In most cases, the second term in Eq. (C.8) is much less than the first term. So approximately, the emittance growth is given by

$$\Delta \varepsilon_y = \varepsilon_y - \varepsilon_{y0} \approx \frac{1}{2 \varepsilon_{y0}} [\alpha k^2 \sin(kl) \cos(2k z_m) \sigma_z \sigma_y]^2 (\sigma_y^2 + h^2). \tag{C.9}$$

As a numerical example, we take the following typical values at FNPL:

$$f = 1.3 \text{ GHz} \rightarrow \text{k} = 27 \text{ m}^{-1},$$
$$E_0 = 35 \text{ MV/m} \rightarrow \alpha = 1.27,$$
$$\sigma_z = \sigma_y = 1 \text{ mm}, \ h = 1 \text{ mm} \ [50, 62],$$
$$z_i = 0.11 \text{ m}, z_f = 0.19 \text{ m} \rightarrow z_m = 0.15 \text{ m}, l = 0.08 \text{ m},$$
$$\varepsilon_{y0} = 1 \text{ mm-mrad}.$$

First let's verify that the assumption $\Delta \phi \ll kz$ made in deriving Eq. (C.9) is true:

$$\Delta \phi \sim k \sigma_z = 0.027 \ll kz \sim [2.97, 5.13],$$

So $\Delta \phi$ is less than one percent of kz. From Eq. (C.9), we have $\Delta \varepsilon_y = 3.5 \times 10^{-2}$ mm-mrad, which is 3.5% of the initial value.

A comment on Eq. (C.9): we see that σ_y appears in 2nd and 4th orders on the right-hand side of the equation. So the emittance growth is very sensitive to the

transverse beam size. Now keeping all the parameters the same, but increasing σ_y from 1 mm to 2 mm, from Eq. (C.8), the normalized vertical emittance is 1.35 mm-mrad, which is 35% higher than the initial value.

APPENDIX D
TRANSFER MATRIX OF THE BOOSTER CAVITY

Apart from raising the beam energy by about 12 MeV, the booster cavity also has influences on the transverse motions of the particles, such as focusing and/or deflecting. The effects in transverse plane, to the first order, can be expressed by the linear transfer matrix of the cavity. Therefore it is of interest to measure the transfer matrix of the booster cavity.

The transfer matrix of an rf-section was derived by Chambers in the late 60's [87]. The model considers the motion of an ultra-relativistic beam in a standing wave structure operating in π-mode. Chambers' model has been generalized to the case of an arbitrary (including higher space harmonics) accelerating structure in Ref. [88]. The main results of Ref. [87] is that the trace space transfer matrix of a cylindrical symmetric standing wave rf structure operating at π-mode is given by

$$R = \begin{bmatrix} \cos\alpha - \sqrt{2}\cos\varphi\sin\alpha & \sqrt{8}\frac{\gamma_i}{\gamma'}\cos\varphi\sin\alpha \\ -\frac{\gamma'}{\gamma_f}\left(\frac{\cos\varphi}{\sqrt{2}} + \frac{1}{\sqrt{8}\cos\varphi}\right)\sin\alpha & \frac{\gamma_i}{\gamma_f}\left(\cos\alpha + \sqrt{2}\cos\varphi\sin\alpha\right) \end{bmatrix}, \qquad \text{(D.1)}$$

where γ_i, γ_f are the initial and final Lorentz factors, $\alpha = \frac{1}{\sqrt{8}\cos\varphi}\log\frac{\gamma_f}{\gamma_i}$ and γ' is the normalized accelerating gradient. In virtue of adiabatic damping the determinant of R is $|R| = \gamma_i/\gamma_f$.

Chamber's model is only approximate in our regime where the incoming beam is not ultra-relativistic ($\gamma_i \simeq 8$). Refs [87] and [88] assume the end-region field of the cavity only provides a focusing kick and no acceleration − this is the so-called "hard edge" model. In reality, there is no open boundary condition allowing such a hard edge model: the axial electric field has fringes that extend into the beam pipe on each sides of the structure. Therefore we expect some corrections to the analytical models.

The technique used to measure the transfer matrix is based on a difference orbit method. We use a pair of steerers upstream of the cavity to perturb input trace space parameters to the cavity. The orbit downstream of the cavity is recorded by BPM's. The orbit perturbation $\mathbf{x}_i = (x_i, x_i')^T$ and associated response $\mathbf{x}_f = (x_f, x_f')^T$, are

related accord to

$$\mathbf{x}_f = R\mathbf{x}_i, \tag{D.2}$$

where R stands for the transfer matrix between the points i and f where the initial and final trace space coordinates are measured. Mathematically, one needs a minimum set of four perturbations to compute the four elements of the matrix R. Practically, we impress a set of N perturbations $\delta\mathbf{x}_{i,j}$ to a reference orbit $\mathbf{x}_{i,0}$ ($\delta\mathbf{x}_{i,j} = \mathbf{x}_{i,j} - \mathbf{x}_{i,0}$), where $j = 1, 2, \ldots N$. The corresponding measured response $\delta\mathbf{x}_{f,j} = \mathbf{x}_{f,j} - \mathbf{x}_{f,0}$ can be casted into the system of equation:

$$\mathbf{r} = \begin{bmatrix} \frac{\delta x_{f,1}}{\sigma_{x,1}} \\ \frac{\delta x_{f,2}}{\sigma_{x,2}} \\ \vdots \\ \frac{\delta x_{f,N}}{\sigma_{x,N}} \end{bmatrix} = \begin{bmatrix} \frac{\delta x_{i,1}}{\sigma_{x,1}} & \frac{\delta x'_{i,1}}{\sigma_{x,1}} \\ \frac{\delta x_{i,2}}{\sigma_{x,2}} & \frac{\delta x'_{i,2}}{\sigma_{x,2}} \\ \vdots & \vdots \\ \frac{\delta x_{i,N}}{\sigma_{x,N}} & \frac{\delta x'_{i,N}}{\sigma_{x,N}} \end{bmatrix} \begin{bmatrix} R_{11} \\ R_{12} \end{bmatrix} = \mathcal{P} \begin{bmatrix} R_{11} \\ R_{12} \end{bmatrix}, , \tag{D.3}$$

and

$$\mathbf{r}' = \begin{bmatrix} \frac{\delta x'_{f,1}}{\sigma_{x',1}} \\ \frac{\delta x'_{f,2}}{\sigma_{x',2}} \\ \vdots \\ \frac{\delta x'_{f,N}}{\sigma_{x',N}} \end{bmatrix} = \begin{bmatrix} \frac{\delta x_{i,1}}{\sigma_{x',1}} & \frac{\delta x'_{i,1}}{\sigma_{x',1}} \\ \frac{\delta x_{i,2}}{\sigma_{x',2}} & \frac{\delta x'_{i,2}}{\sigma_{x',2}} \\ \vdots & \vdots \\ \frac{\delta x_{i,N}}{\sigma_{x',N}} & \frac{\delta x'_{i,N}}{\sigma_{x',N}} \end{bmatrix} \begin{bmatrix} R_{21} \\ R_{22} \end{bmatrix} = \mathcal{Q} \begin{bmatrix} R_{21} \\ R_{22} \end{bmatrix}. \tag{D.4}$$

where $\sigma_{x,i}$ and $\sigma_{x',i}$ come from the BPM measurement uncertainty of $\delta x_{f,i}$ and $\delta x'_{f,i}$, respectively.

The two systems of equations above can be inverted using a least square method [89, 90]:

$$\begin{bmatrix} R_{11} \\ R_{12} \end{bmatrix} = [(\widetilde{\mathcal{P}}\mathcal{P})^{-1}\widetilde{\mathcal{P}}]\mathbf{r} \text{ and } \begin{bmatrix} R_{21} \\ R_{22} \end{bmatrix} = [(\widetilde{\mathcal{Q}}\mathcal{Q})^{-1}\widetilde{\mathcal{Q}}]\mathbf{r}'. \tag{D.5}$$

The errors on the computed transfer matrix elements are given by square root of the

diagonal elements of the matrices $(\widetilde{\mathcal{P}}\mathcal{P})^{-1}$ and $(\widetilde{\mathcal{Q}}\mathcal{Q})^{-1}$:

$$\sigma_{R_{1,i}}^2 = [(\widetilde{\mathcal{P}}\mathcal{P})^{-1}]_{ii}, \tag{D.6}$$

$$\sigma_{R_{2,i}}^2 = [(\widetilde{\mathcal{Q}}\mathcal{Q})^{-1}]_{ii}. \tag{D.7}$$

To account for the error coming from the uncertainty on the steerer calibration, a Monte-Carlo simulation was performed [91]. Based on several calibrations of the steerers, we estimate a 15% uncertainty on the steerer calibration. Fifty sets of steerers settings are randomly generated to form a Gaussian distribution with the mean at steerer nominal value and a variance σ_s equal to 15% of the mean. The transfer matrix elements are then computed for each of the 50 settings and the corresponding variance of each element is obtained.

At last, the total error on the computed transfer matrix elements is calculated by adding quadratically the two contribution from BPM measurements and the steerer calibrations.

The orbit perturbations are impressed by means of two pairs of horizontal and vertical steerers located upstream from the TESLA-cavity (S1 and S2 in Figure D.1). The resulting orbit change downstream of the cavity are measured using BPM's. (BPM1, BPM2 in Figure D.1). The beam was first centered on the cavity axis by properly tuning the strengths of the steerer S1 and S2. After centering, a change of $\pm 30°$ in rf-phase and 15% in accelerating gradient induced a maximum position change downstream from the cavity of 500 μm (see Figure D.2).

The beam orbit with the steerers setting used to produce Figure D.2 are used as our reference orbit.

Assume that the steerer is short such that the beam positions are the same at the entrance and exit of the steerer. Given the kick imparted by S1 and S2 (respectively $\delta x'_{S1}$ and $\delta x'_{S2}$), the corresponding position and angle changes at the cavity entrance (referred by index i) with respect to the reference orbit launch are:

$$\begin{aligned}
\delta x_i &= \delta x'_{S1} L_{S1 \to i} + \delta x'_{S2} L_{S2 \to i} \\
\delta x'_i &= \delta x'_{S1} + \delta x'_{S2},
\end{aligned} \tag{D.8}$$
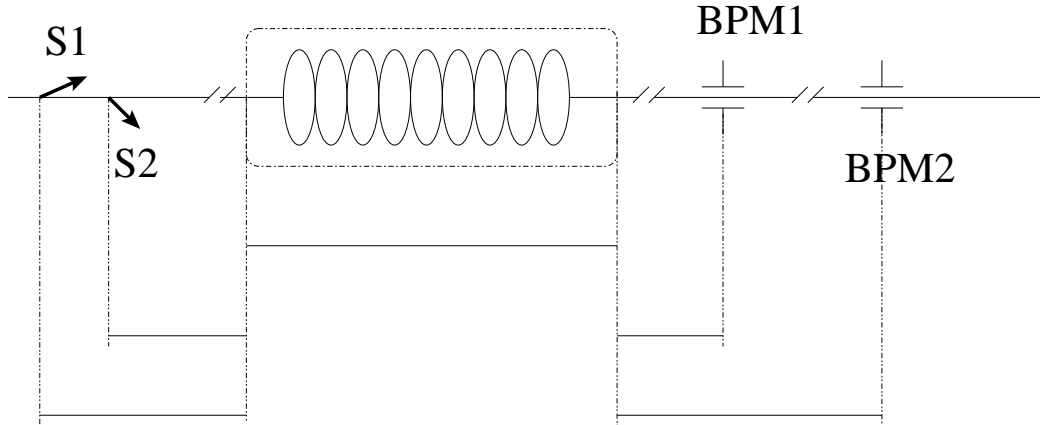
Figure D.1: Experimental set-up relevant to the measurement of the TESLA-cavity transfer matrix. S1 and S2 represent the locations of the two steerers, and BPM1 and BPM2 the locations of the two beam position monitor.

where $L_{a \to b}$ denotes the distance between points a and b. Similarly given the positions changes at BPM1 and BPM2 (respectively δx_{BPM1} and δx_{BPM2}), the corresponding position and angle changes at the cavity exit (referred by index f) are given by:

$$
\begin{aligned}
\delta x_f &= \delta x_{BPM2} - \delta x'_f L_{f \to BPM2} \\
\delta x'_f &= \frac{\delta x_{BPM2} - \delta x_{BPM1}}{L_{BPM1 \to BPM2}}.
\end{aligned}
\tag{D.9}
$$

Eq. (D.8), (D.9) provide all the information needed for solving Eq. (D.5).

The steerer's magnetic field has been measured and some examples are shown in Figure D.3 and Figure D.4. The measured B-field profile versus z can be fitted with the following analytical approximation:

$$
B(z) = B_0 + \frac{\hat{B}}{\cosh(z/a)},
\tag{D.10}
$$

where $\hat{B}$, a and B_0 are the fitting parameters. In Figure D.3 (c), such a fit of the measurement is also presented, and the resulting relevant values are $a = 4.82$ cm and $\hat{B} = 4.28$ G for a 1 A excitation current. The magnetic field offset is found to be $B_0 = 0.53$ G, a value consistent with the earth magnetic field. The advantage in using Eq.(D.10) for modeling the field is that the kick imparted by the steerer can be
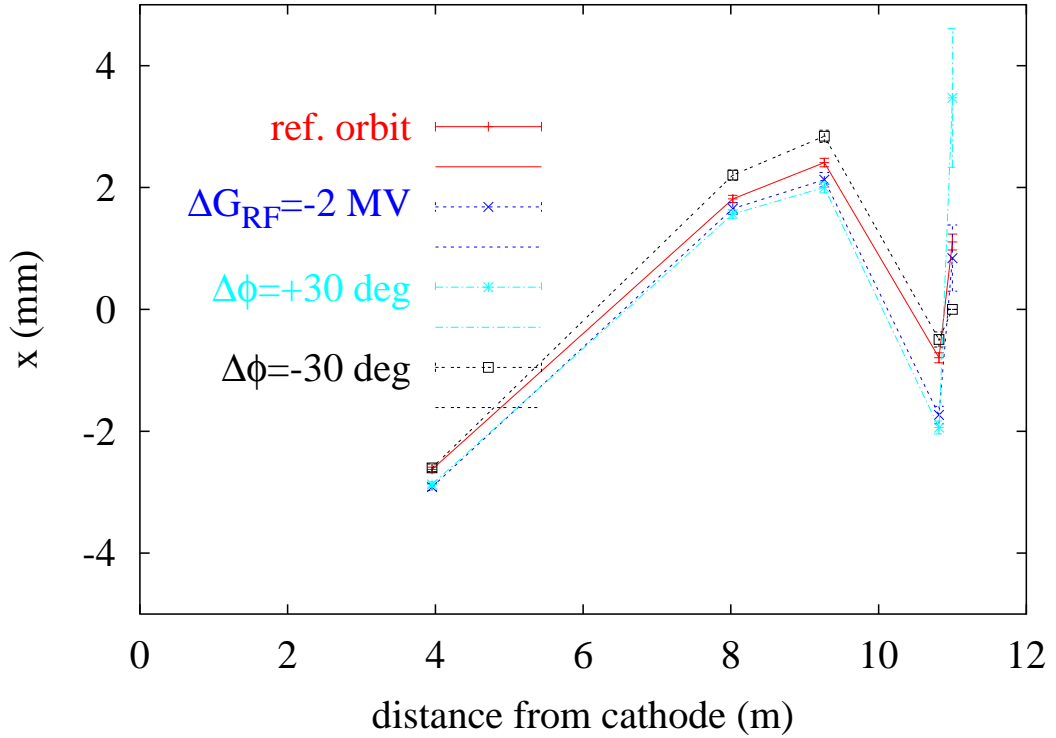
Figure D.2: Orbit variations along the beamline downstream the cavity for different settings of the cavity phase and gradient. The measurements at $z \simeq 11$ m are performed downstream of the dipole spectrometer and thus represent the beam momentum.

then estimated analytically from:

$$\frac{dx'}{dI} = \frac{e \int_{-\infty}^{+\infty} B(z) dz}{p_\parallel} = \frac{e}{p_\parallel} \left[2a\hat{B} \arctan\left(\tanh(z/(2a))\right) \right]_{-\infty}^{+\infty} = \frac{e}{p_\parallel} \pi a \hat{B}, \quad \text{(D.11)}$$

in practical units,

$$\frac{dx'}{dI} [\text{rad/A}] = \frac{1.9436 \times 10^4}{p_\parallel c [\text{eV}]}. \quad \text{(D.12)}$$

Taking into account the length between the steerer (here we consider HTB9C) and the first BPM, one finally gets

$$p_\parallel c [\text{eV}] = \frac{6.1806 \times 10^4}{(dx)/(dI)}, \quad \text{(D.13)}$$

where $(dx)/(dI)$ is in units of m.A^{-1}.
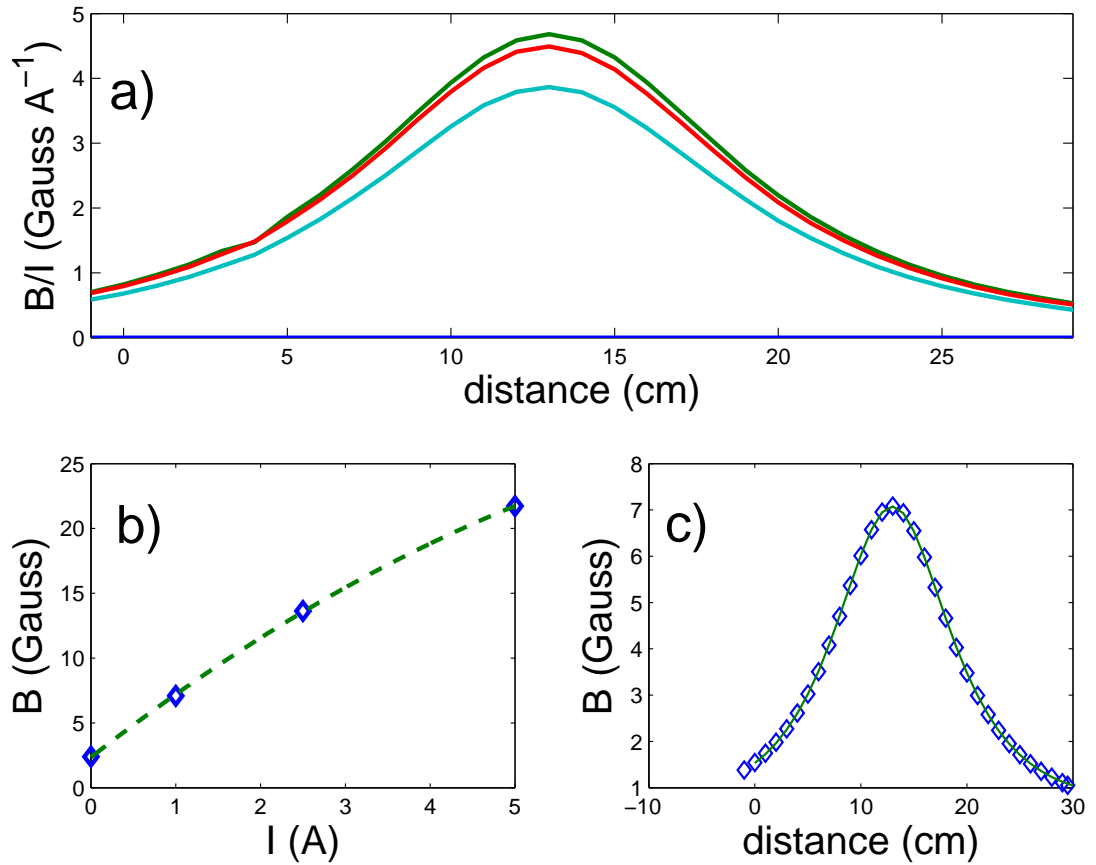
Figure D.3: (a): Measured $B_y(z, x = 0, y = 0)$ field profile for the first steerer at different excitation currents. (b): The field maximum value in (a) versus steerer current. (c): The measured field profile (diamonds) is fitted with Eq. (D.10) (solid line) for an excitation current of 1 A.

Saturation effects on the B versus I curve can be observed when the steerer is operated at the maximum allowed excitation current (5 A) and the onset of the saturation is around 2.5 A, as shown in Figure D.3 (b); these saturation effects are not important for the measurement discussed here since the maximum excitation current is less than 2 A.

The hysteresis curve of the steerers is also measured (see Figure D.4). After various tests, we followed the following procedure to degauss the steerers:

1. cycle the steerer using an oscillating current excitation with exponential decay:
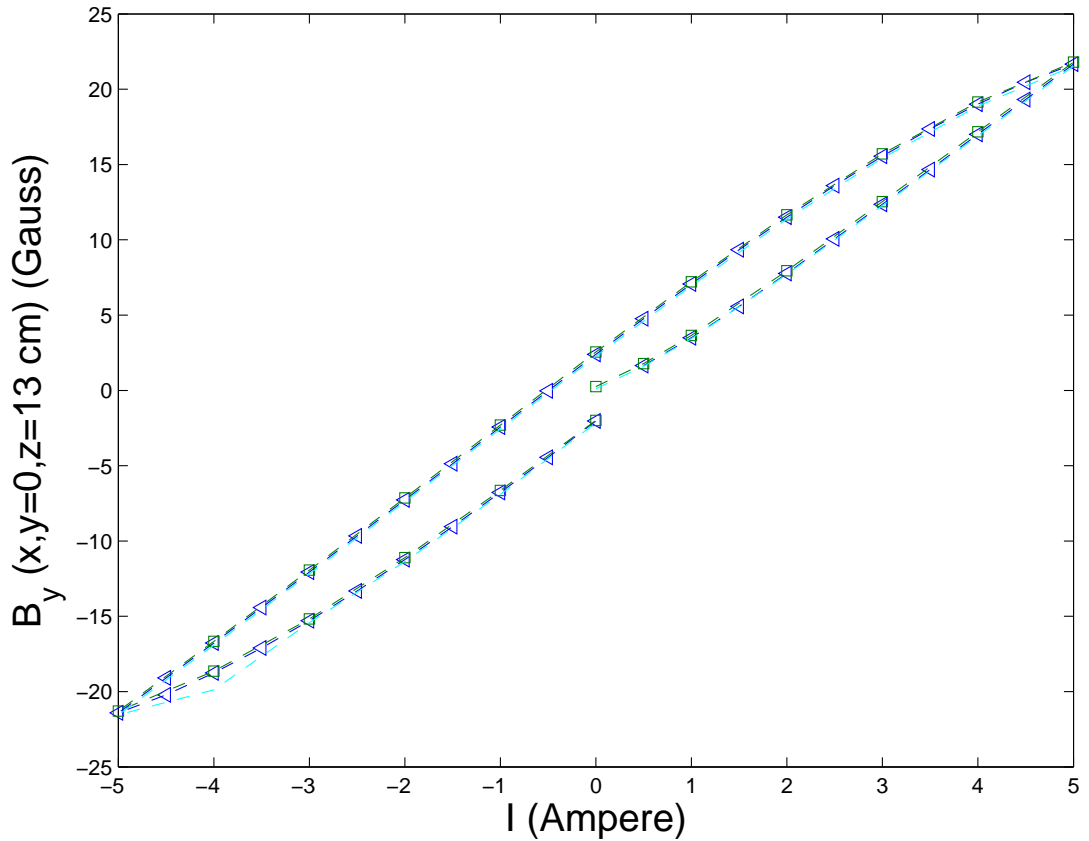
Figure D.4: Measured $B_y(z \simeq 13$ cm$, x = 0, y = 0)$ field hysteresis curve

$$I = I_0 \cos(\omega t) \exp(-t/\tau);$$

2. set the steerer to its maximum positive value;

3. decrease the current to the desired set point.

Steps (2) and (3) of the above procedure indicate that we operate the steerer in the upper part of the hysteresis loop. Thus the linear dependence of the B-field on the current is ensured when operating with excitation current within ± 2 A.

The measurements of transfer matrix elements are presented in Figure D.5. We generally observed a disagreement between experiment and numerical calculations for the first row of the matrix (R_{11} and R_{12}). The second row is in better agreement. The determinant, within the error bars, exhibits the behavior expected from adiabatic damping.
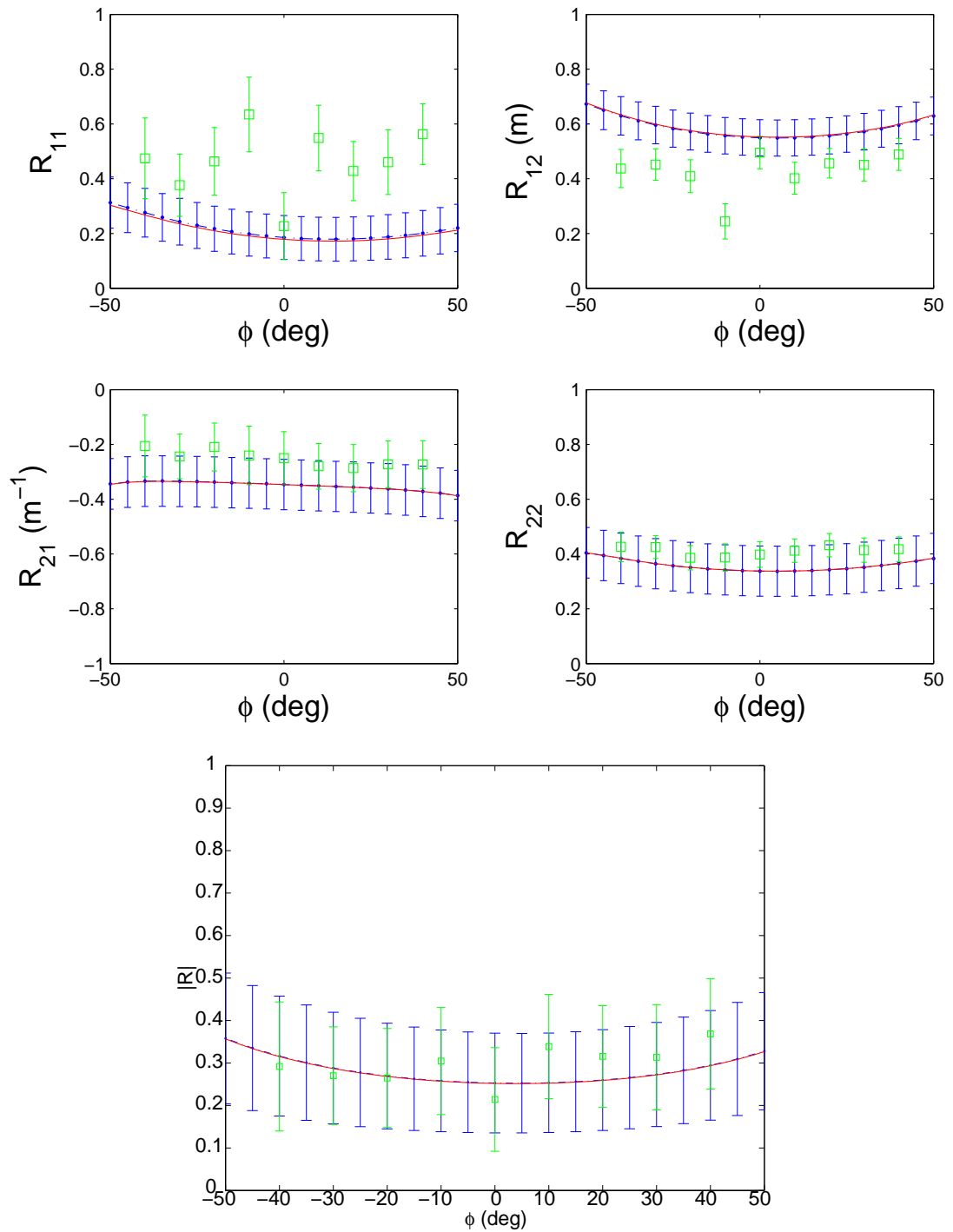
Figure D.5: Experimental measurement (green squares)of the transfer matrix element and inferred determinant comparing with ELEGANT simulation results with ((blue dots) or without BPM calibration error (red line).

REFERENCES

[1] P. M. Lapostolle, IEEE Trans. Nucl. Sci. NS-18 (1971) 1101.

[2] C. Lejeune and J. Aubert, Adv. Electron. Electron Phys., Suppl. **13A**, 159 (1980).

[3] See for example, M. Reiser, *Theory and Design of Charged Particle Beams* (John Wiley & Sons, inc., 1994), pp. 62-66.

[4] K. Floettmann, "Some basic features of the beam emittance," Phys. Rev. ST Accel. Beams **6**, 024202 (2003).

[5] C. A. Brau, "What brightness means," in *The physics and applications of high brightness electron beams* (World Scientific, 2003), pp. 20 - 27.

[6] I. M. Kapchinskij and V.V. Vladimirskij, in *Proceedings of 2nd Int. conf. on High Energy Accel. and Instr.* CERN, 1959, p. 274.

[7] E. Courant and H. Snyder, Ann. Phys. (New York), **3**, pp. 1 - 48 (1958).

[8] L. C. Teng, "Concerning n-dimensional coupled motions," Fermilab Report, FN-229 (1971); "Coupled transverse motion," Fermilab Report, TM-1556 (1989).

[9] K. L. Brown and R. V. Servranckx, "Cross-plane coupling and its effect on projected emittance," SLAC Report, SLAC-PUB-4679 (1989); also published in *Particle Accelerators*, 1991, Vol. 36, pp.121-139.

[10] Ph. Piot, "Review of experimental results on high-brightness photo-emission electron sources," in *The physics and applications of high brightness electron beams* (World Scientific, 2003), pp. 127 -142.

[11] J. S. Fraser, R. L. Sheffield and E. R. Gray, "A new high-brightness electron injector for free electron lasers," NIM 250 (1986) 71-76.

[12] P. G. O'Shea, "RF photoinjectors," in *Proceedings of 1st ICFA workshop on high brightness beam, UCLA.* (World Scientific, 1999).

[13] B. Carlsten, "New photoelectric injector design for the Los Alamos National Laboratory XUV FEL accelerator," NIM A285 (1988) 313-319.

[14] K.-J. Kim, "RF and Space-charge Effects in Laser-driven RF Electron Guns," NIM A275 (1989) 201-218.

[15] L. Serafini, "Analytical description of particle motion in radio-frequency photo-injector," Particle Accelerators, Vo. 49 (1995), pp. 252-271.

[16] L. Serafini and J. Rosenzweig, "Envelope analysis of intense relativistic quasi-laminar beams in rf photoinjectors: A theory of emittance compensation," Phys. Rev. E **55**, 7565 (1997).

[17] M. Reiser, *Theory and Design of Charged Particle Beams* (John Wiley & Sons, inc., 1994). We start from Eq. (5.218); the second term vanishes for a drift space. Adding the canonical angular momentum term, which resembles the emittance term [see Eq. (4.80)], we obtain Eq. (2.1).

[18] E. Noether, "Invariante Varlationsprobleme," Nachr. d. König. Gesellsch. d. Wiss. zu Gttingen, Math-phys. Klasse (1918), 235-257; English translation by M. Travel, *Transport Theory and Statistical Physics* **1**(3), pp. 183-207 (1971).

[19] See for example, M. Reiser, *Theory and Design of Charged Particle Beams*, John Wiley & Sons, INC., 1994, pp. 33-35.

[20] G. I. Budker *et al.*, IEEE trans. Nucl. Sci. **NS-22**, 2093-2097 (1975).

[21] Ya. Derbenev *et al.*, Fizika Plasmy **4**, 492-500 (1978) [Sov. J. Plasma Phys. **4**, 273 (1978)].

[22] V. Parkhomchun, A. Skrinskii, Physics-Uspekhi **43**(5) 433-452 (2000).

[23] I. Ben-Zvi *et al.*, in *Proceedings of the 2003 Particle Accelerator Conference, Portland, Oregon* (IEEE, Piscataway, NJ, 2003), pp. 39-41.

[24] R. Brinkmann, Y. Derbenev and K. Flöttmann, Phys. Rev. ST Accel. Beams **4**, 053501 (2001).

[25] Ya. Derbenev, University of Michigan Report No. UM-HE-98-04 (1998).

[26] A. Burov, V. Danilov, FERMILAB-TM-2043 (1998).

[27] D. Edwards *et al.*, in *Proceedings of the XX International Linac Conference, Monterey, CA*, pp. 122-124 (2000).

[28] D. Edwards *et al.*, in *Proceedings of the 2001 Particle Accelerator Conference, Chicago, IL* (IEEE, Piscataway, NJ, 2001), pp. 73-75.

[29] K. Yokoya and P. Chen, in *Proceedings of the 1989 Particle Accelerator Conference, Chicago, IL* (IEEE, New York, NY, 1989), pp. 1438-1440.

[30] L. Z. Rivkin, in *Proceedings of CAS, Fifth advanced accelerator physics course, Rhodes, Greece* (CERN, Geneva, 1995), pp. 557-572.

[31] J. Corlett *et. al*, in *Proceedings of the 2001 Particle Accelerator Conference, Chicago, IL* (IEEE, Piscataway, NJ, 2001), pp. 2635-2637.

[32] W. Barry *et. al*, Lawrence Berkeley National Lab. Report No. LBNL-51766, 2002.

[33] A. Zholents, P. Heimann, M. Zolotorev, J. Byrd, NIM A425 385-389 (1999).

[34] S. J. Smith and E. M. Purcell, Phys. Rev. **92**, 1069 (1953).

[35] K.-J. Kim and S.-B. Song, NIM A475 158-163 (2001); C. L. Bohn *et. al*, unpublished, available at http://nicadd.niu.edu/presentations/BohnFNPLspeoi.doc.

[36] Y. Zhang, Ya. Derbenev and R. Li, NIM A507 459-463 (2003).

[37] J. Rosenzweig, "Flat-beam rf photocathode sources for linear collider applications," in *Proceedings of 1991 Particle Accelerator Conference, San Francisco, CA*, 1987-1989, (1991).

[38] J. Rosenzweig, "Space charge dominated envelope dynamics of asymmetric emittance rf photocathode injector for linear collider applications," in *Proceedings of 1993 Particle Accelerator Conference, Washington, D.C.*, 3021-3923, (1993).

[39] J. Rosenzweig, "Design of a high duty cycle, asymmetric emittance beams in rf photocathode injector," in *Proceedings of 1997 Particle Accelerator Conference, Vancouver, B.C., Canada*, 1965-1967, (1997).

[40] D. Edwards, unpublished; K.-J. Kim, "Small emittance generation: flat beams," in*Proceedings of ICFA Nanobeam02*, Lausanne, Switzerland (2000).

[41] A. Burov, S. Nagaitsev and Ya. Derbenev, Phys. Rev. E **66**, 016503 (2002).

[42] K.-J. Kim, "Round-to-flat transformation of angular-momentum-dominated beams," Phys. Rev. ST Accel. Beams **6**, 104002 (2003).

[43] H. Wiedemann, "Particle Accelerator Physics I," Second Edition, Springer, 1999, pp. 154-156.

[44] E. Thrane *et al.*, "Photoinjector Production of a Flat Electron Beam," *Proceedings of XXI International Linac Conference, Gyeongju, Korea*,pp. 308-310, (2002).

[45] K.-J. Kim, unpublished; C. L. Bohn, private discussions.

[46] K. Flöttmann, "ASTRA: A Space Charge Tracking Algorithm," available at *http://www.desy.de/∼mpyflo*.

[47] M. Borland, "elegant: A Flexible SDDS-Compliant Code for Accelerator Simulation," Advanced Photon Source LS-287, September 2000.

[48] J. Amundson and P. Spentzouris, "SYNERGIA: A Hybrid, Parallel Beam Dynamics Code with 3D Space Charge," *Proceedings of 2003 Particle Accelerator Conference, Portland, OR*, pp. 3195-3197, (2003).

[49] SYNERGIA simulations presented in the Figure 4.1 are provided by P. Piot.

[50] M. Krassilnikov, *et al.*, in *Proceedings of EPAC 2002*, Paris, France, 1640-1642.

[51] E. R. Colby, "Design, Construction, and Testing of a Radiofrequency Electron Photoinjector for the Next Generation Linear Collider," Ph.D. Dissertation, University of California at Los Angeles, 1997.

[52] J.-P. Carneiro, Ph.D. Dissertation, "Etude Expérimentale du Photo-Injecteur de Fermilab," Université de Paris–Sud, 2001. *http://www-lib.fnal.gov/archive/dissertation/fermilab-dissertation-2001-01.shtml*.

[53] M. J. Fitch, "Electro-Optic Sampling of Transient Electric Fields from Charged Particle Beams," Ph.D. Dissertation, University of Rochester, Rochester, New York, 2000.

[54] R. A. Powell, W. E. Spicer, G. B. Fisher and P. Gregory, "Photoemission studies of Cesium Telluride," Physics Review B, Vol. **8**, Number 8, pp. 3987-3995 (1973).

[55] K. Flöttmann, "Note on the thermal emittance of electrons emitted by cesium telluride photcathodes," TESLA_FEL 97-01, DESY, Germany.

[56] P. Michelato, D. Sertore *et al.*, "Ce_2Te Photocathode for the TTF Injector II," in *Proceedings of EPAC 1996*, Barcelona, Spain, 1510-1512.

[57] M. Kuchnir *et al.*, " Photo-cathode preparation systerm of the A0 photoinjector," Fermilab-TM-2182, 2002.

[58] A. Fry, E. Hahn, W. Hartung *et al.*, "Experience at Fermilab with high quantum efficiency photo-cathodes for RF electron guns," in *Proceedings of the XIX International Linac Conference, Chicago, IL*, pp. 642-644 (1998).

[59] W. Hartung *et al.*, "Studies of photo-emission and field emission in an RF photo-injector with a high quantum efficiency photo-cathode," in *Proceedings of the 2001 Particle Accelerator Conference, Chicago, IL* (IEEE, Piscataway, NJ, 2001), pp. 2239-2241.

[60] A. R. Fry, "Novel pulse train glass laser for rf photoinjectors," Ph.D. Dissertation, University of Rochester, Rochester, New York, 1996.

[61] T. Berenc, Sept. 2003. "Calibration of the rf power monitors for the photoinjector laboratory rf system," FermiLab Beams Document 575-v1, is available at *http://beamdocs.fnal.gov/cgi-bin/public/DocDB/ShowDocument?docid=575&version=1.*

[62] R. Cee, *et al.*, "Beam Based Alignment of the TTF RF-Gun Using V-code," TTF/FEL collaboration meeting, Frascati, Italy, Nov. 5-7, 2001.

[63] W. Beinhauer *et al.*, "Beam-Based Alignment of TTF RF-Gun Using V-code," in *Proceedings of the 2001 Particle Accelerator Conference, Chicago, IL* (IEEE, Piscataway, NJ, 2001), pp. 3099 - 3101.

[64] B. Aune *et al.*, "Superconducting TESLA cavities," Phys. Rev. ST Accel. Beams **3**, 092001 (2000).

[65] Model number C-mount C25011 see documentation at *http://www.pentaxusa.com/pdf/Manual_Iris_Lenses_Pages.pdf.*

[66] J. Wennerberg, unpublished results and private communication, July 2004.

[67] See "USAF 1951 and microscopy resolution test charts" available at *http://www.efg2.com/Lab/ImageProcessing/TestTargets.*

[68] Information from PENTAX USA web-site.

[69] M. Hüning, Fermilab Beams Document, Beams-doc-652-v1 available at *http://beamdocs.fnal.gov/cgi-bin/public/DocDB/ShowDocument?docid=652&version=1.*

[70] K. Desler, *et al.*, Fermilab Beams Document, Beams-doc-1361-v1 (2004).

[71] HAMAMATSU Universal Streak Camera C5680 series Instruction manual.

[72] K. Honkavaara, Ph. Piot, S. Schreiber and D. Sertore, "Bunch length measurements at TTF with a streak camera," DESY, TESLA 2000-38.

[73] K. Bishofberger, "FNPL Spectrometer Recalibration" (2002), unpublished, available at *http://nicadd.niu.edu/fnpl/docs/kip-spectrometer.pdf.*

[74] P. Piot, N. Barov, R. Berenc and Y.-E. Sun, "Notes on Energy Measurements at FNPL," Fermilab Beams Document, Beams-doc-1132-v1 (2004).

[75] For dispersion functions of various types of dipoles, see for example, H. Wiedemann, "Particle Accelerator Physics I," Second Edition, Springer, 1999, p. 170.

[76] Model ICT-122-070-20:1, Bergoz Instrumentation, France. *http://www.bergoz.com.*

[77] J.-P. Carneiro *et al.*, "A0 Photo-Injector: Experiments with Gun A: June 97 to December 97," Fermilab-EXP-202, 1999.

[78] Y.-E. Sun *et al.*, "Generation of angular-momentum-dominated electron beams from a photoinjector," Phys. Rev. ST Accel. Beams **7**, 123501 (2004).

[79] P. Piot and Y.-E. Sun, "Optical set-up for digital cemera system at FNPL," FermiLab Beams Document 1346-v1, available at *http://beamdocs.fnal.gov/cgi-bin/public/DocDB/ShowDocument?docid=1346&version=1.*

[80] J. H. Billen and L. M. Young, in *Proceedings of the 1993 Particle Accelerator Conference, Washington DC* (IEEE, Piscataway, NJ, 1993), pp. 790-792.

[81] Review of Particle Physics, Euro. Phys. Jour. **C 3**, num 1-4 (1998) p. 146.

[82] L. Emery, *User's Guide to shower version 1.0, an EGS4 Interface* available http:www.aps.anl.gov/asd/oag/manuals/shower_V1.0/shower.pdf.

[83] "TESLA techical design report - part II, the accelerator," TESLA report 2001-23, edited by R. Brinkmann *et al.*

[84] T. Maruyama *et. al*, Phys. Rev. Lett. **66**, 2376 (1991); Phys. Rev. B **46**, 4261 (1992).

[85] T. Nakanishi *et. al*, Phys. Lett. A **158**, 345 (1991); T. Omori *et. al*, Phys. Rev. Lett. **67**, 3294 (1991).

[86] S. Lidia *et. al*, in *Proceedings of the 2003 Particle Accelerator Conference, Portland, Oregon* (IEEE, Piscataway, NJ, 2003), pp. 2086-2088.

[87] E. Chambers, Stanford High Energy Physics report (1965) (unpublished).

[88] J. Rosenzweig and L. Serafini, Phys. Rev. E **47**, 2031 (1994).

[89] W. Press, S. Teukolsky, W. Vetterling and B. Flannery, *Numerical Recipes in C*, 2nd edition (Cambridge University Press, 1992), pp. 671-673.

[90] P. Bevington and D. Robinson, *Data Reduction and Error Analysis for the Physical Science*, 2nd edition (WCB McGraw_Hill, 1992), pp. 101 - 109.

[91] P. Piot and Y.-E. Sun, "Note on the transfer matrix measurement of a TESLA cavity (preliminary results)," FermiLab Beams Document 1521-v1, available at *http://beamdocs.fnal.gov/cgi-bin/public/DocDB/ShowDocument?docid=1521&version=1.*